Università degli Studi della Basilicata

Dottorato di Ricerca in

"Ingegneria per l'Innovazione e lo Sviluppo Sostenibile"

INNOVATIVE INDICES FOR WATER STRESS DETECTION FROM HYPERSPECTRAL INFRARED OBERVATIONS

Settore Scientifico-Disciplinare

FIS/06

Coordinatore del Dottorato

Prof.ssa Aurelia Sole

Dottoranda

Pamela Pasquariello

Relatori

Prof. Guido Masiello

Prof. Carmine Serio

Ciclo XXXVI

Contents

List of Figures

List of Tables

"But Nature flies from the Infinite;
for the Infinite is imperfect, and
Nature always seeks an end."
(Aristotle)

Abstract

Monitoring surface and vegetation conditions is crucial for analyzing the impact of climate change on natural resources. Detecting vegetation stress using remote-sensing data is essential for understanding these changes and taking action against extreme events like land and forest dryness caused by summer heatwaves in the Mediterranean region. Commonly used satellite indices for this purpose include the Normalized Difference Vegetation Index (NDVI), followed by the Leaf Area Index (LAI), Fraction of Absorbed Photosynthetically Active Radiation (FAPAR), Surface Soil Moisture (SSM), and physical parameters such as near-surface air temperature (T_a), obtained from both remote sensing data and on-site measurements.

However, it is a well-known fact that NDVI cannot distinguish between barren soil and distressed vegetation and, while surface temperature and air temperature have an influence on soil moisture, correlation among these three quantities is not straightforward to evaluate.

This thesis aims at demonstrating the effectiveness of two newly-developed thermodynamical indices, the Emissivity Conrast Index (ECI) and the Water Deficit Index (WDI), in assessing vegetation stress and woodland degradation, specifically in southern Italy from 2014 to 2022. ECI is based on infrared surface emissivity, closely related to land cover, while WDI directly measures surface water loss. These indices have been calculated using physical parameters derived from observations acquired by the Infrared Atmospheric Sounding Interferometer (IASI), then upscaled and remapped on a regular grid using an Optimal Interpolation (OI) scheme. A comparison with other traditional indices is presented, further validating the applied methodology.

Additionally, it is shown how the synergy between ECI and WDI can be exploited to identify the criminal origin of a fire event, specifically the Mount Vesuvius arsons of summer 2017, uncoupling the fire outbreak from the heatwave that affected the Mediterranean area during that same period.

Finally, the Weather Reasearch and Forecasting (WRF) model is used with two different sets of global forecasts as input -Global Forecast System (GFS) and European Centre for Medium-Range Weather Forecasts (ECMWF)-

to calculate WDI, surface and dew-point temperature (T_s and T_d) maps for July 2017 over southern Italy. The results are compared against the WDI maps obtained from IASI retrievals, showing a high level of similarity, as well as limited yet interesting differences, mainly related to the specific implementations of the global Numerical Weather Prediction (NWP) models from which the input forecasts were derived.

Chapter 1

Earth surface and atmosphere monitoring for drought and surface dryness

1.1 The problem

Climate change is undeniably affecting the environment, supported by substantial evidence (Trenberth et al. 2014; Cook, Mankin, and Anchukaitis 2018; Samaniego et al. 2018; Adler et al. 2022). One of the most prominent indicators is the global rise in average temperatures, which has altered Earth's hydrological cycle (Christensen et al. 2021). This worldwide pattern has led to the expansion of the tropical belt and a drier environment, characterized by more frequent and severe water-related events like extreme droughts, heatwaves, and temperature extremes (Samaniego et al. 2018; A. P. Williams et al. 2020; Edenhofer 2015). In many countries, the widespread issue of vegetation and soil water stress has intensified due to the effects of climate change. Drought, once considered a natural disaster, is now increasingly prevalent not only in semi-arid regions but also in the Mediterranean area. This shift has led to heightened concern, particularly in areas abundant with vegetation and forests. Prolonged drought periods in such regions elevate the risk of forest fires whereas, in semi-arid zones, drought exacerbates water stress.

Drought, a complex situation resulting from low precipitation and limited water availability in soils, significantly impacts natural vegetation and accelerates desertification. Water stress caused by drought reduces growth and increases mortality in forest ecosystems, transforming the landscape (A. P. Williams et al. 2020; D'Orangeville et al. 2018; Cholet et al. 2022). For-

est water stress occurs when trees face prolonged or severe water shortages that surpass their coping mechanisms, leading to physiological and ecological responses that ultimately affect forest health and productivity. These responses can be categorized into physiological and ecological symptoms (Lisar, Motafakkerazad, and Hossain 2012; Imadi et al. 2016).

Physiological symptoms of forest water stress encompass changes in plant water status, gas exchange, growth, and metabolism. Water deficit disrupts essential plant activities, restricting their responses to environmental changes. Researchers like Lisar, Motafakkerazad, and Hossain 2012 have outlined the effects of water stress on plants, including alterations in photosynthesis, respiration, translocation, ion uptake, carbohydrates, nutrient metabolism, and hormones. Insufficient water availability initially reduces water potential in plant cells, leading to growth inhibition, reproductive failure, and wilting due to the accumulation of substances like abscisic acid and osmolytes (Lisar, Motafakkerazad, and Hossain 2012; Imadi et al. 2016; Hsiao 1973; Kramer 1963). Prolonged water stress can lead to forest mortality, ranging from individual trees to large forest stands collapsing.

Water deficit-induced vegetation stress is a prevalent issue in numerous countries due to climate change, as evidenced in studies (Rita et al. 2020; Anderegg et al. 2020). Drought, an extreme natural phenomenon common in semi-arid areas and many Mediterranean regions, particularly those at moderate latitudes, poses a significant threat. Prolonged periods without rain heighten the risk of forest fires in lushly vegetated and wooded lands (Mishra and Singh 2010). Moreover, the absence of rainfall in semi-arid zones leads to water stress, as indicated in Feiziasl et al. 2022; Spinoni et al. 2019. Consequently, addressing the scarcity of rainfall and overall water supply necessitates specific measures to monitor and identify drought conditions. These efforts are essential to mitigate the adverse impacts of drought on human health, wildlife, and plant communities.

1.2 State of the art

To minimize the negative effects on human well-being, wildlife, and plant ecosystems, it is crucial to implement measures that focus on monitoring and promptly identifying water stress in vegetation and soil. This can be accomplished by employing three specific approaches: field measurements, meteorological data (e.g., Sutanto et al. 2019; J. S. Stoyanova and Georgiev 2013; Gouveia, Trigo, and DaCamara 2009), and remote sensing (e.g., Bento et al. 2018; J. Stoyanova et al. 2019; Feldman et al. 2020; Vicente-Serrano, Pons-Fernández, and J. Cuadrat-Prats 2004).

Remote sensing methods are increasingly being employed to assess forest water stress due to their advantages, particularly in terms of spatial coverage compared to traditional ground-based approaches (Harris, Bryant, and Baird 2006; Joshi et al. 2021; N. Liu et al. 2020). These techniques, which include satellite imagery, offer insights into water stress over vast areas, including remote or inaccessible regions. This capability is invaluable for monitoring forests on a regional or even global scale, given the crucial role of forests in the global water cycle, energy, and carbon balances. Remote sensing methods are non-intrusive and can gauge water stress without direct contact with the forest (Govender et al. 2009).

Remote sensing in vegetation observation operates on the principle of using sensors to measure various wavelengths of electromagnetic radiation emitted or reflected by plants and their surrounding environment (Huete 2004; J. Wang et al. 2010). Healthy vegetation exhibits distinct patterns of reflection and absorption of different wavelengths, which can be detected by remote sensing instruments (Huete 2004; Gausman 1977). For instance, healthy vegetation predominantly absorbs visible light but reflects a significant amount of near-infrared (NIR) radiation. Consequently, in visible composite images, healthy vegetation appears green, while in near-infrared images, it appears bright (see Fig. 1.1). Through the analysis of these reflected or emitted electromagnetic radiation patterns, remote sensing instruments can provide valuable data about vegetation properties such as leaf area index (LAI), chlorophyll content, water content, and biomass (Ceccato et al. 2001; N. C. Coops et al. 2003; Curran, Dungan, and Gholz 1990). This information is instrumental in monitoring vegetation health, identifying areas of vegetation stress.

The typical spectral reflectance of vegetation demonstrates high reflectance in the NIR region (around 700–1300 nm) and lower reflectance in the visible region (around 400–700 nm) (Stone, Chisholm, and Coops 2001; Blackburn 1999; Rouse et al. 1974a). This phenomenon is attributed to chlorophyll absorption in the visible wavelengths and the strong reflectance caused by the internal structures and water content of plant cells in the NIR region (Lichtenthaler 1987). Additionally, vegetation tends to exhibit low reflectance in the shortwave infrared (SWIR) region (around 1300–2500 nm) due to water and cellulose absorption in plant tissues (Harris, Bryant, and Baird 2006; Faurtyot and Frédéric Baret 1997; Asner 1998). The spectral characteristics of plants respond to different wavelength radiations (N. C. Coops et al. 2003; Asner 1998; Nicholas Coops et al. 2002). Pigments, especially chlorophyll, predominantly govern the spectral responses of leaves in visible wavelengths, closely linked to photosynthetic capacity and overall primary productivity (Gausman 1977; Curran, Dungan, Macler, et al. 1991). Additionally, the

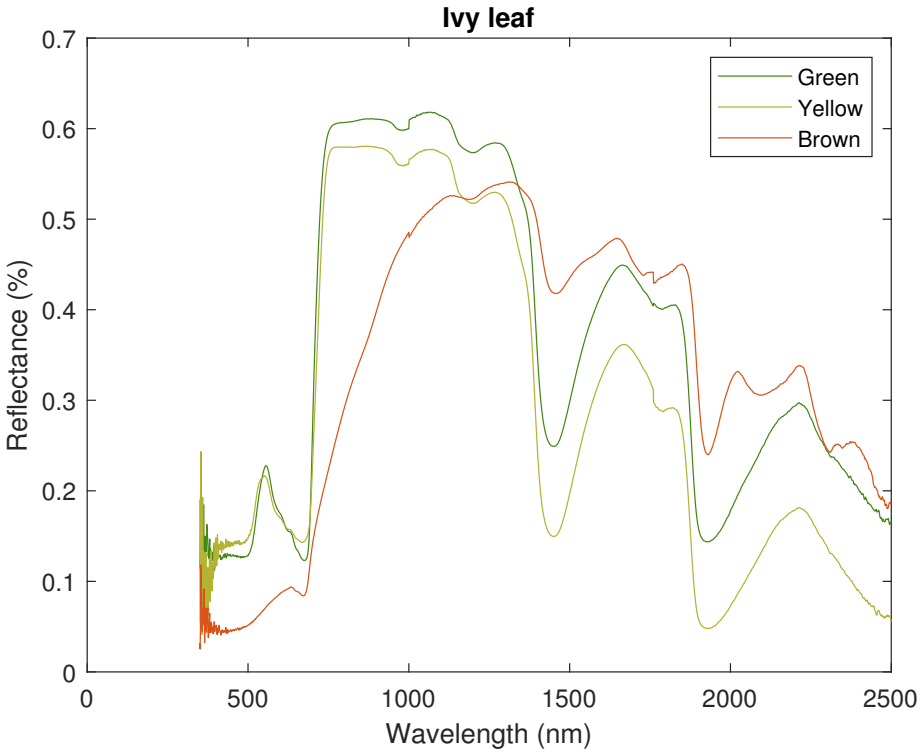

(a)

(b)

Figure 1.1: Reflectance spectra (1.1a) of three leaves from the same ivy (1.1b) at different colors (and health states): green, yellow, and brown.

leaf's cell structure impacts spectral reflectance characteristics at NIR wavelengths, while leaf water content influences interactions with wavelengths in the SWIR region.

Water stress occurs when plants suffer from water shortage, leading to changes in their physiological and biochemical processes, ultimately reducing vegetation health (Lisar, Motafakkerazad, and Hossain 2012). These alterations can be detected through remote sensing techniques to monitor plant health and identify water stress areas (J. Wang et al. 2010; L. O. Anderson et al. 2010; Eitel et al. 2006; Fuchs 1990). One method for detecting water stress involves measuring changes in the reflectance of visible and near-infrared light (L. O. Anderson et al. 2010; Eitel et al. 2006). Generally, stressed plants exhibit lower reflectance in the near-infrared region and higher reflectance in the visible region (Gausman 1977). Another approach to detecting water stress is by assessing changes in the thermal properties of plants using thermal infrared sensors (N. Liu et al. 2020; Sepulcre-Cantó et al. 2006). As plants experience water stress, they may have higher leaf temperatures due to reduced transpiration for cooling and heat accumulation.

1.2.1 Vegetation Indices (VIs)

Several vegetation indices (VIs) have been created to track alterations in vegetation and associated physiological processes. These indices utilize the spectral reflectance features of plants obtained through diverse imaging methods, combining reflectance at specific spectral wavelengths. Many of these indices have been extensively employed to identify water stress in vegetation, particularly in forests (as documented in Vicente-Serrano, José M Cuadrat-Prats, and Romo 2006; S. Chen et al. 2015; Guido Masiello, Cersosimo, et al. 2020). Le, Harper, and Dell 2023 classifies them according to the specific spectral bands used for their calculation:

- typical VIs, based on the reflectance in the visible red range (600–700 nm) and a portion of the NIR range (700–900 nm);
- water VIs, using SWIR-band reflectance;
- pigment VIS, individuating the concentrations of leaf pigments, mainly chlorophyll, by using green and red-edge reflectance;
- temperature VIs, with thermal infrared signals which provide information concerning land surface and canopy temperature.

The most used index from the first category is the Normalized Difference Vegetation Index (NDVI) (Rouse et al. 1974b), which is defined as follows:

$$NDVI = \frac{\rho_{NIR} - \rho_{RED}}{\rho_{NIR} + \rho_{RED}} \tag{1.1}$$

where ρ_{NIR} and ρ_{RED} are the reflectances in the near-infrared and red bands, respectively.

The mid-infrared (MIR) region, spanning approximately 1300 to 2500 nm, displays a notable absorption feature related to water, which intensifies with higher water content (Musick and Pelletier 1988; Hunt Jr and Rock 1989). Various water-vegetation indices have been developed by analyzing reflectance data from the NIR, MIR, and shortwave infrared (SWIR) regions of the electromagnetic spectrum. Among these indices, the Normalized Difference Water Index (NDWI), devised by Gao 1996, is widely used for assessing water content and detecting plant water stress. This index is calculated using sensitive NIR and SWIR wavelengths that capture the presence of water within plant tissues. It is defined as:

$$NDWI = \frac{\rho_{NIR} - \rho_{SWIR}}{\rho_{NIR} + \rho_{SWIR}} \tag{1.2}$$

NDWI has been widely used to estimate water content for various tree species (Jackson et al. 2004), particularly in areas where water availability is limited or where drought stress is prevalent (Eitel et al. 2006).

Similarly to NDWI, Surface Soil Moisture (SSM) refers to the amount of water content present in the top layer of the soil, typically in the upper few centimeters or decimeters, depending on the context. This moisture content is a crucial parameter in understanding the immediate availability of water for plants, ecosystems, and various land surface processes (Daly and Porporato 2005). SSM can be influenced by factors such as precipitation, evaporation, transpiration, runoff, and soil characteristics. Monitoring and analyzing surface soil moisture are important for agricultural practices, hydrology, weather forecasting, climate studies, and land management, as it directly impacts vegetation health, water resource management, and overall ecosystem dynamics.

The spectral properties of canopy temperature refer to how plants emit thermal radiation across different parts of the electromagnetic spectrum, depending on their temperature (Fuchs 1990). Several factors, such as solar radiation, air temperature, humidity, and plant water use, affect the temperature of a plant canopy. In the thermal infrared (TIR) region of the spectrum, plants emit radiation within wavelengths ranging from 800 to 1400 nm, allowing for the estimation of their temperature (Joshi et al. 2021; Amani et al. 2017; Zhang et al. 2019). Various spectral indices have been developed using

TIR data to estimate canopy temperature and identify plant stress, such as the Temperature Vegetation Dryness Index (TVDI, Sandholt, Rasmussen, and Andersen 2002) and the enhanced TVDI (iTVDI, Rahimzadeh-Bajgiran, Omasa, and Shimizu 2012. TVDI is a spectral index used to assess vegetation water stress based on canopy temperature and vegetation cover. It is calculated by taking the difference between surface temperature T_s (measured by thermal sensors) and the ambient environment's temperature close to the surface T_a, and dividing it by the difference between surface temperature and a reference temperature representing maximum transpiration under the same atmospheric conditions (Sandholt, Rasmussen, and Andersen 2002). A higher TVDI value indicates more severe water stress, while a lower value indicates sufficient water supply.

In addition to these spectral indices, it is crucial to mention other key parameters, mainly related to canopy structure: the Leaf Area Index (LAI), the Fraction of Absorbed Photosinthetically Active Radiation (FAPAR) and the Fractional Vegetation Cover (FVC). These indices can be estimated both in situ and from satellite observations.

LAI represents the total leaf area per unit ground area (usually measured as m^2/m^2) and is a critical parameter for understanding the structure and health of vegetation (Myneni et al. 1997). It quantifies the collective leaf surface area per unit ground area, establishing a direct correlation with the available light interception capacity of plants and the extent of green vegetation interacting with solar radiation, influencing the remote sensing signal. Additionally, it represents the size of the interface between the vegetation canopy and the atmosphere, impacting energy and mass exchanges. This metric holds significance as it serves as a pivotal parameter for forecasting photosynthetic primary production, estimating evapotranspiration, and functioning as a reference tool in crop growth studies. Consequently, LAI assumes a crucial role in the realm of theoretical production ecology. LAI serves as a crucial input for Numerical Weather Prediction (NWP), regional and global climate modeling, weather forecasting, and global change monitoring. Moreover, LAI holds relevance for various land-monitoring applications, including agriculture and forestry, environmental management, land use planning, hydrology, monitoring and management of natural hazards, and tracking vegetation-soil dynamics and drought conditions.

FAPAR measures the fraction of incoming solar radiation absorbed by vegetation for photosynthesis. It provides insights into the vegetation's efficiency in utilizing sunlight for biological processes and is derived from remote sensing data (Widlowski et al. 2004). Specifically, it defines the proportion of Photosynthetically Active Radiation (PAR) within the range of $400-700\,\mathrm{nm}$ that is absorbed by the green components of the canopy, reflect-

ing the canopy's capability to absorb energy. FAPAR is realted to canopy structure, optical properties of leaves and soil, and prevailing irradiance conditions. Acknowledged as a fundamental terrestrial state variable in the realm of global change sciences, FAPAR plays a pivotal role in models assessing vegetation primary productivity. It is particularly crucial in carbon cycle models that integrate state-of-the-art land surface process schemes. Additionally, FAPAR serves as an indicative measure of vegetation health and is generally well correlated with LAI, especially for robust and healthy vegetation canopies.

FVC quantifies the proportion of the ground covered by vegetation, considering both vertical and horizontal distribution. It is defined as the complement to unity of the gap fraction at nadir direction, accounting for the amount of vegetation distributed in a horizontal perspective. FVC plays a key role in determining the contribution of soil and vegetation to emissivity and temperature, essential for comprehensive descriptions of land surface processes and parameterization schemes employed in climate and weather forecasting(Chu and Chu 2020). Moreover FVC is employed in a wide range of applications, encompassing agriculture, forestry, environmental management, land use planning, hydrology, monitoring and managing natural hazards, assessing vegetation-soil dynamics, and evaluating conditions related to drought and the extent of fire scars.

Lastly, it is worth mentioning evapotranspiration (ET) as another key parameter in monitoring water stress in vegetation. ET is the combined process of water vapor transfer into the atmosphere through two main mechanisms: evaporation from the Earth's surface and transpiration from plants. This process is a key component of the Earth's water cycle and plays a crucial role in the distribution and movement of water in ecosystems. Evaporation refers to the process by which liquid water at the surface is transformed into water vapor and released into the atmosphere. It occurs from open water bodies, moist soil, and wet vegetation surfaces. Transpiration is the release of water vapor from plant leaves into the atmosphere. Plants absorb water through their roots, and this water is transported upward through the plant to the leaves, where it is released as vapor through tiny pores called stomata. Several factors influence the rate of ET, including solar radiation, temperature, wind speed, humidity, and the availability of water in the soil. These factors collectively determine the energy available for the conversion of liquid water into vapor. ET can be measured using various techniques, including field-based methods such as lysimeters, eddy covariance systems, and Bowen ratio systems. Remote sensing technologies, such as satellites and aerial imagery, are also employed to estimate ET over large spatial scales. ET is a crucial component of the hydrological cycle. The water vapor released into

the atmosphere eventually condenses to form clouds and, under the right conditions, precipitates as rain or snow, completing the cycle. It also plays a significant role in land surface-atmosphere interactions and influences local climate, humidity levels, and temperature, representing a key variable in climate models. It is also true that changes in land use, climate, and water availability can impact ET patterns, influencing ecosystems, water resources, and overall environmental health.

1.3 Limitations of current methodologies

While this index can provide valuable information about the state of vegetation, it has inherent limitations when distinguishing between senescent vegetation and arid soil, especially when vegetation cover is sparse or the soil surface is exposed (as discussed in Karnieli et al. 2010). In certain situations, senescent vegetation and arid soil may exhibit overlapping NDVI values, making it challenging to differentiate between the two based solely on NDVI (Galvão, Vitorello, and Pizarro 2000).

Furthermore, neither T_s and T_a are able to provide direct insights into soil moisture content, which is a vital factor in assessing water stress. Evaluating the correlation among these three variables is not straightforward (Berg et al. 2014; Jiang et al. 2022).

Similarly to NDVI, TVDI can be affected by non-vegetated surfaces, such as bare soil or urban areas. The index may not effectively discriminate between stressed vegetation and other land cover types, leading to potential misinterpretations. Moreover, TVDI assumes homogeneous atmospheric conditions across the study area: variations in atmospheric properties can influence the thermal infrared signal, affecting the reliability of TVDI in regions with diverse climates (Du et al. 2017; Guo et al. 2023).

The main challenge in the use of FAPAR, FVC and LAI is realted to the performance of the different algorithms used to derive them, which can vary based on the characteristics of the study area and the accuracy of the algorithm itself. Sensitivity to specific land cover types and environmental conditions may affect the estimation of said indices and, together with an extensive use of modeling techniques, heavily leaning on parameterization, could also produce a notable level of uncertainty in the representation of actual surface conditions (Frederic Baret and Buis 2008).

It is worth emphasizing that researchers have extensively explored the relationships between surface temperature and NDVI for evaluating drought conditions. However, it is crucial to note that in specific scenarios, as highlighted in prior studies (as noted in Ru et al. 2020), these relationships have

produced inconsistent results.

This underscores the complexity of understanding vegetation water stress and the necessity for comprehensive and nuanced approaches that consider multiple factors to accurately assess the health and moisture levels of vegetation, especially in forest ecosystems. Such complexities necessitate a holistic evaluation that combines various data sources and indices, going beyond the limitations of individual parameters, to gain a comprehensive understanding of the intricate interplay between vegetation, surface temperatures, and soil moisture content.

The next chapters of this thesis are devoted at exposing and validating a new methodology proposal for drought and surface water stress. It relies on the use of surface temperature and emissivity, as well as dew point temperature (T_d) close to the surface. These three physical quantities are more closely related to surface type, coverage and soil moisture, proving to be extremely useful in detecting changes in surface water content and vegetation health, as it will be extensively shown.

Chapter 2

New thermodynamical indices and their retrieval scheme

This chapter is devoted to exposing the proposed methodology, presenting the developed indices, the process of calculating them, and the data used. Specifically, it will be focused on the methodology developed to compute ECI and WDI maps from IASI observations.

2.1 Proposed methodology

To address the limitations highlighted in Section 1.3, a comprehensive and unified methodology is implemented, ensuring both spatial and temporal consistency in our analyses. This approach involves the concurrent observation and computation of surface characteristics and thermodynamic air parameters to define two new indices, ECI and WDI, whose formulation caters specifically to regional-scale analysis. Proficient use of satellite data is then necessary to ensure precise spatial coverage and consistent temporal sampling. For this purpose, the IASI hyper-spectral satellite (Hilton et al. 2012), operating on the European Meteorological Platforms (MetOp) deployed by the European Organisation for the Exploitation of Meteorological Satellites (EUMETSAT), proves to be invaluable. Through effective utilization of IASI observations, we can extract surface temperature and dew point temperature simultaneously, overcoming challenges associated with coordinating data across time and space. However, it is vital to note that satellite data are accessible at irregular grid points, introducing complexities in the analysis of spatial patterns. Overcoming these challenges, our methodology aims to enhance our understanding of water stress dynamics, providing valuable insights into regional water management strategies.

Leveraging the air parameters from IASI, we can compute the dew point temperature, a direct indicator of surface evapotranspiration processes. Moreover, the emissivity data acquired from IASI are employed to calculate the emissivity contrasts in various thermal bands. Thus, the reason why ECI and WDI are referred to as *thermodynamical* indices is evident: they account for the condition of both land and atmosphere and are directly estimated using thermodynamical quantities. This provides them with a more direct phyisical meaning and interpretation in the context of Earth surface and atmosphere monitoring.

In this framework, the goals of this thesis encompass two main aspects: first, defining and computing the indices derived from direct satellite soundings; second, formulating a method to interpolate the sparse satellite retrievals onto a consistent grid. This interpolation technique is essential for refining our comprehension of spatial patterns and facilitating a more thorough analysis of water deficits within the region.

The procedure can be schematized as follows:

1. IASI radiances are first fed to a level 2 (L2) prototype, whose accuracy has been extensively assessed in previous studies (Liuzzi et al. 2016; Guido Masiello, Carmine Serio, Venafra, Giuliano Liuzzi, et al. 2018). This scheme is able to simultaneously retrieve T_s, T_d and the surface emissivity spectrum, needed to calculate the indices of interest. It will be presented in Sec. 2.3;

2. a level 3 (L3) module (whose most up-to-date version can be found in De Feis, Guido Masiello, and Cersosimo 2020) is then used to remap and downscale the L2 data on a regular grid, as explained in Sec. 2.5.

As a clarification, in the context of this thesis L2 represents the sparse, physical parameters retrieved from IASI soundings (the latter considered as Level 1, L1, data), while L3 indicates those same quantities after being regularly gridded and upscaled.

To gain a deeper understanding of the significance of incorporating the IASI instrument in defining these indices, Section 2.2 provides context about its mission, technical features, and unique qualities that motivated its application in this thesis.

2.2 The IASI instrument

IASI, developed by the Centre national d'études spatiales (CNES) in France, is deployed on the Metop platforms as part of EUMETSAT's European Polar

System (EPS). Initially designed for meteorological purposes, IASI's primary aim is to provide vital information regarding temperature and water vapor profiles. Its spectral coverage ranges from 645 to 2760 cm^{-1}, with a sampling interval of 0.25 cm^{-1}, yielding a total of 8461 channels or spectral observations in every spectrum.

IASI operates as a cross-track scanner with 30 adjacent Fields of Regard (FOR) per scan, covering an angular range of $\pm 48.33\,^{\circ}$ on either side of the nadir. The FOR viewing geometry includes a 2×2 matrix of Instantaneous Fields of Views (IFOVs). Each individual IFOV has a diameter of $0.8394\,^{\circ}$, providing a ground resolution of 12 km per nadir at a satellite altitude of 819 km. The 2×2 IFOV matrix is centered on the viewing direction. At nadir, a FOR of 4 IASI IFOVs (or pixels) covers a square ground area of approximately $50 \times 50\,\mathrm{km}^2$. These corresponding FORs, within the 30 views, are $\pm 1.67\,^{\circ}$ on each side from the nadir direction. Further comprehensive details regarding IASI and its mission objectives can be found in Hilton et al. 2012.

2.3 From radiances to physical quantities: the ϕ-IASI code

The retrieval prototype, ϕ-IASI (Guido Masiello, Carmine Serio, Carissimo, et al. 2009; Masiello et al. 2012), employs an optimal estimation (OE) technique, combined with a fully analytical, monochromatic radiative transfer model (Rodgers 2000) to determine the thermodynamic state and chemical composition of the atmosphere. This method involves mathematically inverting the entire IASI spectrum, enabling the simultaneous retrieval of a state vector encompassing surface emissivity (ε) and surface temperature (T_s), as well as temperature (T), water vapor (Q), ozone (O), HDO, and OCS profiles. Additionally, it calculates the column amounts of CO2, N2O, CO, CH4, SO2, HNO3, NH3, and CF4. Validation studies for retrieving temperature, surface temperature and ozone can be found in Liuzzi et al. 2016; Umberto Amato et al. 2002; Annamaria Carissimo, De Feis, and Carmine Serio 2005; Guido Masiello, Carmine Serio, Deleporte, et al. 2013, and for emissivity in Guido Masiello, Carmine Serio, Venafra, Giuliano Liuzzi, et al. 2018; Guido Masiello, Carmine Serio, Venafra, DeFeis, et al. 2014. Nonetheless, the pertinent parameters for the current analysis include ε, T_s, and the atmospheric profiles for T and Q.

The ϕ-IASI code is comprised of two main modules:

- σ-IASI, a forward module yielding spectral radiances and analytical

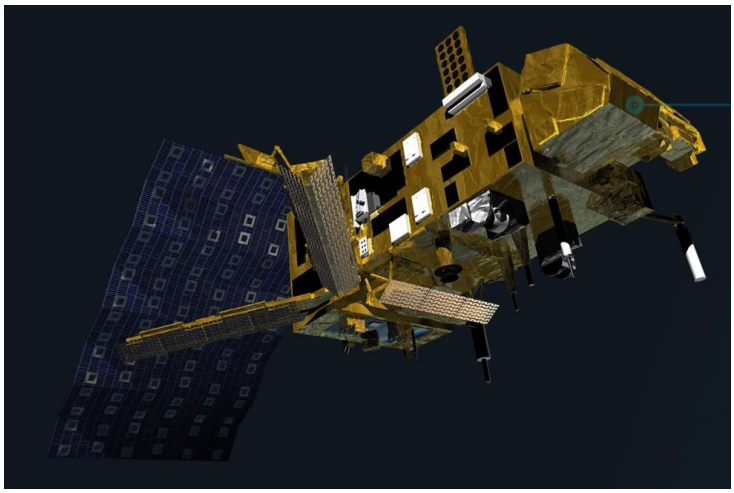

(a)

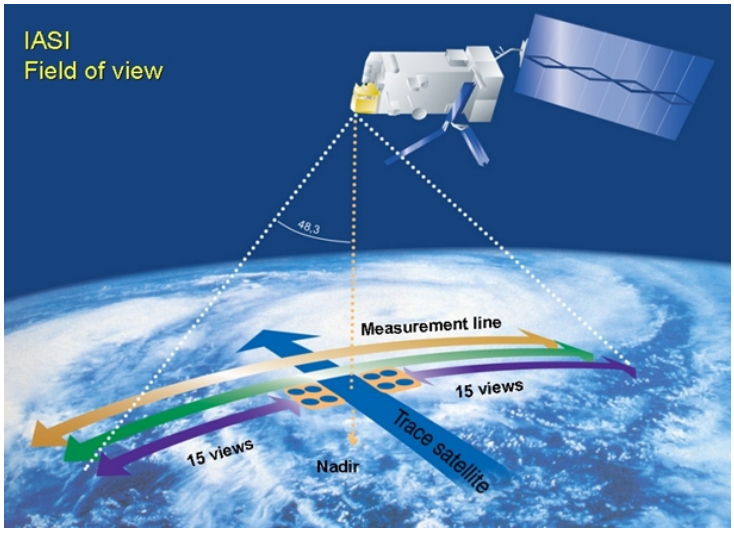

(b)

Figure 2.1: The IASI instrument (2.1a) and its FOV specifics (2.1b).

Jacobians concerning surface temperature, emissivity, and any atmospheric parameter, including the volume mixing ratio of the gases mentioned above;

- δ-IASI, an inversion scheme implementing an iterative algorithm for the optimal estimation of the thermodynamic state of the atmosphere and its composition;

The radiative transfer model employed is a fast model that utilizes a precomputed look-up table for optical depth calculations (Liuzzi et al. 2016;

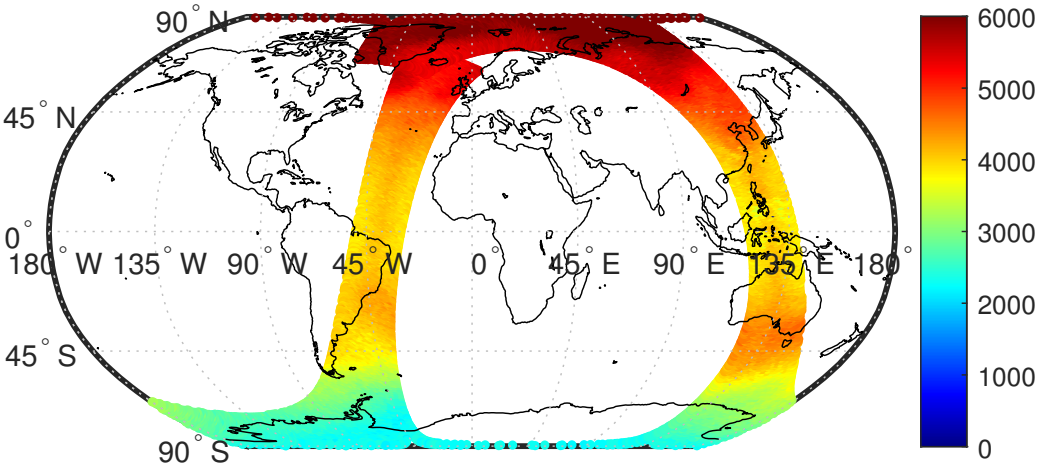

Figure 2.2: Example of IASI orbit (from July 2021)

Umberto Amato et al. 2002). This look-up table is generated from Line-by-Line Radiative Transfer Model (LBLRTM, Shephard et al. 2009; Alvarado et al. 2013, utilizing the line compilation *aer 3.2* (accessible at `http://rtweb.aer.com/line_param_frame.html`). The forward module calculates radiance by discretizing the radiative transfer equation on a fixed grid consisting of $N_L = 60$ pressure layers, covering the atmosphere from 1050 to 0.005 hPa.

The forward model provides spectral radiances and analytical Jacobians related to surface temperature, emissivity, and various atmospheric parameters, as described in previous studies (Guido Masiello, Carmine Serio, Venafra, Giuliano Liuzzi, et al. 2018; Guido Masiello, Carmine Serio, Venafra, DeFeis, et al. 2014; Guido Masiello and Carmine Serio 2013). These parameters include the volume mixing ratio of gases mentioned earlier. In its recent iteration (Liuzzi et al. 2016), σ-IASI also incorporates solar spectral radiation, which significantly contributes to the spectral range from 2000 to 2240 cm^{-1}. This interval contains crucial information for retrieving OCS (Carmine Serio, Guido Masiello, Mastro, et al. 2020; Camy-Peyret et al. 2017).

The inversion scheme, δ-IASI, employs an iterative algorithm for the optimal estimation of the atmosphere's thermodynamic state and composition. It conducts the mathematical inversion of the entire IASI radiance spectrum, consisting of 8461 channels, to simultaneously retrieve the atmospheric state vector mentioned above and here completely listed:

$$\mathbf{V} = (\varepsilon, T_s, T, Q, O, HDO, CO_2, N_2O, CO, CH_4, SO_2, HNO_3, NH_3, OCS, CF_4)$$

The inversion scheme processes IASI soundings acquired under clear sky con-

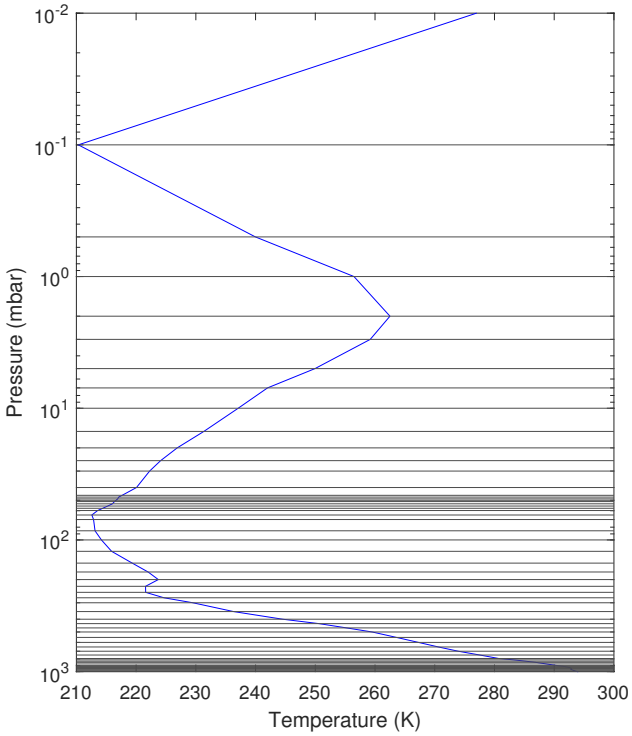

Figure 2.3: Location of the 60 pressure layers used by σ-IASI over Earth's atmosphere, together with a temperature profile sample retrieved by δ-IASI. Notice how they are more densely packed in both the lower troposphere and the stratosphere.

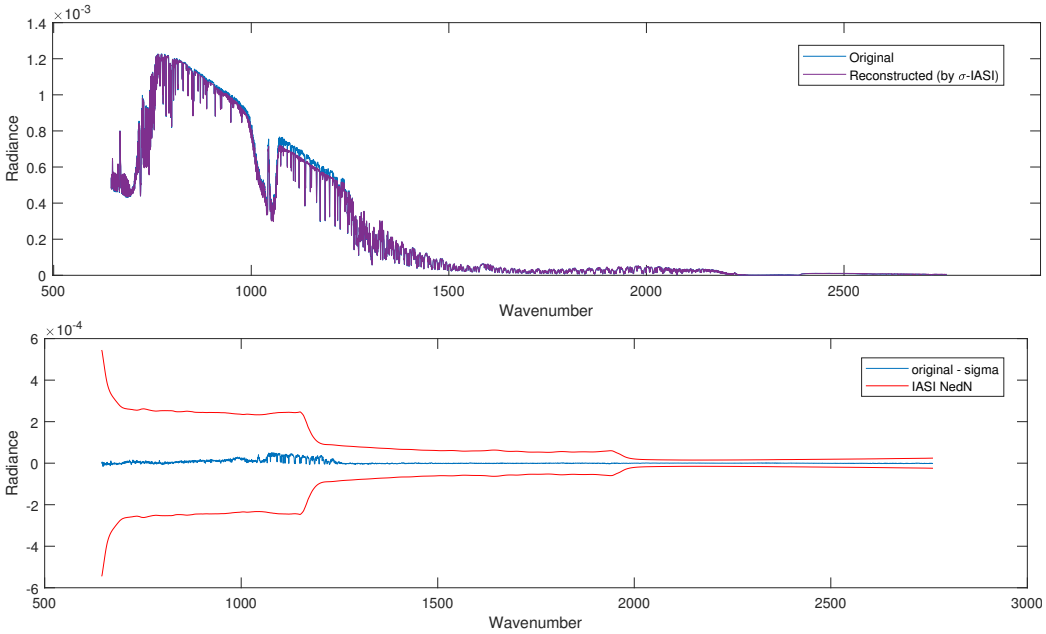

Figure 2.4: Upper panel: comparison between an actual IASI radiance spectrum (blue) and the same spectrum reconstructed by σ-IASI (violet). Bottom panel: difference between the two spectra (blue), together with IASI radiometric noise (red).

ditions. Clear sky soundings are identified using a standalone cloud detection scheme (Amato et al. 2014).

To improve efficiency, dimensionality reduction techniques are implemented in both the data space and the parameter space. Random Projection is used for data reduction, as detailed in Liuzzi et al. 2016; Camy-Peyret et al. 2017; Serio et al. 2019; Carmine Serio, Guido Masiello, and Giuliano Liuzzi 2016, while Principal Component transform is employed for parameter reduction, as shown in Carmine Serio, Guido Masiello, Mastro, et al. 2020; Guido Masiello, Carmine Serio, and Antonelli 2012; Carmine Serio, Guido Masiello, and Venafra 2019. These techniques optimize the retrieval process, enabling a more precise and efficient analysis of the atmospheric state and surface properties.

2.4 The indices: Emissivity Contrast Index (ECI) and Water Deficit Index (WDI)

2.4.1 Emissivity Contrast Index (ECI)

The notion of *emissivity contrast* was initially introduced by French, Schmugge, and Kustas 2000 to distinguish between senescent vegetation and bare soil. Starting from that, the Emissivity Contrast Index (ECI) has been defined as:

$$ECI = 1 - \delta\varepsilon, \tag{2.1}$$

where

$$\delta\varepsilon = \max(ChannelEmissivity) - \min(ChannelEmissivity) \tag{2.2}$$

represents the emissivity contrast French, Schmugge, and Kustas 2000, calculated as the disparity between the maximum and minimum emissivity values among the five spectral bands listed in Tab. 2.1.

In the context of this thesis work, ECI is calculated from the IASI retrieval of the emissivity spectrum, which shares the same spectral range, coverage, and sampling as the IASI spectrum. To simplify the emissivity spectrum's complexity, a suitable averaging process was applied, resulting in the derivation of five mean emissivities (see Tab. 2.1).

Table 2.1: IASI-retrieved emissivity bands used to compute ECI, together with the specific land cover type they are most sensitive to. The colors of the rows are meant to mirror the respective colored squares in Fig. 2.5.

IASI Band	Sensitivity
800-830 cm^{-1}	Vegetation (green or senescent)
900-1000 cm^{-1}	Green vegetation
1000-1100 cm^{-1}	Vegetation (green or senescent)
1100-1200 cm^{-1}	Reststrahlen band of Quartz (bare soil and desert sand)
2000-2200 cm^{-1}	High green/dry vegetation contrast

These specific channels (4.8, 8.6, 9.7, 10.8 and 12.1 μm) were selected due to their high sensitivity to bare, green, and senescent vegetation (see both Tab. 2.1 and Fig. 2.5). The first one exhibits a high contrast between

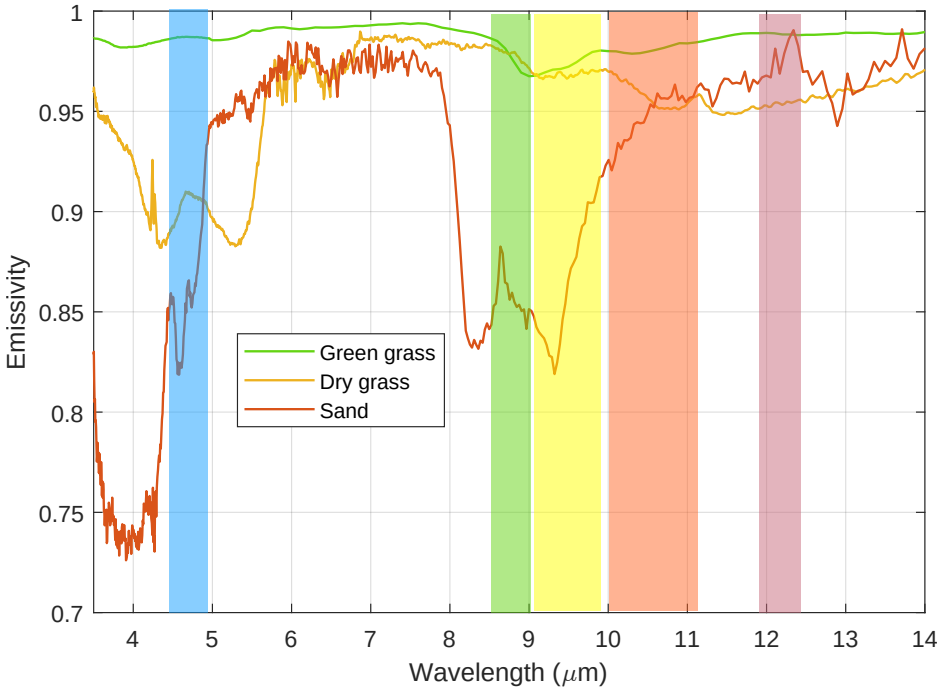

Figure 2.5: Emissivity spectral signatures of sand (red), dry grass (yellow) and green grass from the MODIS UCSB Emissivity Library (at `https://icess.eri.ucsb.edu/modis/EMIS/html/em.html`), plotted over the TIR bands used to compute ECI from the IASI emissivity spectrum (colored squares): notice the presence of the 4.8 μm channel, a peculiarity of the IASI instrument.

green and dry vegetation, which is essential in densely vegetated areas such as forests, which may present water stress while still preserving much of their canopy. The second channel shows a higher sensitivity to barren surfaces due to the pronounced quartz Reststrahlen effect. This characteristic makes it particularly valuable for identifying areas with desert sand or bare soil. The other three bands are primarily influenced by senescent or green vegetation cover and serve as auxiliary information providers about the presence of vegetation in general. Moreover, utilizing channels in the long-wave spectral range exclusively offers an advantage, as they are less affected by background aerosol contamination(Guido Masiello, Cersosimo, et al. 2020; Moparthy, Carrer, and Ceamanos 2019).

Due to their definitions, both ECI and NDVI carry consistent meanings: higher values indicate greener conditions, whereas lower values suggest brown or less vegetated areas. In theory, ECI falls within the range of [0, 1], although natural land features are anticipated to exhibit values around [0.5,

0.7]. Water, on the other hand, typically has a contrast of about 0.01 with an ECI of approximately 0.99. Green vegetation tends to have a very high emissivity due to its structured nature and water content, resulting in an ECI ranging between 0.98 and 1. Senescent or dry vegetation, with its variable emissivity depending on factors such as cover type and dryness, is expected to yield an ECI between 0.94 and 0.98. Desert sand and arid soil, on the other hand, are likely to have an ECI ranging from 0.5 to 0.8.

As an illustration of the comparison between ECI and NDVI, Fig. 2.6 displays ECI maps calculated for August 2017 over Southern Italy, alongside the corresponding monthly maps for MODIS NDVI. The substantial reduction in vegetation cover, caused by the impactful heatwave of summer 2017 over the Mediterranean area, is clearly evident in both maps and will be thoroughly analyzed in chapter 3.

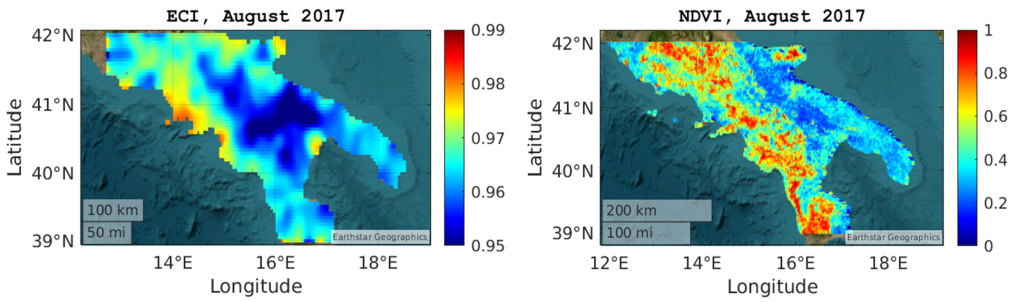

Figure 2.6: ECI and MODIS NDVI maps for August 2017 over Southern Italy.

2.4.2 Water Deficit Index (WDI)

The IASI-based water deficit index has been defined as:

$$WDI = T_s - T_d. \tag{2.3}$$

Using δ-IASI, the temperature (T) and specific humidity (Q) profiles can be retrieved, but only the values corresponding to the lowest atmospheric layer ($1005 - 1013\,\mathrm{hPa}$), denoted as T_1 (in K) and Q_1 (in Kg) are used to calculate the dew point temperature close to the surface. The pressure at this specific layer was labeled as P_1 (in hPa). The surface temperature (T_s) was also obtained as an output of the L2 inverse scheme. To calculate the dew point temperature (T_d), the actual water vapor pressure (P_w) and the

saturation water vapor pressure (P_{ws}) must both be determined. The actual water vapor pressure (P_w) can be computed from Q_1 using the following formula:

$$P_w = \frac{R_w}{R_{air}} P_1 Q_1 10^{-3}, \tag{2.4}$$

where $R_w = 461.5\,\mathrm{JK^{-1}Kg^{-1}}$ and $R_{air} = 286.9\,\mathrm{JK^{-1}Kg^{-1}}$ denotes the specific gas constants of water vapor and air. Huang 2018 suggests to calculate P_{ws} as:

$$P_{ws} = \frac{\exp(a_1 - \frac{a_2}{t_1 + a_3})}{(t_1 + a_4)^{a_5}}, \tag{2.5}$$

with $t_1 = T_1 - 273.15$ (to express temperature in °C) and $a_1 = 34.494$, $a_2 = 4924.99$, $a_3 = 237.1$, $a_4 = 105$ and $a_5 = 1.57$ are fit parameters. Eq. (2.5) is applicable when $t_1 > 0$ (vapor pressure of water). Using both Eq. (2.4) and (2.5), relative humidity (rh) can be computed as:

$$rh = \frac{P_w}{P_{ws}}. \tag{2.6}$$

Lastly, Magnus formula (Sonntag 1990) is used to calculate t_d (i. e. T_d in $^\circ C$):

$$t_d = \frac{c\gamma(T, rh)}{b - \gamma(T, rh)} \tag{2.7}$$

where

$$\gamma(t_1, rh) = \ln(rh) + \frac{bt_1}{c + t_1} \tag{2.8}$$

and $b = 17.62$ (dimensionless), $c = 243.12\,^\circ\mathrm{C}$.

WDI can be calculated using temperatures in either K or $^\circ C$. However, the computation of the dew point temperature, as shown in Eq. (2.7), must be carried out in $^\circ C$ before converting it to K. WDI can thus be more generally defined as follows:

$$WDI = T_s - T_d = t_s - t_d. \tag{2.9}$$

according to the unit of measure to be used.

This parameter is valuable in understanding water stress or deficit during prolonged periods of drought or heatwaves when considering a vegetated or

cropped surface. This is because vegetation releases water into the atmosphere through transpiration, which involves the conversion of liquid water in plant tissues into vapor, subsequently released into the atmosphere (Allen et al. 1998). This is why in summer, particularly during dry conditions, high WDI values are expected due to a significant temperature difference between the surface and the adjacent dew point temperature. Conversely, lower values can be anticipated in winter.

Transpiration, akin to direct evaporation, is shaped by factors like solar radiation, wind, and the vapor pressure gradient at the surface-atmosphere junction. Hence, in the development of a satellite-based index to measure water deficit, careful consideration of elements such as solar radiation, air temperature, humidity, and wind speed is paramount for precise evaluation and assessment. In the case of WDI, as Eq. (2.3) suggests, T_s takes into account the energy supplied by the sun, which leads to a swift rise in the land surface temperature. At the same time, T_d represents the contribution of both air temperature and humidity. Introducing the influence of wind presents challenges. Nevertheless, during droughts and heat waves, the spatial gradient and wind intensity decrease. Meteorological conditions conducive to summer heatwaves are characterized by air subsidence and low-pressure gradients.

Emphasizing the co-occurrence of evaporation and transpiration is crucial, as distinguishing between these processes is challenging. Hence, the term "evapotranspiration" (see Fig. 2.7) is used to encompass the water exchange between vegetation and the air. Besides soil moisture availability, evaporation from cultivated land relies on solar radiation impact. As the crop grows, solar energy reaching the surface diminishes due to foliage or canopy shading, casting shadows below. Consequently, soil evaporation predominantly occurs when the crop is small or leaves are undeveloped. However, transpiration takes over as the primary process once the crop and leaves are well-developed, fully covering the soil.

As was done with ECI, different situations of water stress can be highlighted by different values of WDI. Three main ranges can be distinguished:

- $WDI \gg 0$ - hot and dry meteorological conditions (e.g. during heat waves) encouraging evapotranspiration;
- $WDI \geq 0$ - war and humid atmospheric conditions, with air close to saturation, thus greatly limiting the evapotranspiration rate;
- $WDI < 0$ - water vapor condenses into liquid water at the surface ($T_s < T_d$).

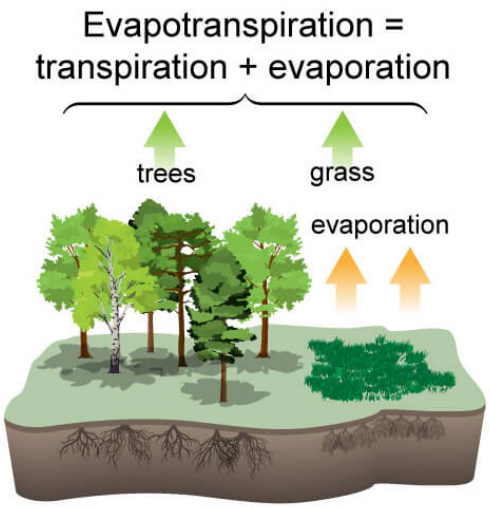

Figure 2.7: Infographic example of the evapotranspiration process.

2.5 From sparse data to high-resolution maps: an Optimal Interpolation strategy

The two-dimensional interpolation method used to generate L3 data was initially introduced by Carmine Serio, Guido Masiello, Pasquariello, et al. 2022. This method integrates optimal and objective Gaussian interpolation techniques, leveraging the complete retrieval covariance matrix obtained from the δ-IASI inverse module. This approach ensures precise estimation of each mapped quantity (Carmine Serio, Guido Masiello, Pasquariello, et al. 2022).

This L3 scheme employs a suitable method to transform L2 data obtained from a sparsely populated and non-uniform grid into L3 products on a standardized grid. To comprehend the significance of this process, Figure 2.8 illustrates a collection of IASI pixels for a L2 *wdi* retrieval, alongside the outcome of the L3 interpolation scheme. In other words, the initial L2 data (approximately 12 km for each pixel) has been mapped onto a regular grid with a resolution of 0.05° through the L3 interpolation scheme

As thoroughly described in Carmine Serio, Guido Masiello, Pasquariello, et al. 2022, when considering $\hat{x}_i$ as the L2 products at a specific 2-D position denoted by the latitude-longitude pair (θ_i, φ_i), the interpolated value $\bar{x}$ can be computed utilizing the following equation, as outlined in the same reference (Carmine Serio, Guido Masiello, Pasquariello, et al. 2022):

$$\bar{x} = \left(\sum_{1=1}^{N} \frac{p_i}{\sigma_i^2} \right)^{-1} \sum_{1=1}^{N} \frac{p_i}{\sigma_i^2} \hat{x}_i \tag{2.10}$$

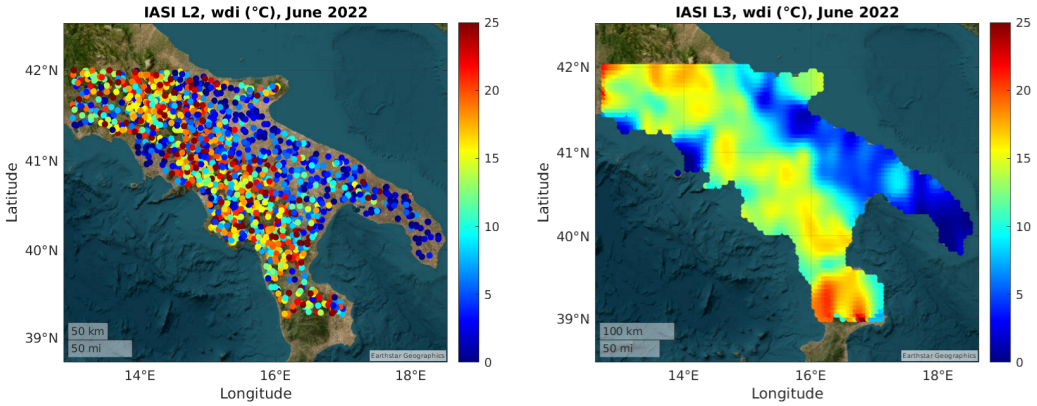

Figure 2.8: L2 IASI WDI for June 2022 (on the left) and the corresponding L3 product (on the right).

where σ_i^2 is the variance of the retrieval and N is the number of retrieved values. The interpolation process is deemed optimal as it integrates weights determined by σ_i^2. Although it is feasible to expand the scheme to encompass all N data points, it is often more pragmatic to restrict the impact of L2 data on a particular location by employing a characteristic length scale. To accomplish this, Carmine Serio, Guido Masiello, Pasquariello, et al. 2022 introduces a Gaussian weight p_i:

$$p_i = \exp\left(-\frac{1}{2}\frac{d^2(\bar{x}, \hat{x}_i)}{d_{th}^2}\right) \tag{2.11}$$

where $d(\bar{x}, \hat{x}_i)$ denotes the Euclidean distance between $\bar{x}$, $\hat{x}_i$, while d_{th} represents a suitable length scale.

By incorporating Gaussian weights, the interpolation scheme becomes objective, and the spatial sampling of the L3 products is determined by the length scale d_{th}. In practical applications, Carmine Serio, Guido Masiello, Pasquariello, et al. 2022 suggests fixing d_{th} based on the density of the L2 data: "especially when accumulating L2 data over an extended period (e.g., one month), $d_{th} = 0.1°$ can be employed, approximately corresponding to the IASI IFOV diameter at a nadir of 12 km".

It is important to note that IASI soundings can be considered uncorrelated in both time and space. Consequently, the application of the variance propagation rule enables the calculation of the variance for the interpolated value:

$$var(\bar{x}) = \left(\sum_{1=1}^{N} \frac{p_i}{\sigma_i^2} \right)^{-1} \sum_{1=1}^{N} \frac{p_i}{\sigma_i^2} \tag{2.12}$$

The results presented in Fig. 2.9 showcase maps of ECI and WDI spanning one month, alongside their respective data densities. These maps were generated using a sampling resolution of $0.05° \times 0.05°$. While this approach sacrifices temporal resolution, it enhances spatial sampling and precision in the resulting product.

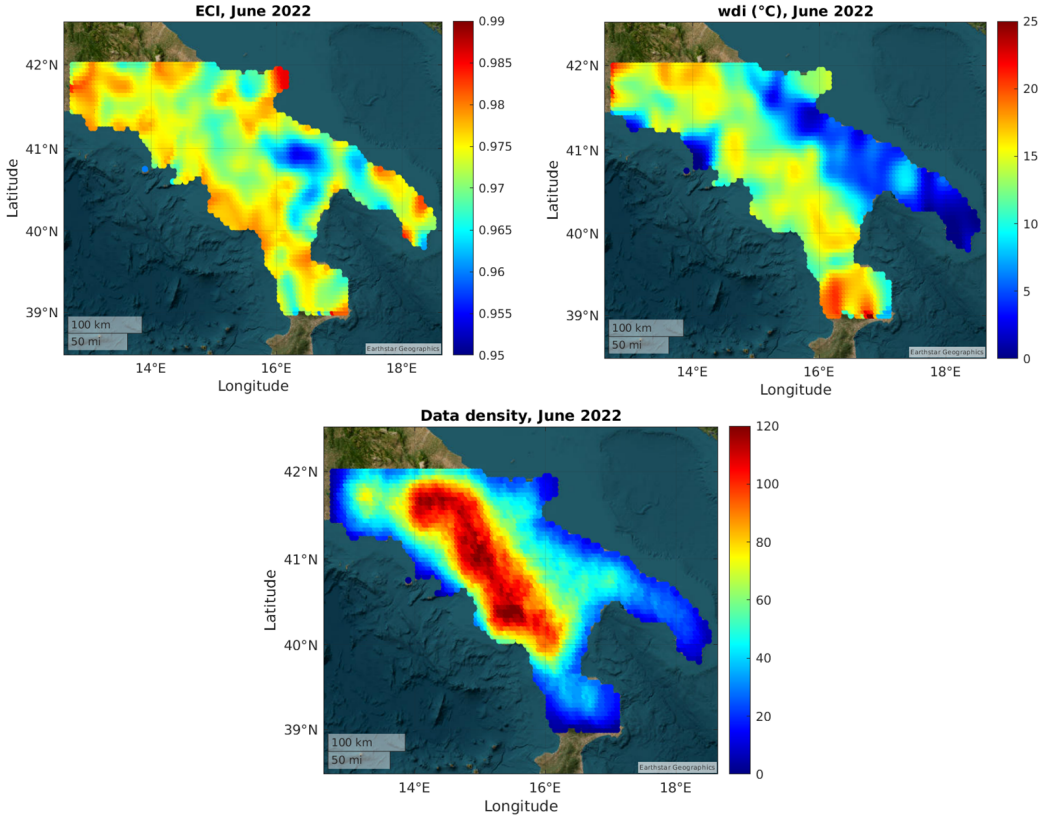

Figure 2.9: Maps of ECI and WDI for June 2022 (upper panel) and the relative IASI L2 data density for the same month (lower panel).

Chapter 3

Validation: Southern Italy over the last decade

In this chapter, the theoretical basis presented in Chapter 2 is applied and validated over a specific geographic area: Southern Italy. It is demonstrated how both ECI and WDI are able to highlight major water stress in woodlands over the Apennine chain due to several summer heat waves, which heavily impacted the Mediterranean basin during the period 2014-2022. Moreover, correlation with other remote-sensed indices is investigated: the analysis is conducted both on a wider (the target area) and on a local scale, considering two specific forested areas in the Basilicata region suffering from long-lasting water stress, thus of particular interest in the context of this thesis research work.

3.1 Description of the target area

The study area depicted in Fig. 3.1 covers a portion of southern Italy. Notably, the Apennines exhibit forested regions, while the eastern part of the region is predominantly characterized by agricultural landscapes, as evident from the 2018 CORINE Land Cover data (available at `https://land.copernicus.eu/pan-european/corine-land-cover`) included in the figure. In the study area's climate is Mediterranean, characterized by dry and warm summers that have become particularly noticeable during the last decade. The dots on the map indicate the two stressed woodlands examined in this study: San Paolo Albanese (40.02° N, 16.34° E, elevation range: 950–1050 m.a.s.l.) and Gorgoglione (40.40° N, 16.14° E, elevation range: 800–850 m.a.s.l.). These areas are currently facing tree mortality due to prolonged drought conditions (Rita et al. 2020; Ripullone et al. 2020; Colangelo et al.

2018).

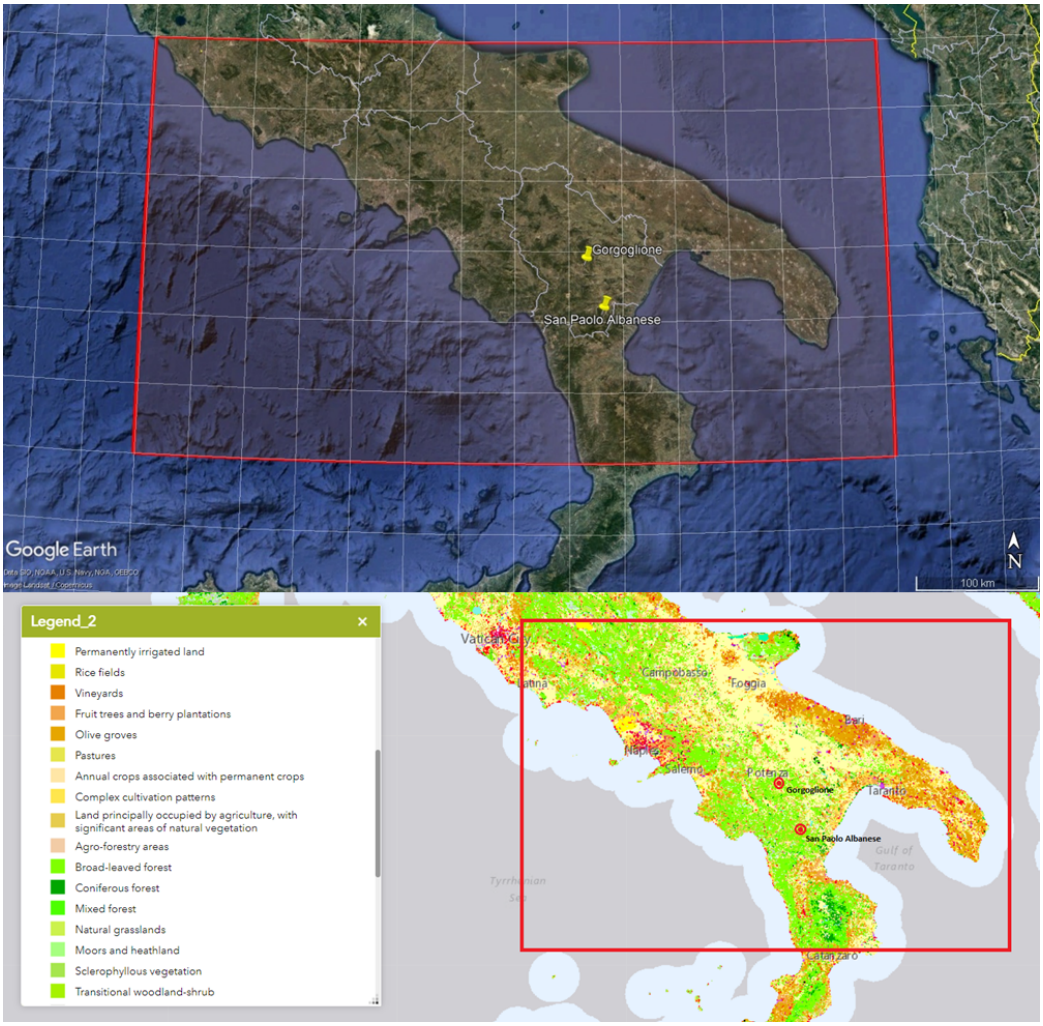

Figure 3.1: The designated study area is outlined by the red square, and it includes the two analyzed locations (marked with yellow pins at the top and red circles at the bottom). The 2018 CORINE Land Cover map emphasizes the presence of forests in the region.

In the San Paolo Albanese site, the vegetation consists of a dense forest primarily composed of *Quercus frainetto Ten.* with a stand density of 348 trees/ha. Studies on the most affected stands have revealed that more than half of the mature specimens exhibited signs of death, while around 15% have recently perished (Ripullone et al. 2020). Conversely, the Gorgoglione woodland represents a significantly mixed forest, boasting an average density of approximately 600 stems/ha. The prevalent species in this area are *Quer-*

cus cerris L. (71%), succeeded by *Quercus pubescens L.* (25%), and other deciduous tree species (4%), albeit at a lower density (Colangelo et al. 2018).

The two primary tree species under study, namely *Quercus cerris L.* and *Quercus pubescens L.*, have exhibited symptoms of decline induced by drought since the early 2000s. These symptoms include shoot dieback, summer leaf loss, withering, growth decline, and high mortality rates. According to local reports in the study area, approximately 450 hectares of oak trees were affected by annual mortality. The incidence of the decline syndrome led to an increase in mortality rates from 5% to 10% between 2002 and 2004 (Ripullone et al. 2020).

3.2 Products used for validation

As for the non-IASI data used for the correlation analysis, Tab. 3.1 provides a detailed list. Overall, two groups of products were considered: LAI, FAPAR, FVC and ET from SEVIRI and SSM from Copernicus Sentinel-1. The SEVIRI products are provided by EUMETSAT Satellite Application Facility on Land Surface Analysis (LSA SAF), while the SSM data are part of Copernicus Global Land Service (CGLS) products collection.

Table 3.1: Products used for the correlation analysis.

Product	Sensor/Platform	Spatial Res.	Temporal Res.
MTLAI [LSA-424]	SEVIRI/MSG	3 km	10-daily
MTFAPAR [LSA-452]	SEVIRI/MSG	3 km	10-daily
MTFVC [LSA-422]	SEVIRI/MSG	3 km	10-daily
DMET [LSA-312]	SEVIRI/MSG	3 km	daily
SSM	C-SAR/Sentinel-1	1 km	daily

3.3 Results

Monthly maps of ECI and WDI for 2017 and 2022 are presented in Figs. 3.2-3.3 and 3.4- 3.5, respectively. It is reasonable to expect a low WDI value and an ECI close to 1 for the Apennine chain, renowned for its lush broad-leaved deciduous forests, especially when vegetation is adequately water-sustained, a condition prevalent during the flourishing periods of spring and summer. However, a discernible drop in ECI becomes evident in the woodland areas

from June to September, while WDI shows a consistent increase during the same period. Specifically, in forested regions, WDI was above approximately 10°C, while ECI reached its minimum values, around 0.95.

This outcome is unsurprising given that the Mediterranean region experienced severe heatwaves in both years. The significant drought in May 2022 is apparent, although its overall impact on the subsequent months appears to be less severe compared to 2017 and 2021. In general, both WDI and ECI indicate an escalation in water deficiency due to these heatwaves, leading the vegetation to transition into its senescent phase earlier than usual. Figs. 3.7 and 3.6 depict the indices for the summer months of 2017, 2020, 2021, and 2022, reaffirming a cyclical pattern of intense water stress. Summer 2020 stands out as being relatively less hot and dry than the other three years, with June 2020 being milder. In contrast, June 2022 exhibits a combination of higher WDI and lower ECI values, making it the hottest and driest June of the four years.

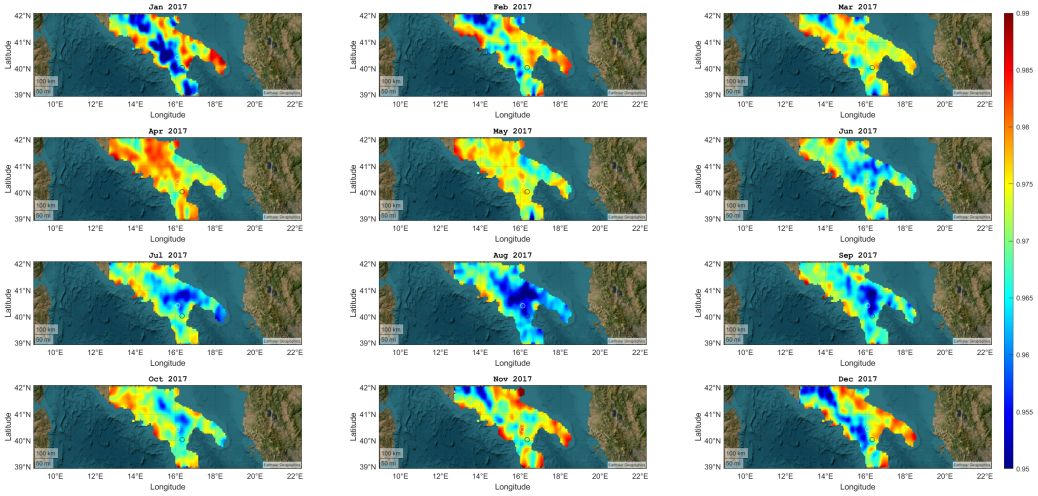

Figure 3.2: Maps of ECI for 2017.

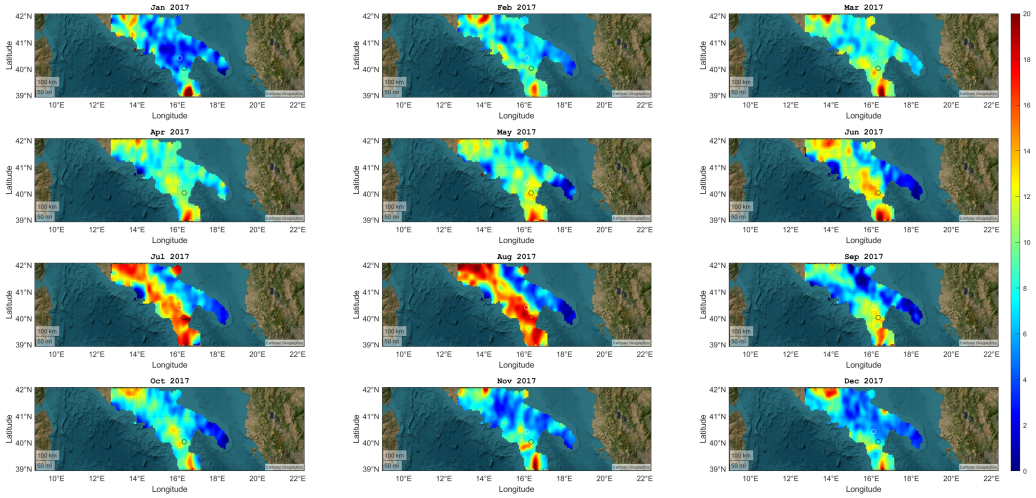

Figure 3.3: Maps of WDI for 2017.

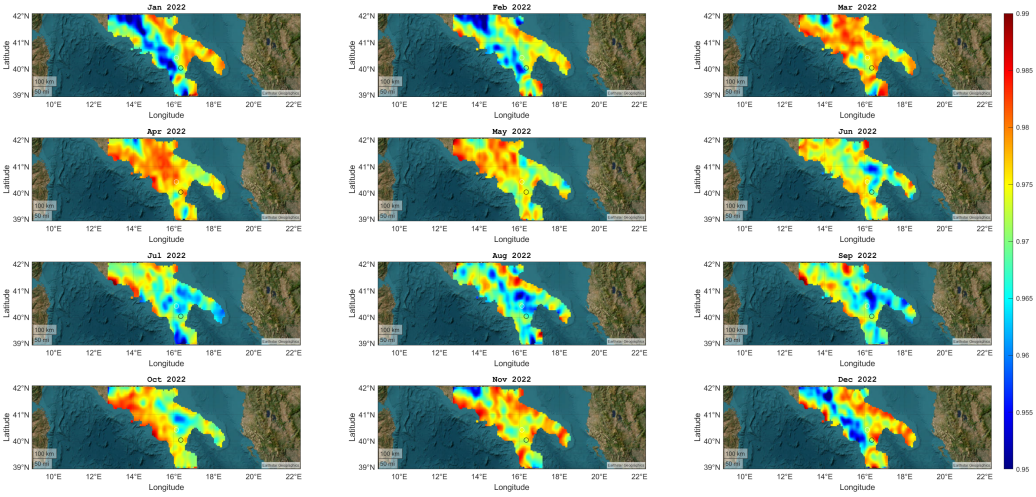

Figure 3.4: Maps of ECI for 2022.

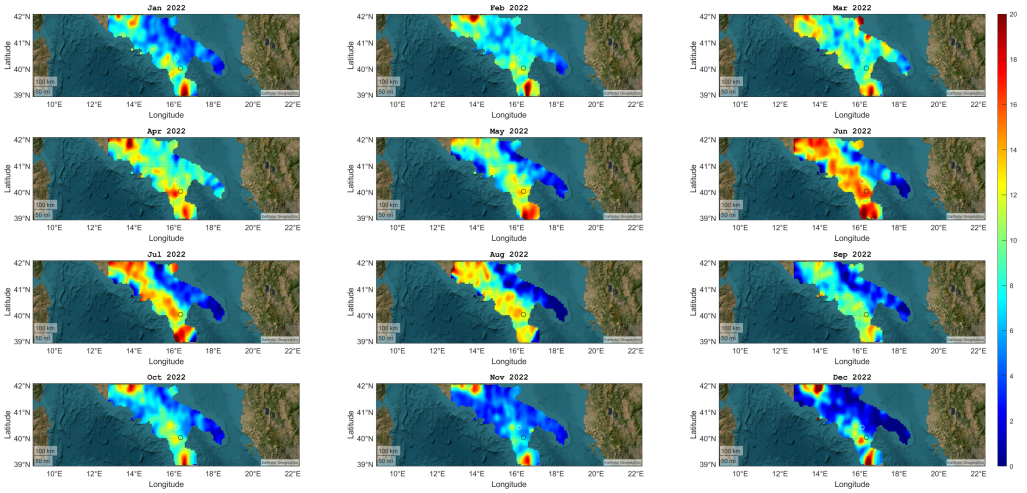

Figure 3.5: Maps of WDI for 2022.

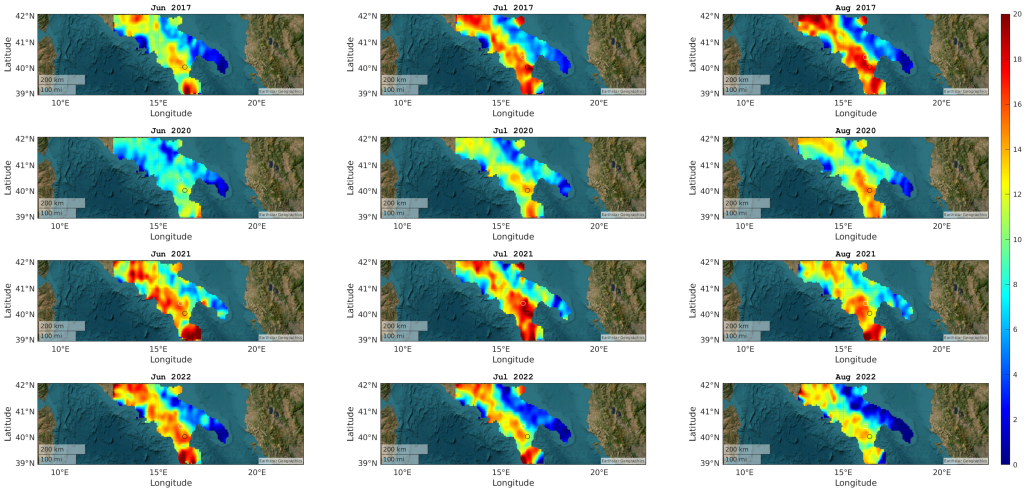

Figure 3.6: Maps of WDI for June, July and August 2017, 2020, 2021 and 2022.

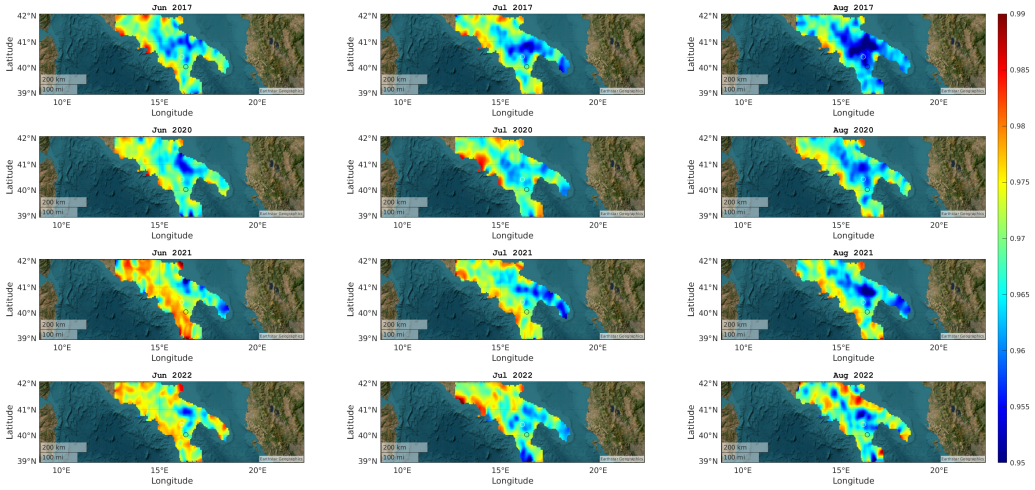

Figure 3.7: Maps of ECI for June, July and August 2017, 2020, 2021 and 2022.

3.4 Comparison with other indices

A comparison of ECI, WDI, and MODIS NDVI (1 km) on both broader (Fig. 3.8) and local (Figs. 3.9-3.10) scales reveals that NDVI fails to effectively highlight the devastating impact of the 2017 heatwave. Throughout the heatwave period, NDVI maintains a relatively stable level, indicating limited sensitivity to the severity of the heatwave. While it accurately outlines woodland areas along the Apennine mountain range, it lacks the capability to capture changes in surface water stress. In contrast, both ECI and WDI demonstrate changes that correspond to the expected pattern of increasing water scarcity, making them more reliable indicators in this context.

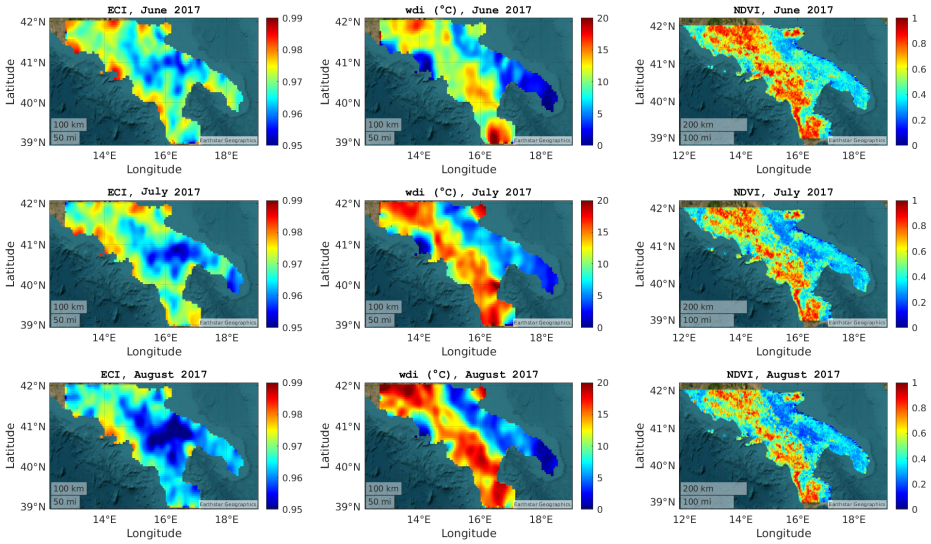

Figure 3.8: Maps of ECI, WDI and NDVI for June, July and August 2017.

To better understand how responsive ECI and WDI are to this phenomenon, a comprehensive study was carried out comparing these two indices with another group of indicators (SSM, LAI, FAPAR, FVC and ET) over the period from 2014 to 2022.

Fig. 3.11 presents monthly maps of ECI, WDI, and SSM for the summer months of 2017. While ECI and SSM appear to decrease over time, WDI shows the opposite trend. This (anti)correlation indicates that an increase in WDI corresponds to a rapid loss of water from the surface into the atmosphere, leading to a decrease in ECI and soil moisture. This suggests reduced water absorption by vegetation.

Examining this pattern at a local scale for the entire period of interest,

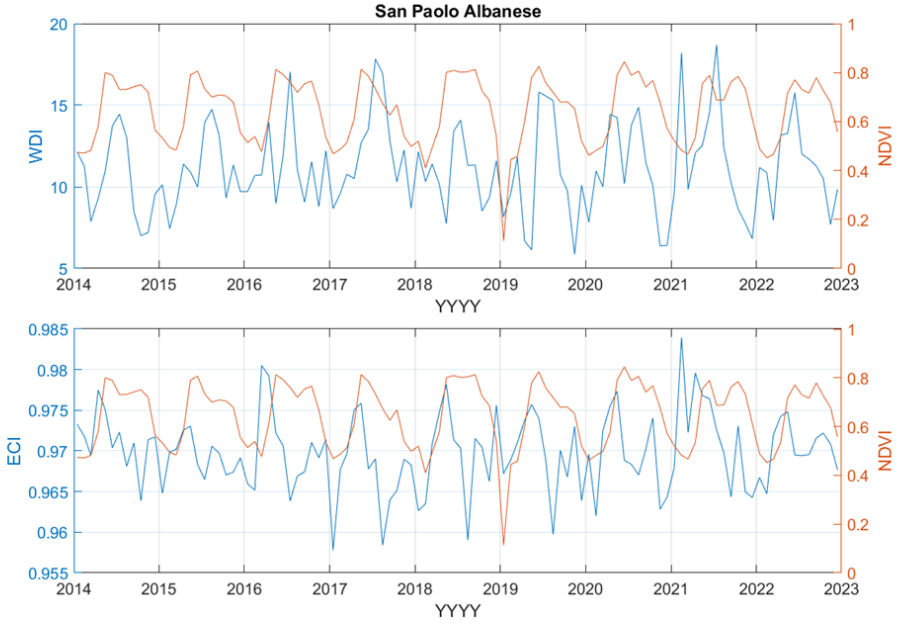

Figure 3.9: Temporal series of NDVI versus WDI and ECI for San Paolo Albanese.

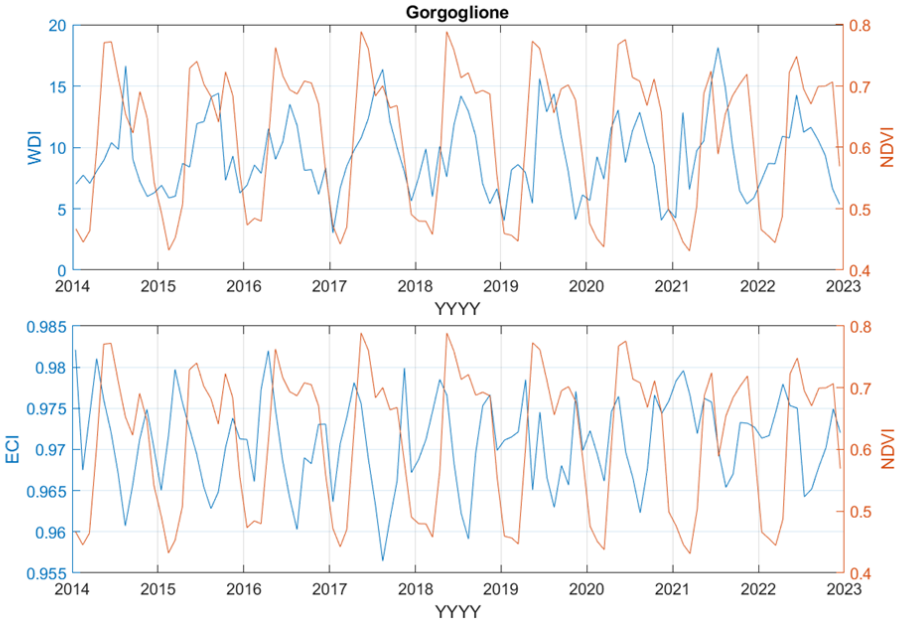

Figure 3.10: Temporal series of NDVI versus WDI and ECI for Gorgoglione.

Figs. 3.12- 3.13 allows for a better understanding of the previously observed trend, which is explicitly confirmed in Fig. 3.14. It is noteworthy that SSM

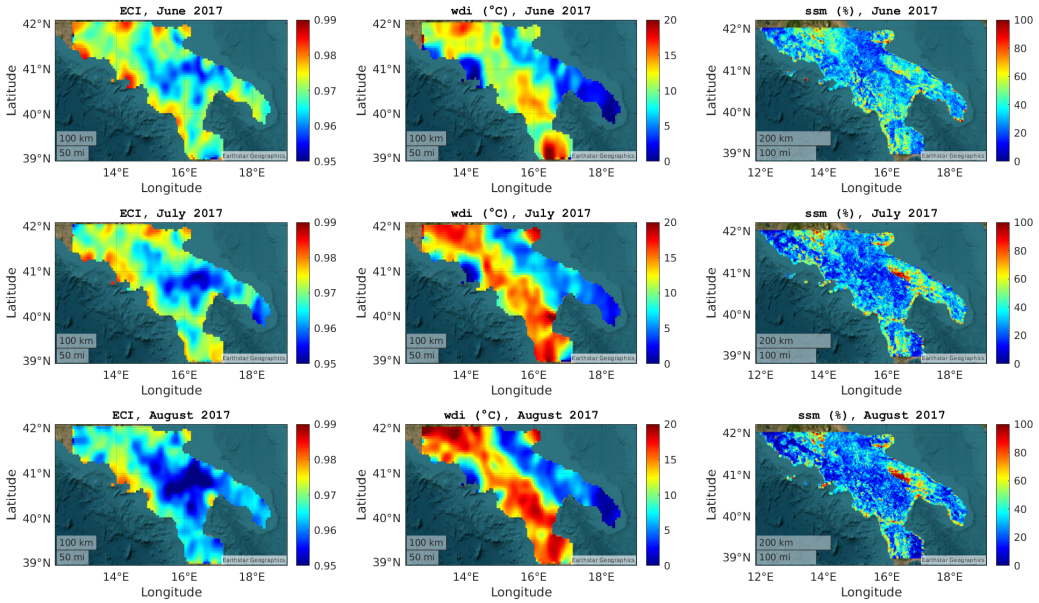

Figure 3.11: Maps of ECI, WDI and SSM for June, July and August 2017.

and ECI in both Gorgoglione and San Paolo Albanese exhibit their highest correlation value with a one-month lag (indicated as $\tau = 1$, following the methodology used in Carmine Serio, Guido Masiello, Pasquariello, et al. 2022, where linear correlation is calculated considering SSM(t) and ECI($t + \tau$)). A similar, albeit in terms of anticorrelation and only in San Paolo, relationship exists between SSM and WDI. This demonstrates that the decline in vegetation is linked to atmospheric conditions, subsequently leading to soil moisture loss.

Fig. 3.15 displays maps of ECI, WDI, and LAI for the summer of 2017, while the trends of these indices from 2014 to 2022 are illustrated in Figs. 3.16-3.17: when WDI increases (and ECI decreases), LAI diminishes, aligning with the expected scenario of heightened vegetation stress. During periods of intense heatwaves, trees often shed their leaves as a protective measure against excessive evapotranspiration. This adaptive mechanism is similar to how trees utilize it during seasons such as winter, when there is insufficient light to sustain photosynthesis (Le, Harper, and Dell 2023). Consistent with the decreasing trend of ECI and WDI, LAI experiences a decline from June to July. A reduction in LAI during summer, when there is ample light available for photosynthesis, is not typical in normal circumstances (Le, Harper, and Dell 2023).

Fig. 3.18 displays maps showing ECI, WDI, and FAPAR for the months of June, July, and August in 2017. In Figs. 3.19- 3.20, the monthly series

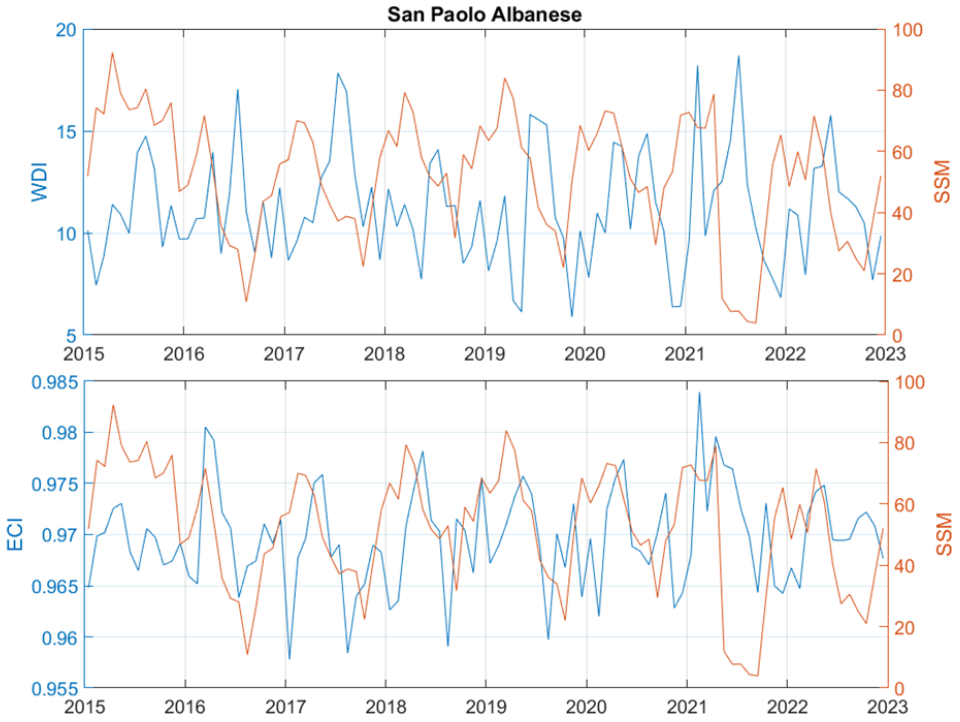

Figure 3.12: Temporal series of SSM versus WDI and ECI for San Paolo Albanese.

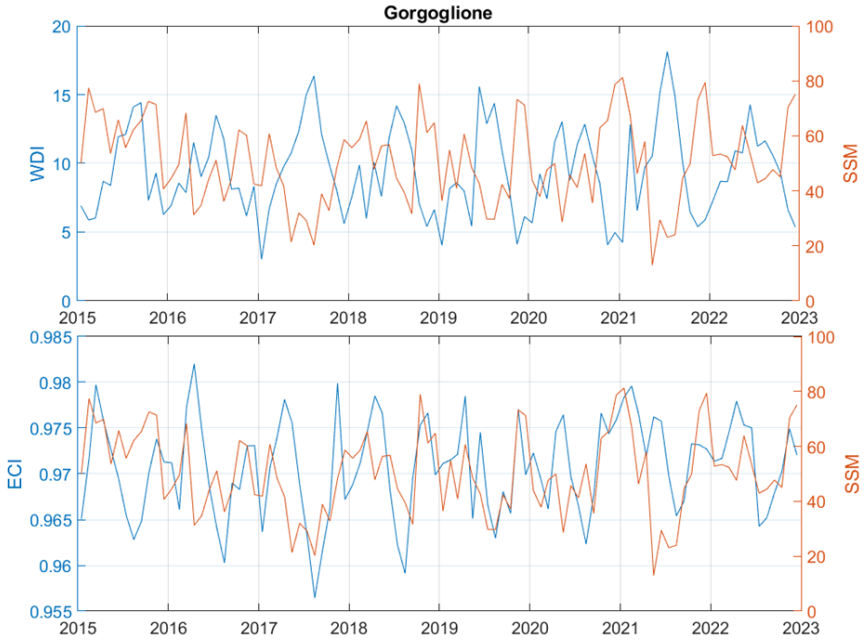

Figure 3.13: Temporal series of SSM versus WDI and ECI for Gorgoglione.

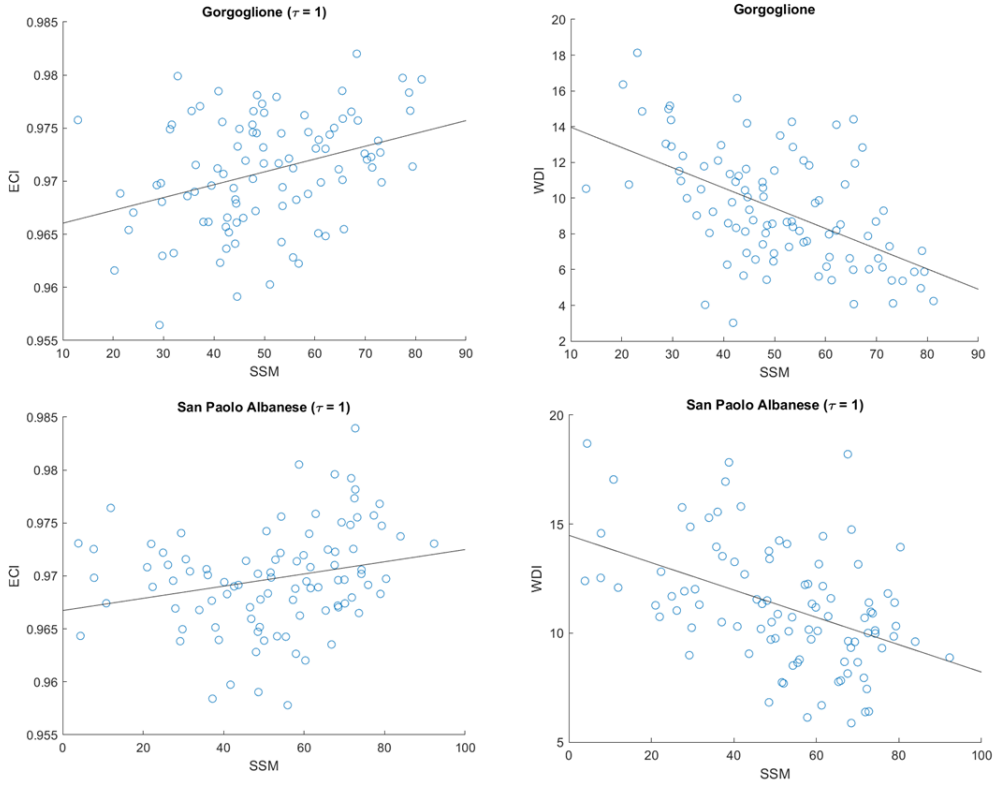

Figure 3.14: Correlation between SSM, ECI and WDI for Gorgoglione (upper panel) and San Paolo Albanese (lower panel).

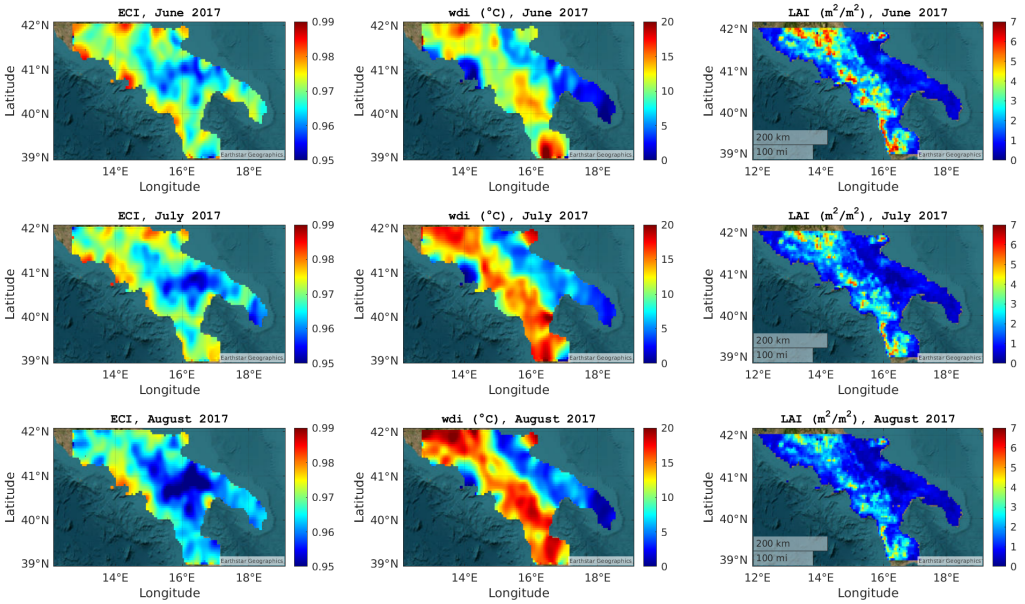

Figure 3.15: Maps of ECI, WDI and LAI for June, July and August 2017.

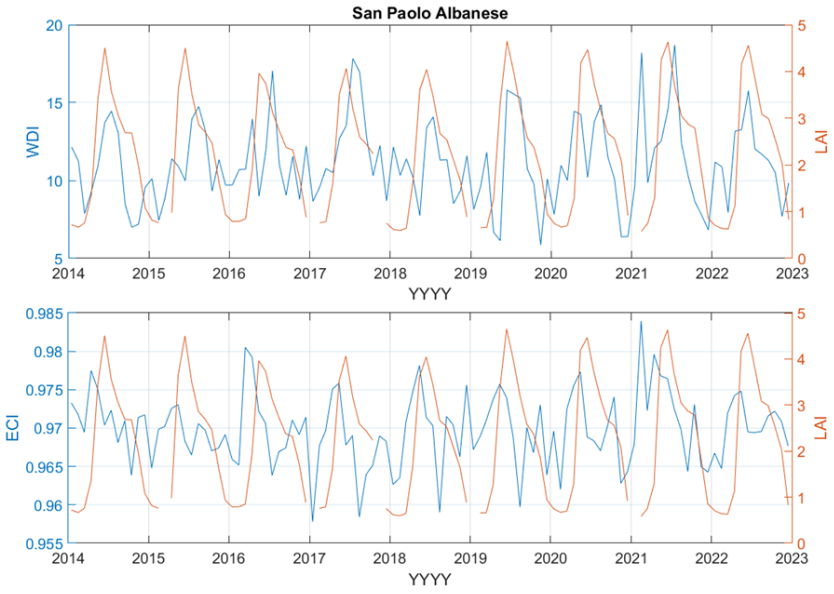

Figure 3.16: Temporal series of LAI versus WDI and ECI for San Paolo Albanese.

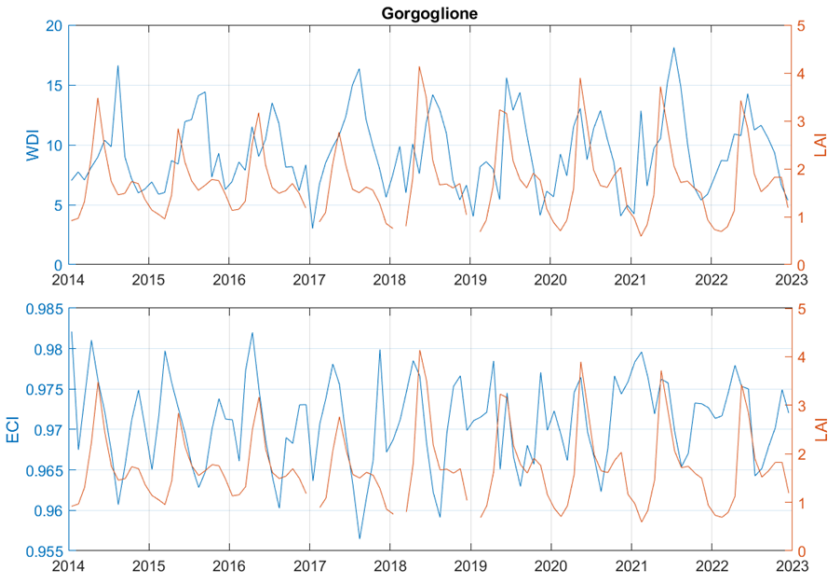

Figure 3.17: Temporal series of LAI versus WDI and ECI for Gorgoglione.

of these indices for Gorgoglione and San Paolo spanning from 2014 to 2022 are illustrated. Similar to the findings related to LAI, the same pattern emerges, but with even greater clarity: an increase in WDI and a decrease in ECI correspond to a significant reduction in FAPAR, indicating a decline in the radiation absorbed by vegetation. This reduction is a consequence of vegetation stress caused by water loss, which hampers the leaves' ability to absorb enough radiation for photosynthesis (Le, Harper, and Dell 2023).

Fig. 3.21 shows maps of ECI, WDI, and FVC for the months of June, July, and August in 2017. In Figs. 3.22- 3.23, the monthly series for Gorgoglione and San Paolo from 2014 to 2022 are displayed. The same kind of behaviour as LAI and FAPAR can once again be observed for FVC.

Fig. 3.24 presents a comparison between ECI, WDI, and ET for the summer of 2017. Correlation trends for San Paolo Albanese and Gorgoglione over the period 2014-2022 can be seen in Figs. 3.25- 3.26. Both WDI and ET exhibit a similar pattern, peaking during the summer months and declining in winter, as shown in Fig. 3.27. A high WDI value indicates an elevated rate of evapotranspiration, indicating increased water loss from trees into the atmosphere. The decreasing levels of soil moisture suggest a decline in water absorption by vegetation from the surface. The elevated values observed during summer cannot be solely attributed to warmer weather; they also reflect a reduction in water vapor exchange between the surface and the atmosphere. In contrast, ECI exhibits peaks during winter months and lower

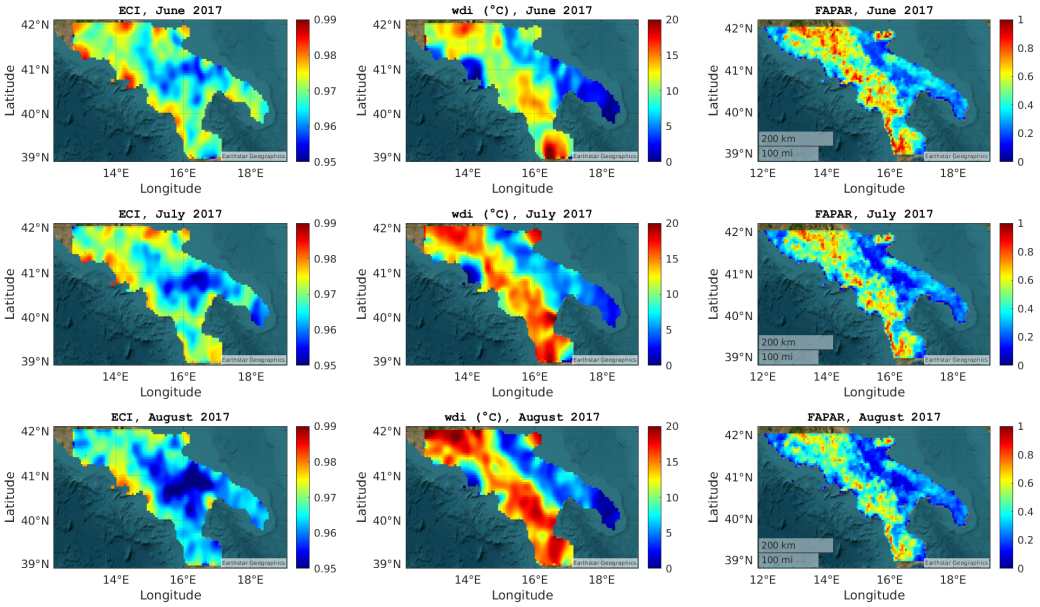

Figure 3.18: Maps of ECI, WDI and FAPAR for June, July and August 2017.

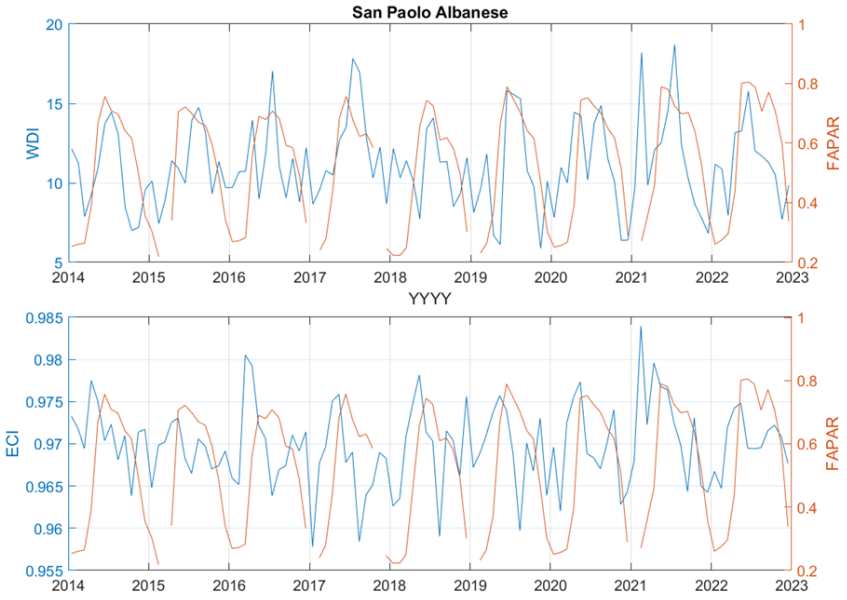

Figure 3.19: Temporal series of FAPAR versus WDI and ECI for San Paolo Albanese.

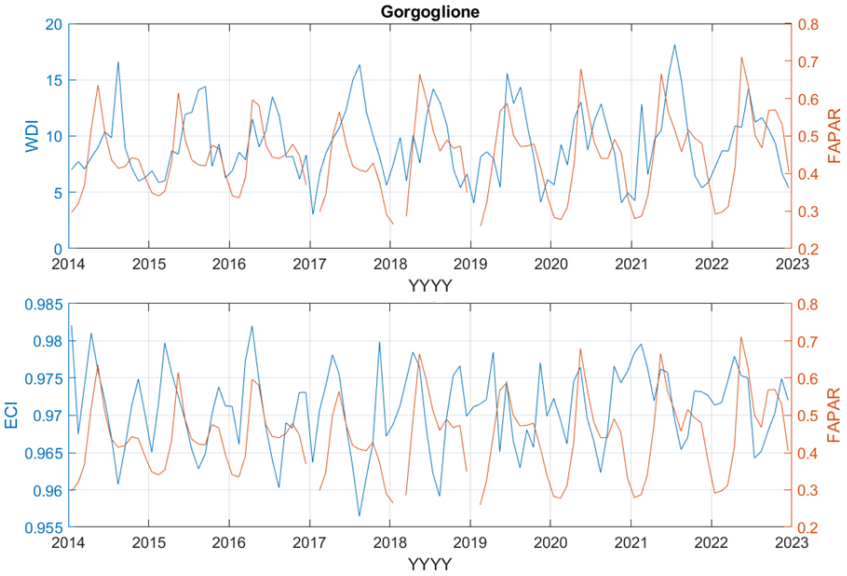

Figure 3.20: Temporal series of FAPAR versus WDI and ECI for Gorgoglione.

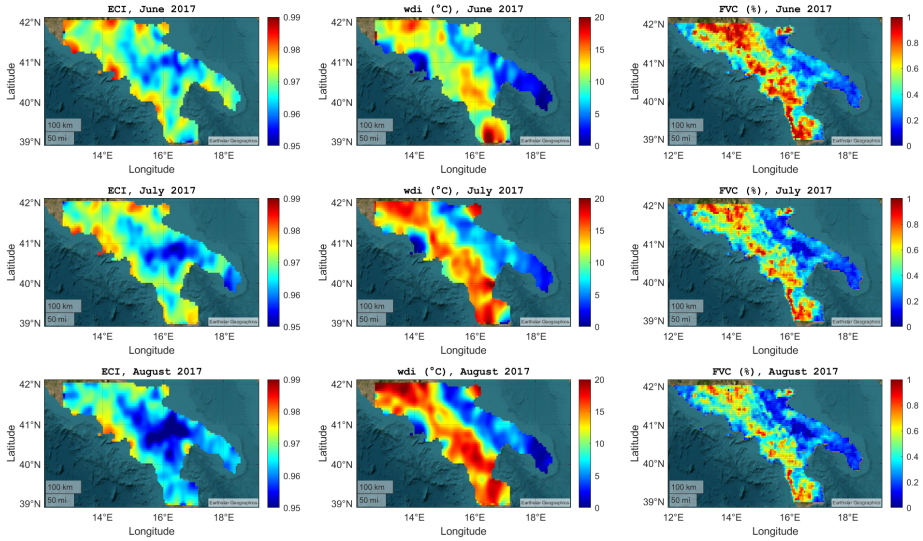

Figure 3.21: Maps of ECI, WDI and FVC for June, July and August 2017.

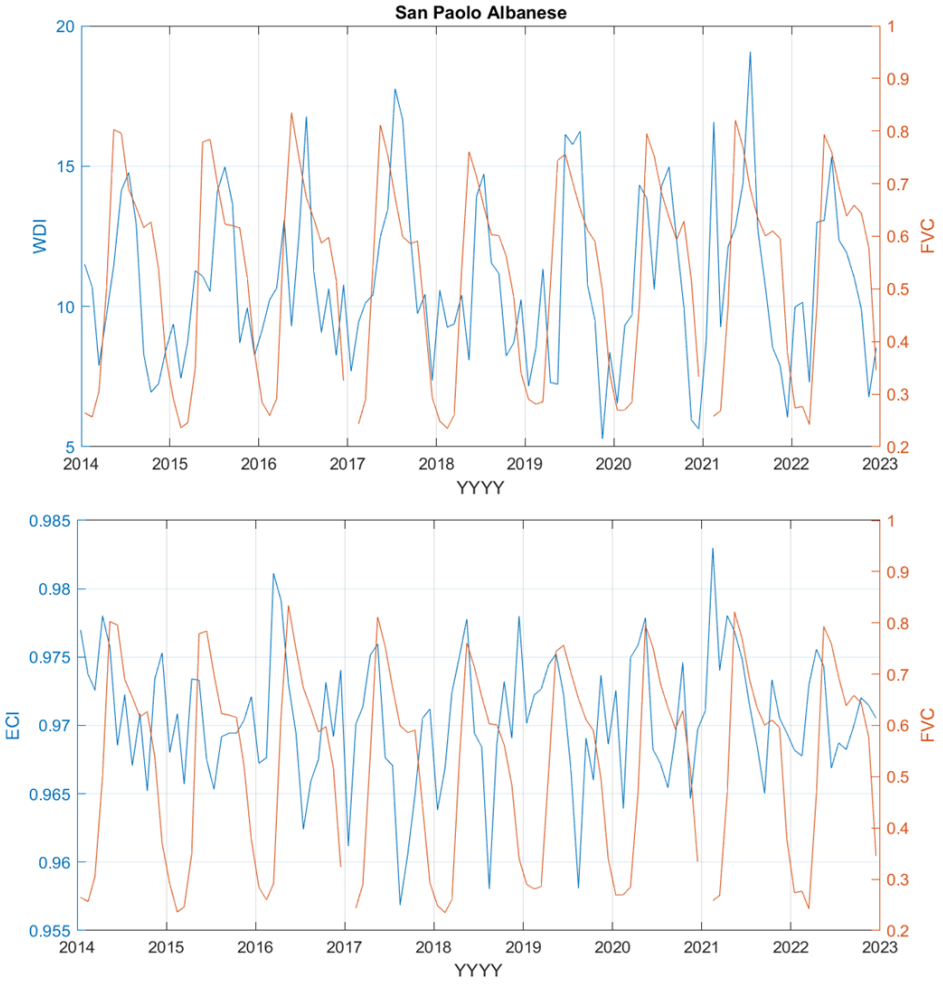

Figure 3.22: Temporal series of FVC versus WDI and ECI for San Paolo Albanese.

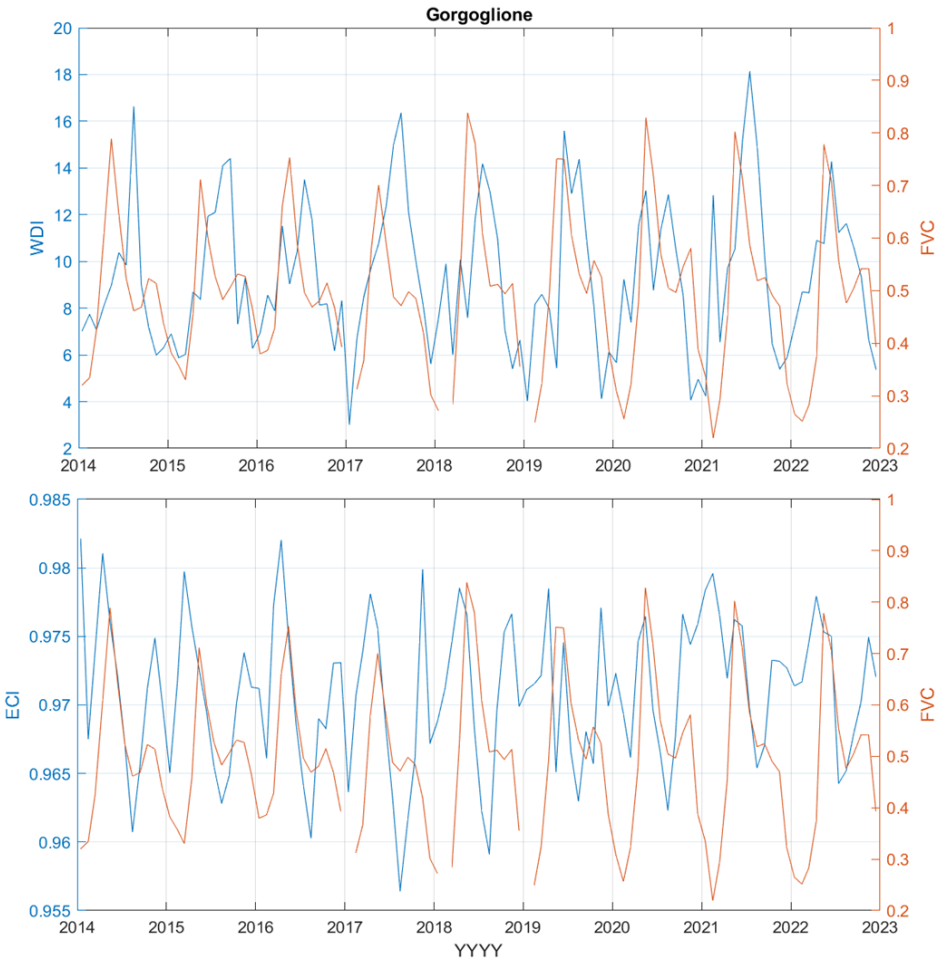

Figure 3.23: Temporal series of FVC versus WDI and ECI for Gorgoglione.

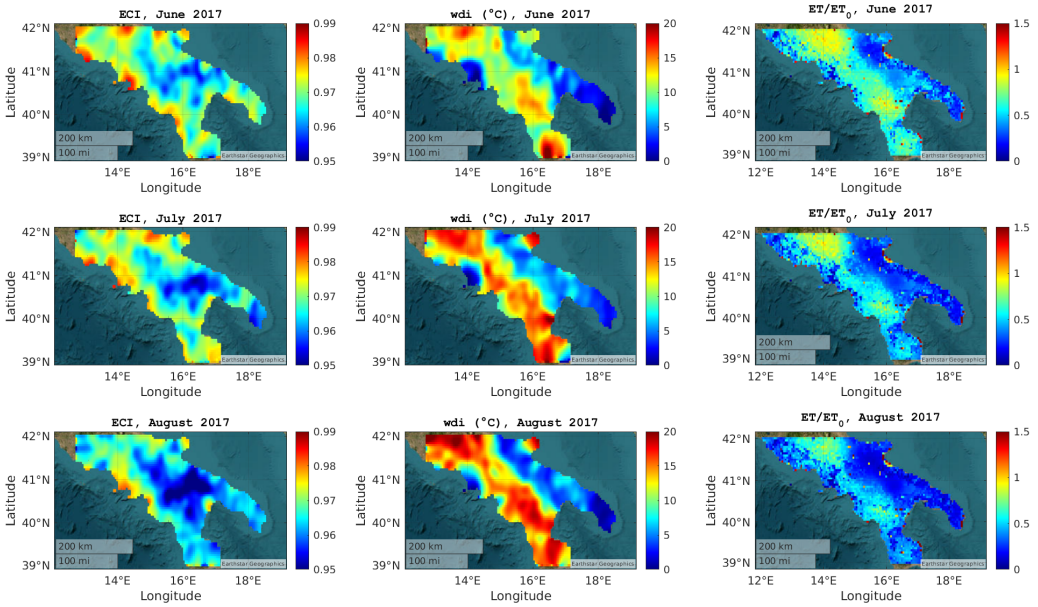

Figure 3.24: Maps of ECI, WDI and ET for June, July and August 2017.

values during summer, displaying an opposite pattern compared to ET. The higher ECI values in winter can be explained by taking into account snow precipitation (Torresani et al. 2022), whereas in summer, it is influenced by the loss of soil moisture, as demonstrated earlier.

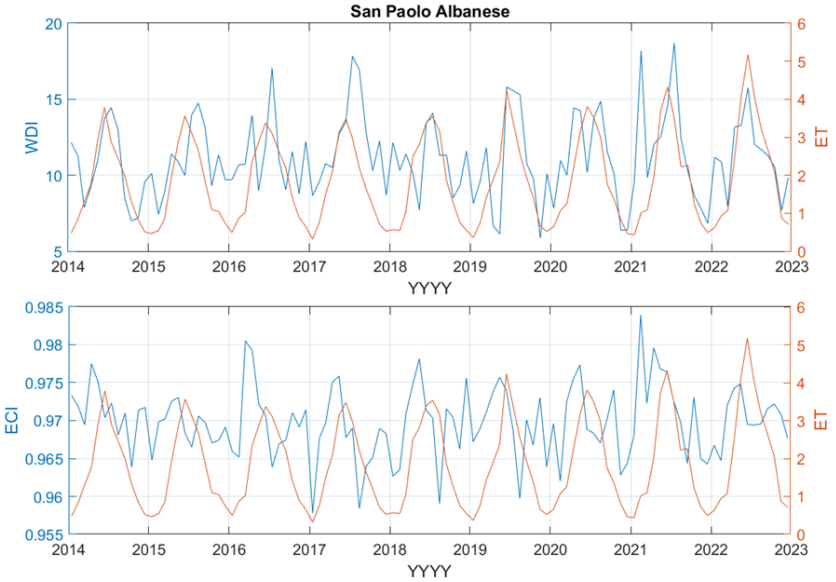

Figure 3.25: Temporal series of ET versus WDI and ECI for San Paolo Albanese

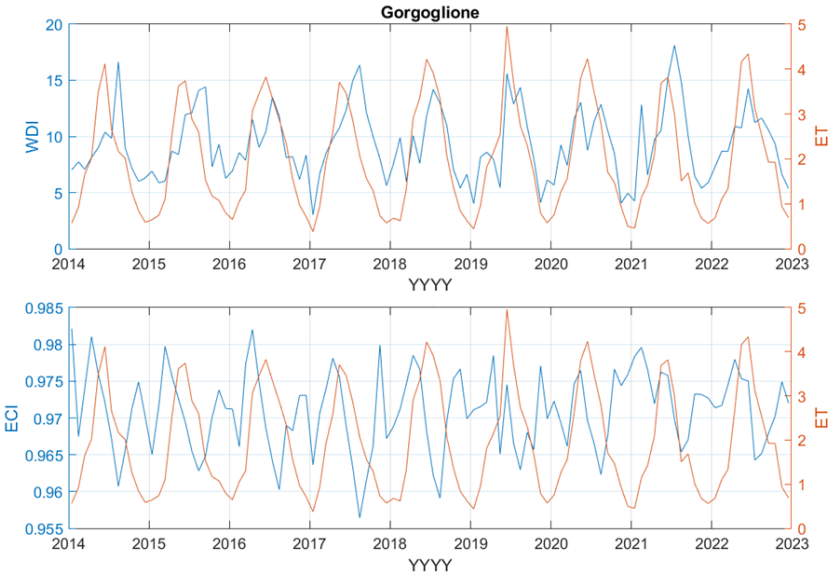

Figure 3.26: Temporal series of ET versus WDI and ECI for Gorgoglione.

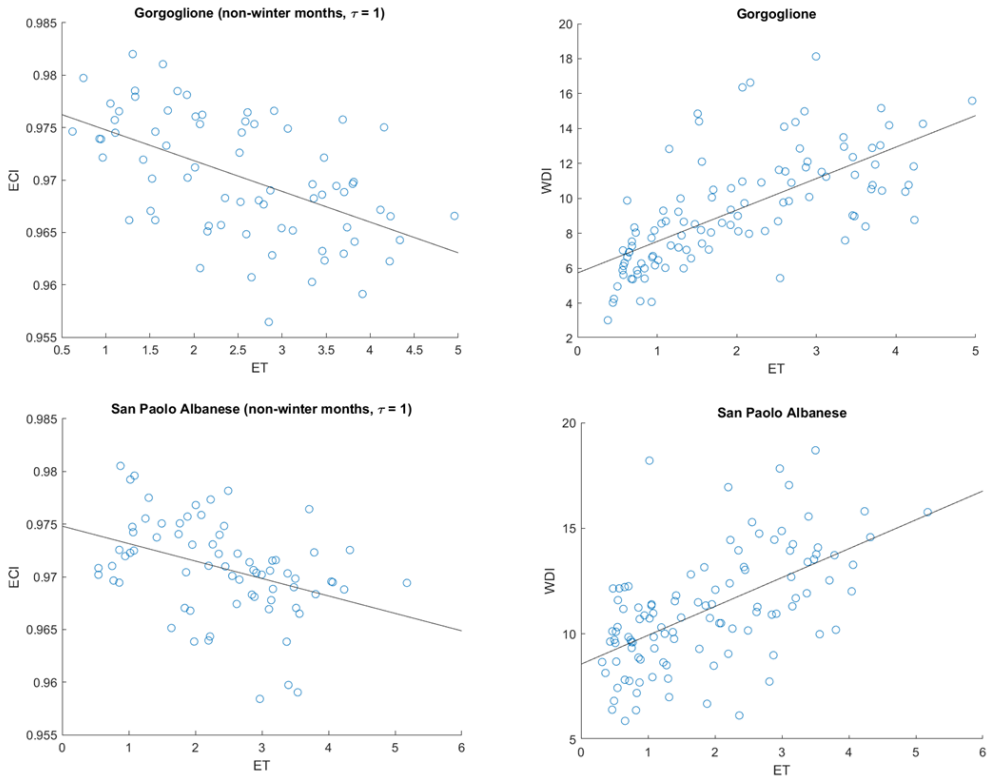

Figure 3.27: Correlation between ET, ECI and WDI for Gorgoglione (upper panel) and San Paolo Albanese (lower panel).

Chapter 4

Validation: the case study of Mount Vesuvius arsons

This chapter demonstrates how the synergy between ECI and WDI can be exploited to identify the criminal origin of a fire event that occurred on Mount Vesuvius in the summer of 2017, thus uncoupling the fire outbreak from the heatwave that affected the Mediterranean area during that same period.

4.1 Description of the case study

In the last 20 years, with the Mediterranean basin suffering high temperatures and drought, especially during summer, wildfires have become an unfortunately common phenomenon. Italy, mainly its southern, widely forested part, has seen the amount of summer fire outbreaks rising almost exponentially, as can be seen in Fig. 4.1, reporting statistics from EFFIS database (San-Miguel-Ayanz et al. 2003). Hot and dry conditions help fires spread faster, burn longer and rage more intensely, sapping moisture from vegetation and turning it into dry fuel that helps fires spread (WMO 2023). However, another dangerous, yet anthropogenic phenomenon often disguises itself underneath the wildfire emergency: arson. It is actually estimated that more than 90% of forestland fire in European Mediterranean countries is caused by human action (Velez 2009; Lovreglio et al. 2010; Canepa and Drogo 2021).

The selected case study is related to a specific set of arsons that occurred on Mount Vesuvius in July 2017. The first, separate blazes started to break out on different points over Mount Vesuvius's slope on June 23rd and rapidly spread until they merged into a massive fire front of two kilometers (see Fig. 4.2) on July 11th (De Luca 2017). The fire was finally dominated and extinguished on July 16th (VesuvioLive 2018). The huge plume of smoke

that generated led some to believe that the Vesuvius was erupting again (it is the only active volcano in mainland Europe). The last time it erupted was back in 1944, but is most famous for the 79 AD eruption that destroyed the ancient Roman city of Pompeii. The smoke from these fires posed the biggest threat and forced several evacuations during that week (De Luca 2017). The wooded slopes of Vesuvius form part of the Vesuvius National Park, which was set up in 1995 to protect the volcano and its surroundings. Much of the woodland was destroyed in what was referred to as an environmental catastrophe: a total amount of 1984 hectares, corresponding to one-third of the entire national park (VesuvioLive 2018). Only two of the culprits were identified and arrested four years later (Di Fiore 2021).

The CORINE Land Cover (Buttner 2014) for 2018 (available at `https://land.copernicus.eu/en/products/corine-land-cover`) highlights the dramatic outcomes of this event (Fig.4.3): the black spot on Mount Vesuvius, classified as *burnt area* by the CORINE algorithm, appears wider when compared to the same location on the 2012 map.

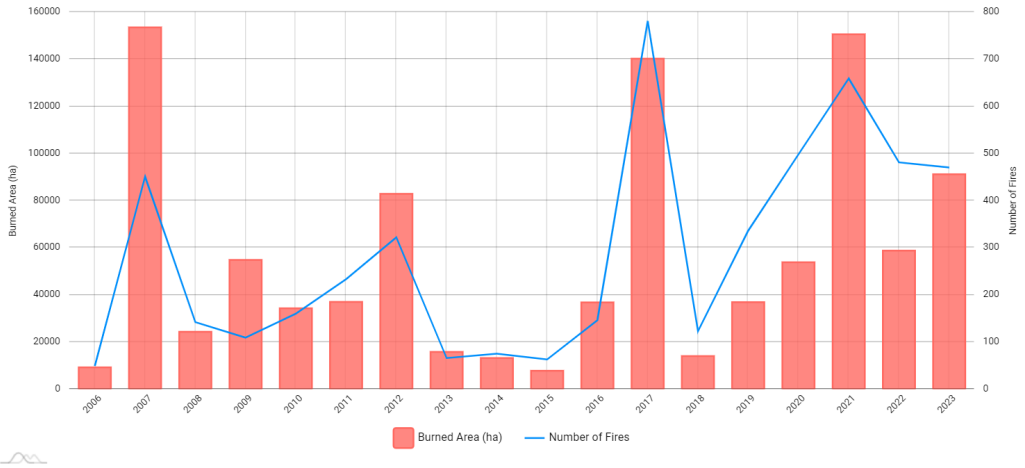

Figure 4.1: Histogram from EFFIS database (San-Miguel-Ayanz et al. 2003) showing the number of fires and the amount of burnt areas in Italy from 2006 to 2023 (`https://effis.jrc.ec.europa.eu/apps/effis.statistics/estimates`).

Figure 4.2: Two pictures of the Vesuvius fire take on July 11th, testifying the event's extreme severity.

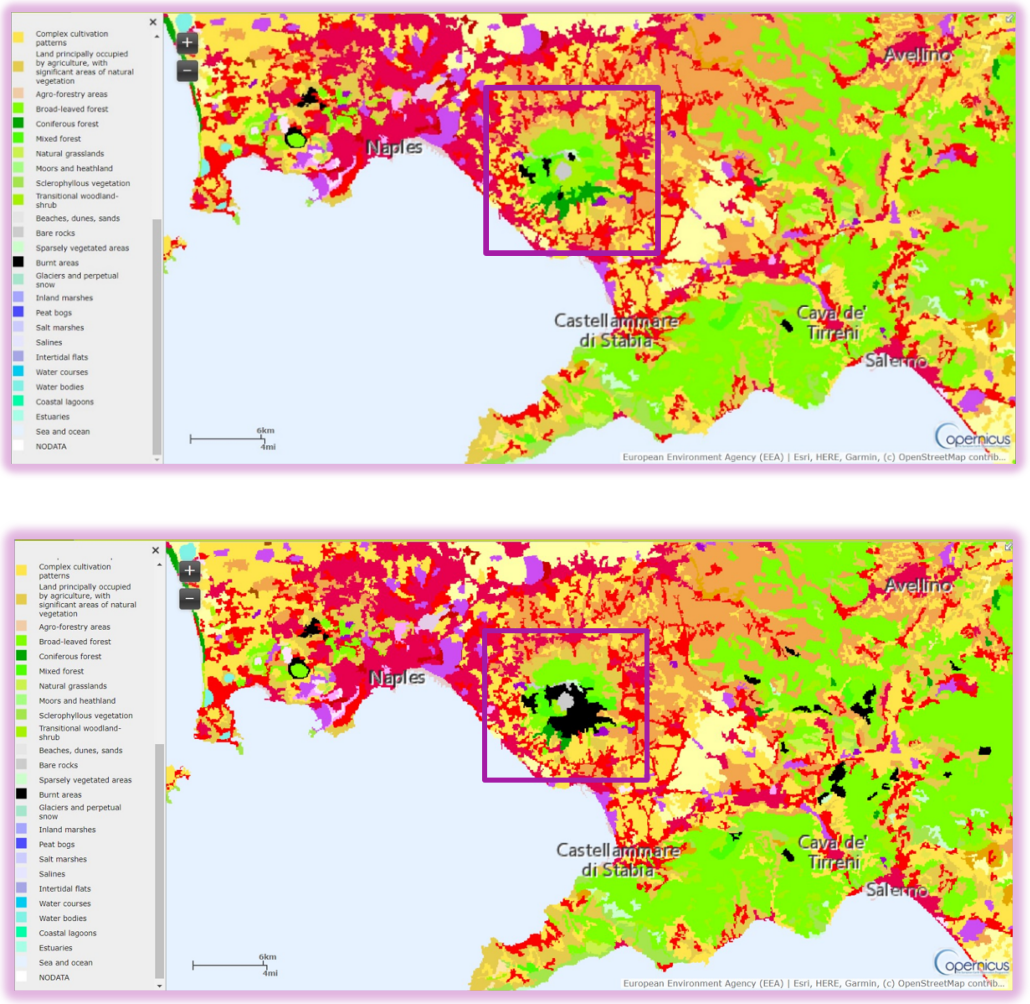

Figure 4.3: CORINE Land Cover (Buttner 2014) maps for 2012 (upper panel) and 2018 (lower panel) over the Gulf of Naples. The violet box encompasses the Mount Vesuvius area. Notice how the portion of the burnt area (in black according to the classification legend) over that same location, as highlighted by the 2018 map, appears wider than in the 2012 version.

4.2 Fire investigation results

To better visualize the entity of the selected fire outbreak, ESA's Sentinel-2 RGB images in different color bands (true and false colors) were produced.

The Sentinel-2 mission operates using a pair of identical satellites: Sentinel-2A and Sentinel-2B. These satellites are equipped with high-resolution multispectral cameras that capture imagery in 13 different wavelength bands, providing valuable insights into land and vegetation.

In Fig. 4.4, various sensor bands are utilized to emphasize the distinct fires occurring around Mount Vesuvius and the resulting smoke spreading across the nearby area:

- Fig. 4.4a uses the typical red, green and blue bands, corresponding to Sentinel-2 channels B4 (665 nm), B3 (560 nm) and B2 (490 nm);
- Fig. 4.4b uses channels B8, B4 and B3, with B8 (842 nm) being in the NIR band. It emphasizes the presence of green vegetation, since it is highly reflective in that spectral interval;
- Fig. 4.4c uses channels B12, B8 and B4, with B12 (2190 nm) included in the SWIR spectral range. This specific band is highly sensitive to fire and burnt soil, while showing lower reflectance values for healthy vegetation.

All three figures display the fire outbreak during its peak of action. In particular, Figs. 4.4b-4.4c are able to pinpoint the severity of the damage (the black area) while the Vesuvius was still burning, whith Fig. 4.4c even highlighting the entity of the fire front.

Another ensemble of colored Sentinel-2 images for three different days of June, July and August 2017 is shown in Fig. 4.5. The three rows represent the situation before, during and after the outbreak respectively: a quick visual comparison among them highlights the intesity of the damage inflicted by the outbreak.

A better way to pinpoint the burnt surface over the target area is estimating its NDVI. In the presence of arid soil, it will show extremely low, positive values. Pre and post-fire NDVI images are shown in Fig. 4.6. Low values are colored in brown, while greenish areas indicate the presence of green vegetation. However, NDVI is not enough to actually identify fire damage.

A more useful index for detecting burnt areas is the Normalized Burn Ratio (NBR, Escuin, Navarro, and Fernández 2008). It is defined as follows:

$$NBR = \frac{\rho_{NIR} - \rho_{SWIR}}{\rho_{NIR} + \rho_{SWIR}} \tag{4.1}$$

This index takes advantage of the properties of the two bands to characterize the presence of burnt soil: high values of NBR are associated with a higher probability of observing a fire-ravaged spot. Pre and post-fire NBR images are shown in Fig. 4.7a and 4.7b. Another index used in the case of wildfires is the ΔNBR (Miller and Thode 2007). It is calculated to assess fire severity:

$$\Delta NBR = NBR_{PRE} - NBR_{POST} \tag{4.2}$$

where NBR_{PRE} and NBR_{POST} represent the NBR value before and after the event respectively. The higher the value, the higher the entity of the damage.

While both NBR and ΔNBR can give insights on the entity and severity of the fire oubreak, they cannot help in identifying the causes behind the phenomenon. In this context, the WDI-ECI synergy could possibly offer interesting information.

Looking at the monthly maps of ECI in Fig. 4.8, it can be observed that the index shows a decreasing trend over the study area (the four black circles) from June to August. The inner areas exhibit even lower ECI values, indicating vegetation distress. Vegetation and the surface have experienced significant long-term stress, with the inner areas being more affected (due to the heat wave) compared to the coastal areas. The decreasing values on Mount Vesuvius are likely attributed to another phenomenon, most probably the July fire. Figure 4.10 displayes the mean emissivity spectrum of the four pixels for the months of June, July and August 2017. The spectral bands used to calculate ECI are also indicated by the colored boxes on the plot.

Maps of WDI for the same period (Fig. 4.9) show that its value on Mount Vesuvius is around 0 °C in June, increasing to 6 °C in August. The moisture loss due to climatic factors does not appear to be predominant, as can instead be observed over the internal part of the area. This further evidence suggests that the July fire was not caused by the heat wave, but was actually intentional, as the competent authorities were then able to prove.

In conclusion, a comparison with other indices and the synergy between the ones developed for this thesis research work highlighted the distressed state of the surface near Mount Vesuvius due to a fire outbreak, with ECI and WDI specifically helping in identyfing the deliberate nature of the fire throughout a remote sensing approach.

(a)

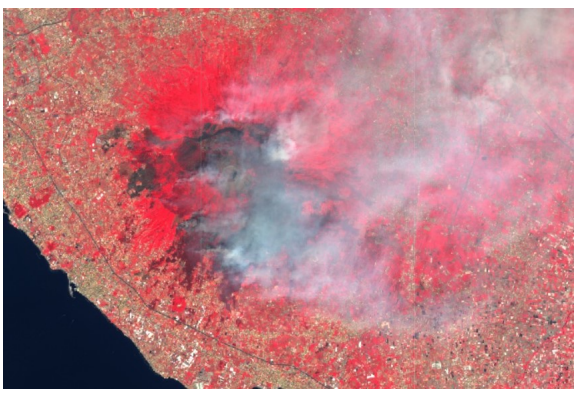

(b)

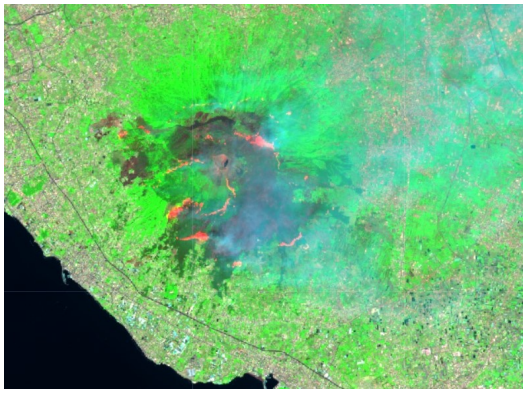

(c)

Figure 4.4: Sentinel-2B RGB images from July 12th 2017, at 9:50 a.m.: Fig. 4.4a uses visible bands B4, B3, B2 to form a true-color picture, while Figs. 4.4b and 4.4c are portrayed in false colors (bands B8, B4, B3 and B12, B8, B4 respectively.)

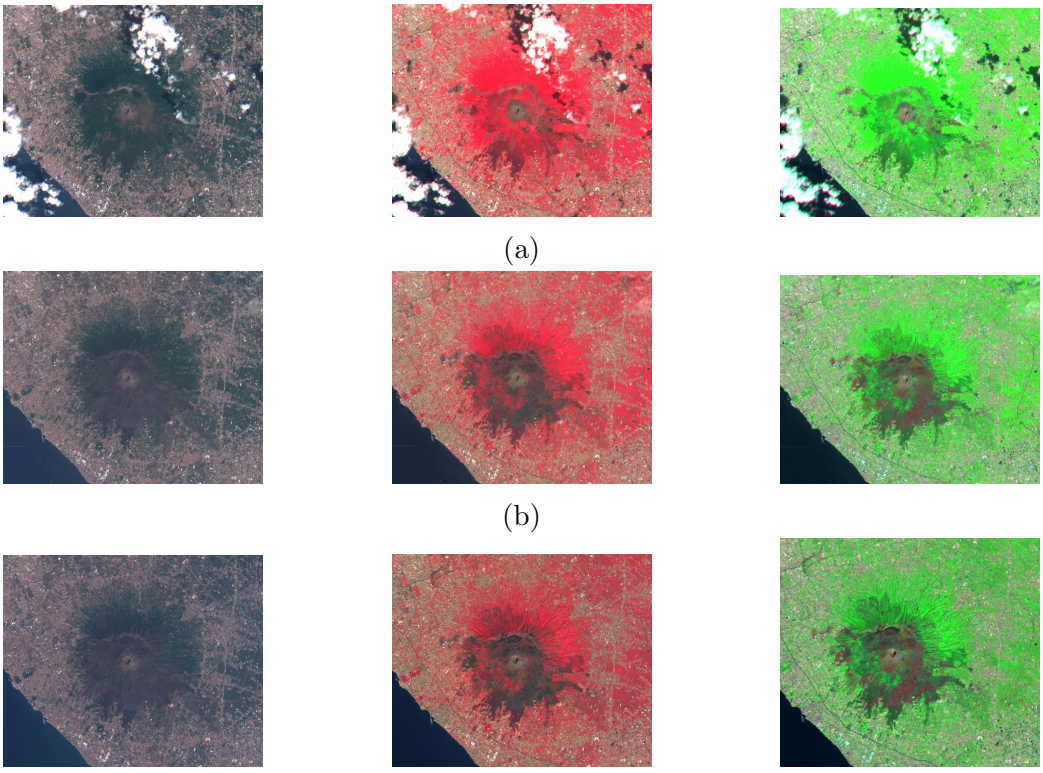

(a)

(b)

(c)

Figure 4.5: Sentinel-2b images for June 27th (Figs. 4.5a), July 22nd (Figs. 4.5b) and August 26th (Figs. 4.5c) over Mount Vesuvius, highlighting the pre and post-fire conditions of the area using different (true and false) color bands.

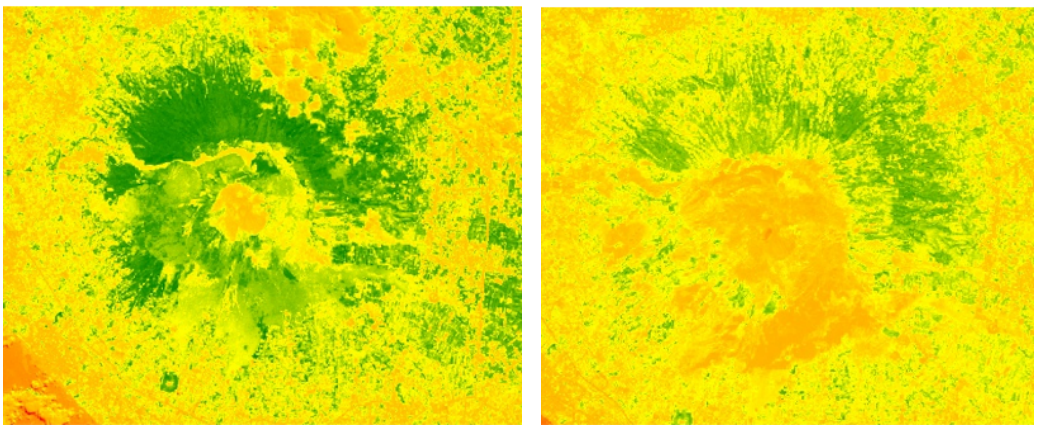

Figure 4.6: Sentinel-2B pre (left) and post-fire (rigth) NDVI images over the burnt area, obtained combining bands B8 (NIR) and B4 (red).

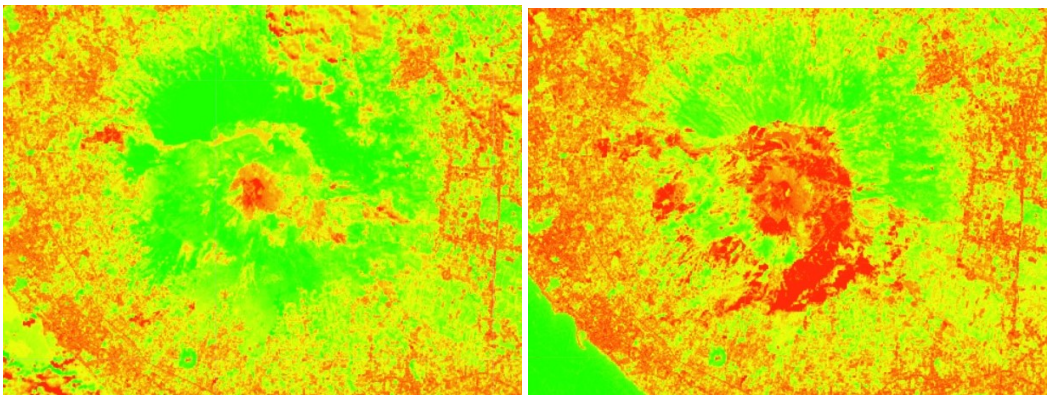

(a) (b)

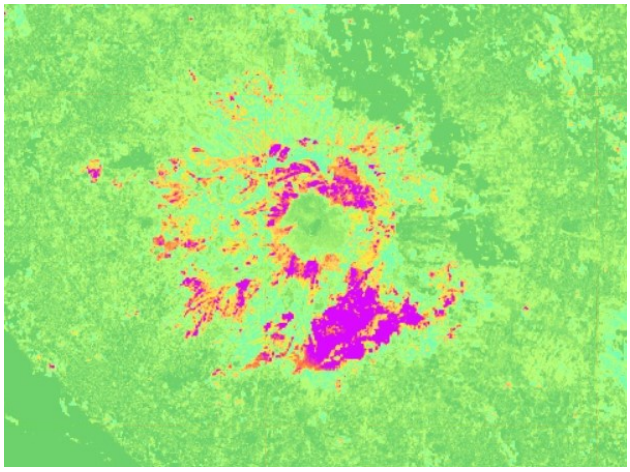

(c)

Figure 4.7: Sentinel-2B pre (Fig. 4.7a) ad post-fire (Fig. 4.7b) NBR images obtained from bands B8 (NIR) and B12 (SWIR), together with their dNBR difference (Fig. 4.7c).

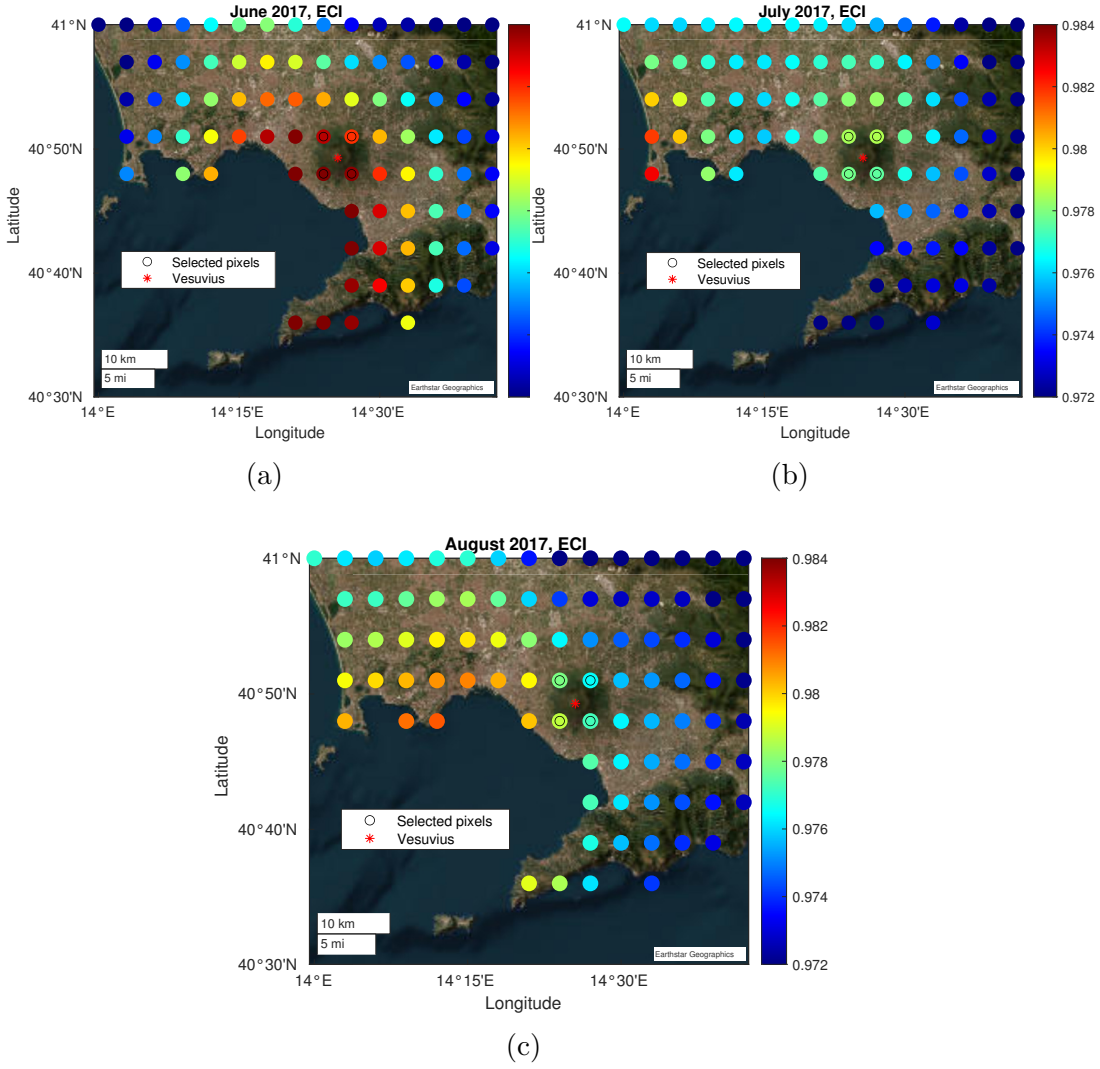

Figure 4.8: Maps of ECI for the Gulf of Naples during summer 2017.

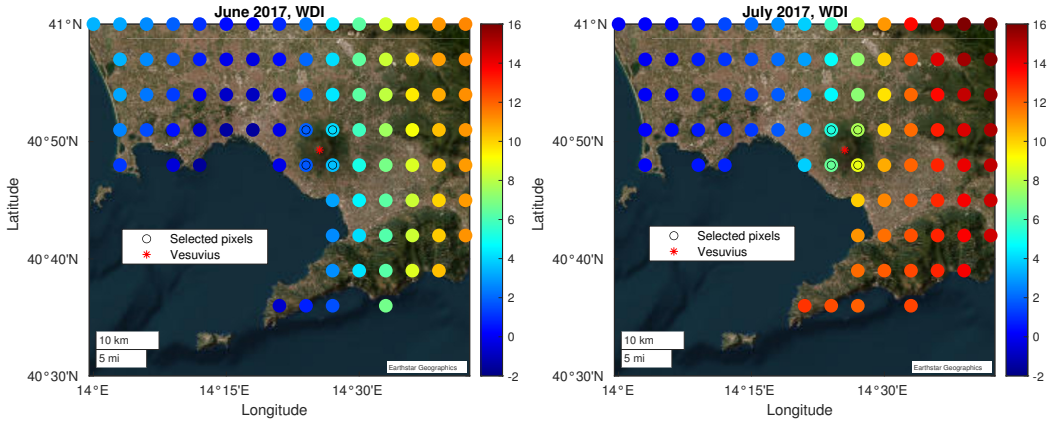

(a) (b)

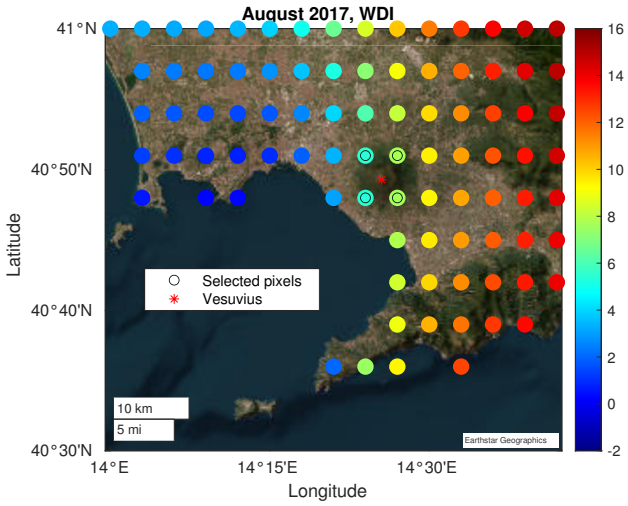

(c)

Figure 4.9: Maps of WDI for the Gulf of Naples during summer 2017.

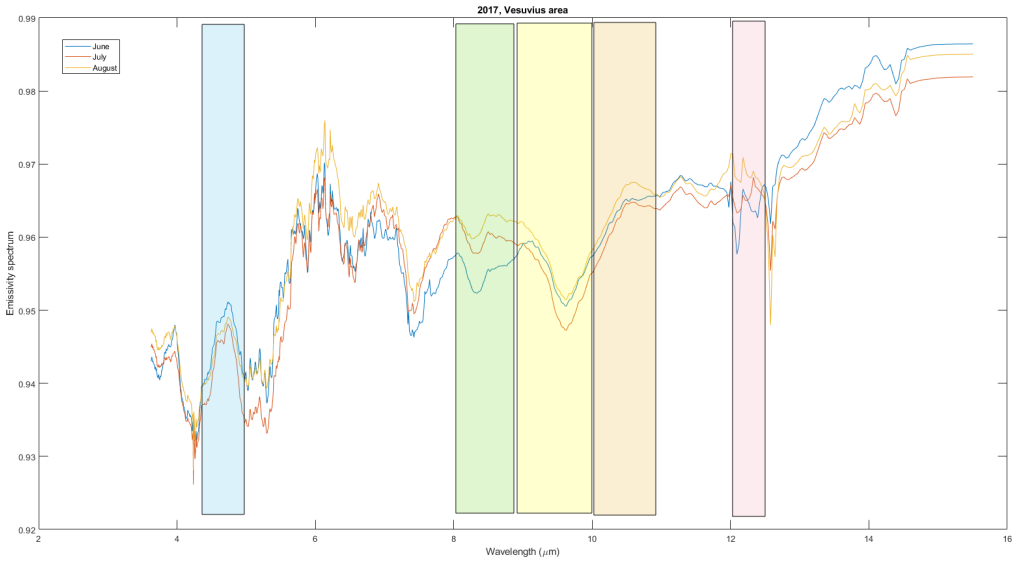

Figure 4.10: Mean emissivity spectrum of the four selected pixels for the three months of June, July and August 2017, together with the indication of the spectral bands used to estimate ECI (colored squares).

Chapter 5

Validation: estimating WDI using the Weather Research and Forecasting Model (WRF)

This chapter is devoted to leveraging the WRF model, a cutting-edge atmospheric modeling and simulation tool that plays a pivotal role in weather research, climate studies, and operational weather forecasting, to obtain high-resolution forecasts of WDI for the target area described in chapter 2. It is shown how the level of detail given by the model enables a better understanding of the index, as well as the possibility to estimate surface water loss with a higher level of detail.

5.1 Description of the WRF model

The WRF system stands as a cornerstone in modern atmospheric science, revolutionizing the way meteorologists understand and predict weather patterns. Developed collaboratively by research institutions and operational forecasting centers worldwide, WRF integrates advanced numerical techniques, high-resolution data assimilation, and sophisticated physics parameterizations to create a powerful tool for weather research and prediction. It employs state-of-the-art numerical methods, such as finite difference and spectral techniques, to discretize the atmospheric equations. These techniques ensure accuracy and efficiency in simulating complex atmospheric processes. Since WRF assimilates vast amounts of observational data, including satellite imagery, radar data, and ground-based measurements, a data assimilation module is provided to synchronize model simulations with real-world observations, enhancing the model's predictive accuracy.

The system incorporates intricate physics parameterizations to simulate sub-grid scale processes, such as cloud formation, precipitation, radiation, and turbulence. These parameterizations capture the nuances of atmospheric interactions, enabling a more detailed representation of weather phenomena. WRF allows researchers to conduct simulations at various spatial and temporal scales, ranging from regional to global domains and from short-term weather events to long-term climate studies. High-resolution modeling is crucial for capturing localized weather phenomena and understanding regional climate variability.

The WRF model has proved to be extremely useful when applied in atmospheric science research. It serves as the backbone of operational weather forecasting systems globally. Its ability to generate high-resolution forecasts aids meteorologists in predicting severe weather events, such as hurricanes, thunderstorms, and heatwaves, with improved accuracy and lead time. Researchers also utilize WRF to investigate climate variability and change at regional scales. By simulating historical climate patterns and projecting future scenarios, scientists gain insights into the impacts of climate change on specific regions, informing adaptation and mitigation strategies. WRF plays a crucial role in air quality modeling by simulating atmospheric dispersion of pollutants. Researchers use the system to assess the impact of emissions from industries, transportation, and natural sources on air quality, facilitating policy decisions to mitigate pollution. The model enables scientists to study extreme weather events, such as droughts, floods, and wildfires, in unprecedented detail. By simulating the atmospheric conditions leading to these events, researchers enhance our understanding of their causes and dynamics, aiding in disaster preparedness and response efforts.

WRF represents a paradigm shift in atmospheric science research and operational forecasting. Its sophisticated modeling techniques and diverse applications make it an indispensable tool for understanding the complexities of the Earth's atmosphere. As meteorologists and climate scientists continue to grapple with the challenges posed by a changing climate, WRF remains at the forefront, enabling innovative research and enhancing our ability to predict and respond to weather-related phenomena with unprecedented precision.

5.1.1 Physics Parameterizations

The accurate representation of atmospheric processes relies heavily on sophisticated physics parameterizations. These parameterizations encapsulate complex physical phenomena that occur at scales smaller than the model grid, allowing researchers to capture the intricacies of the Earth's atmosphere:

- Microphysics - Microphysics parameterizations in WRF deal with the processes related to cloud and precipitation formation. This includes the representation of cloud droplet formation, collision and coalescence, and ice nucleation. WRF incorporates advanced microphysical schemes that consider different hydrometeor types, such as rain, snow, ice, and graupel. These schemes account for various processes like autoconversion, accretion, and evaporation, ensuring a realistic simulation of cloud and precipitation patterns.

- Radiation - WRF includes multiple radiation schemes to model the transfer of solar and thermal radiation within the atmosphere. These schemes calculate the interactions between radiation and atmospheric constituents, clouds, and the Earth's surface. WRF's radiation parameterizations are vital for simulating diurnal temperature variations, cloud radiative effects, and energy exchanges between the atmosphere and the Earth's surface.

- Boundary Layer Physics - Boundary layer parameterizations in WRF simulate the processes occurring near the Earth's surface, where the effects of the underlying terrain significantly influence atmospheric behavior. These parameterizations account for turbulence, mixing, and vertical fluxes of heat, moisture, and momentum. They are essential for capturing phenomena like temperature inversions, atmospheric stability, and the development of low-level jets, which have significant impacts on local weather patterns.

- Land Surface Processes - WRF's land surface models simulate interactions between the atmosphere, soil moisture, and heat fluxes. These parameterizations consider the land surface characteristics such as vegetation cover, soil type, and land use. By incorporating these details, WRF can simulate feedback mechanisms between the land surface and the atmosphere, leading to realistic representations of phenomena like land-atmosphere coupling, heatwaves, and regional climate variations.

- Convection - Convection parameterizations in WRF are crucial for simulating thunderstorms and other convective weather events. These schemes model the vertical transport of heat, moisture, and momentum due to updrafts and downdrafts within convective clouds. WRF offers multiple convection schemes, allowing researchers to choose the one best suited for specific weather conditions and spatial scales. This flexibility ensures an accurate representation of convective processes in a wide range of atmospheric situations.

- Planetary Boundary Layer (PBL) schemes - WRF includes various PBL parameterizations that characterize the turbulent layer of the atmosphere near the Earth's surface. These schemes account for the vertical mixing of momentum, heat, and moisture within the PBL. Different PBL schemes are suitable for different atmospheric stability conditions, ensuring that the model captures the variations in boundary layer structure under diverse weather conditions.

- Gravity Wave Drag - Gravity waves, generated by processes such as winds flowing over mountains or convective activity, play a significant role in the atmosphere's dynamics. WRF incorporates parameterizations for gravity wave drag, which represents the effects of these waves on the larger-scale atmospheric flow. By including gravity wave drag parameterizations, WRF can simulate the influence of these waves on weather patterns and improve the accuracy of the model's predictions, especially at high altitudes.

- Cloud parameterizations - WRf includes sophisticated cloud parameterizations that model cloud microphysics, subgrid-scale cloud cover, cloud radiative effects, and precipitation processes. These parameterizations allow WRF to accurately simulate various cloud types, their interactions with radiation, and the formation of precipitation, enhancing the system's ability to predict weather patterns and understand cloud-related phenomena in the atmosphere.

Moreover, WRF supports multiple vertical coordinate systems, including terrain-following, pressure, and hybrid sigma-pressure coordinates. Each of these systems has its advantages, allowing researchers to choose the most appropriate representation for the specific atmospheric conditions they aim to simulate. Terrain-following coordinates are particularly useful for capturing the effects of complex topography on weather patterns, ensuring a more accurate portrayal of localized phenomena such as mountain-induced precipitation.

5.2 Configuration used

Two WRF simulations have been run, using two different sets of global forecast data:

- GFS 0.25° operational forecasts (`https://rda.ucar.edu/datasets/ds084.1/`).

- ECMWF operational analysis at 0.125° (`https://www.ecmwf.int/en/forecasts/dataset/operational-archive`).

Figs. 5.1 and 5.2 illustrate the domain definitions and corresponding height maps for both simulation runs. In the case of the GFS simulation, a dual nested domain setup was employed. The outer domain (D01) spans most of central and southern Italy with a resolution of 20 km, while the inner domain (D02) covers only the southern part of the Italian peninsula at a higher resolution of 4 km.

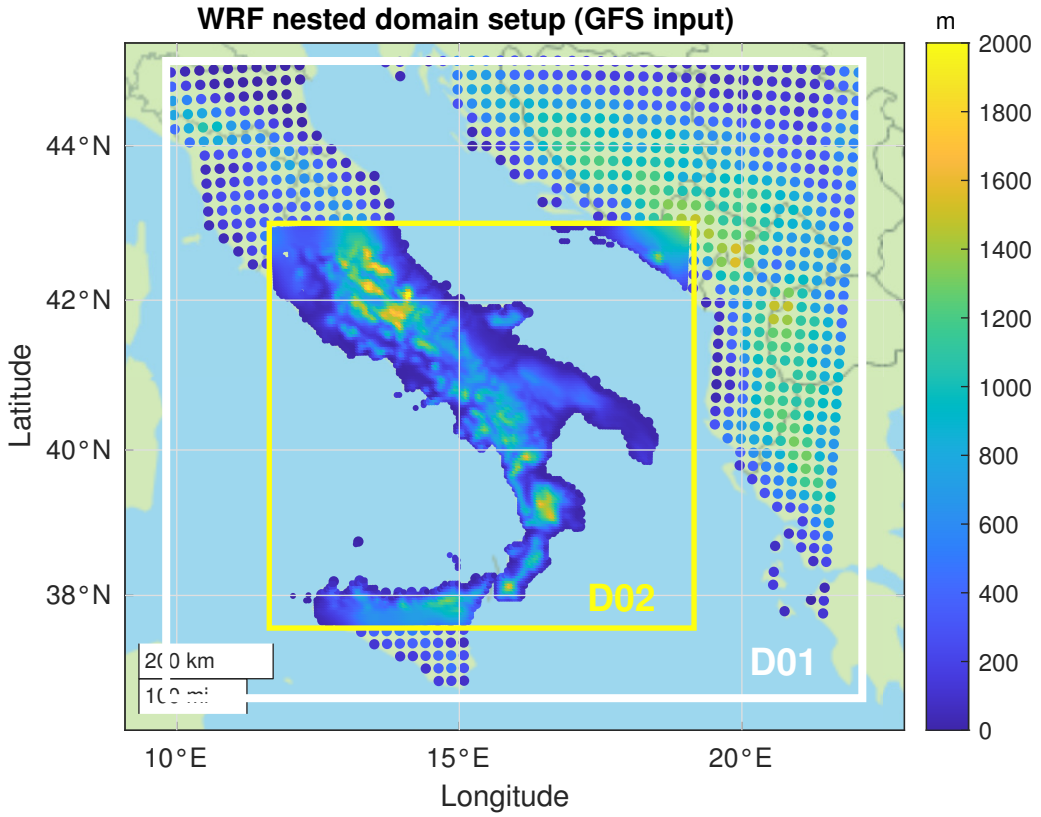

Figure 5.1: WRF model nest configuration (GFS input). The inner domain (D02) corresponds to the actual study area. The horizontal resolutions of the model domains (D01 e D02) are 20 and 4 km respectively.

In contrast, the ECMWF run features a similar dual nested domain configuration, but both domains are exclusively focused on southern Italy. D01 has a resolution of 6 km, while the inner domain, D02, is finely resolved at 1 km. This adjustment in domain definition was imperative due to the substantial discrepancy between the resolutions of the GFS and ECMWF datasets, with the former being twice as coarse as the latter.

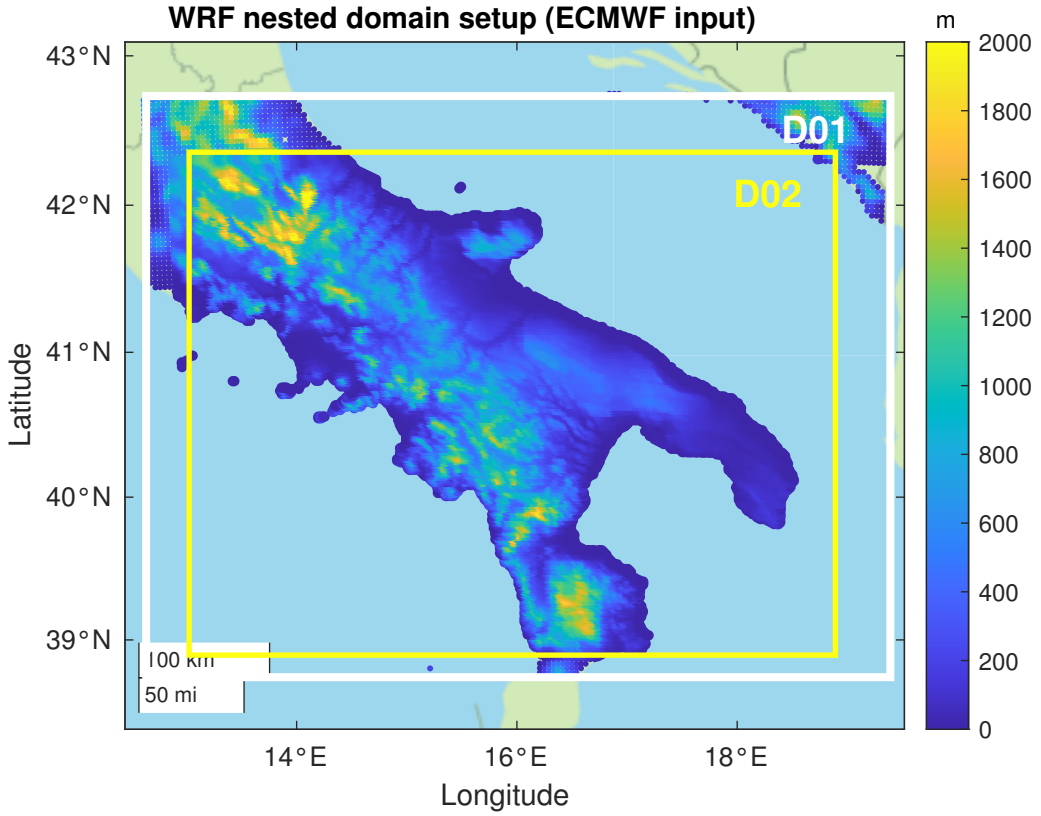

Figure 5.2: WRF model nest configuration (ECMWF input). The inner domain (D02) corresponds to the actual study area. The horizontal resolutions of the model domains (D01 e D02) are 6 and 1 km respectively.

The simulation period spans the entirety of July 2017, and hourly forecasts were stored for both runs, thus accounting for the diurnal variation of WDI, both at a wider (Southern Italy) and local (the woodlands of San Paolo Albanese and Gorgoglione) scale .

Figs. 5.3 and 5.4 showcase an exemplar representation of the vertical layering for both simulation setups, employing the hybrid sigma-pressure vertical coordinate system (Beck et al. 2020; Skamarock et al. 2019). This system offers distinct advantages; it maintains a terrain-following coordinate near the surface, enhancing accuracy in pressure gradient calculations by relying on pressure levels at higher altitudes in the atmosphere (Beck et al. 2020). Notably, this approach prevents the propagation of terrain-induced noise from initial levels to upper atmospheric sections (see Fig. 5.5): the precision of the simulations is therefore enhanced, ensuring a more faithful representation of atmospheric phenomena.

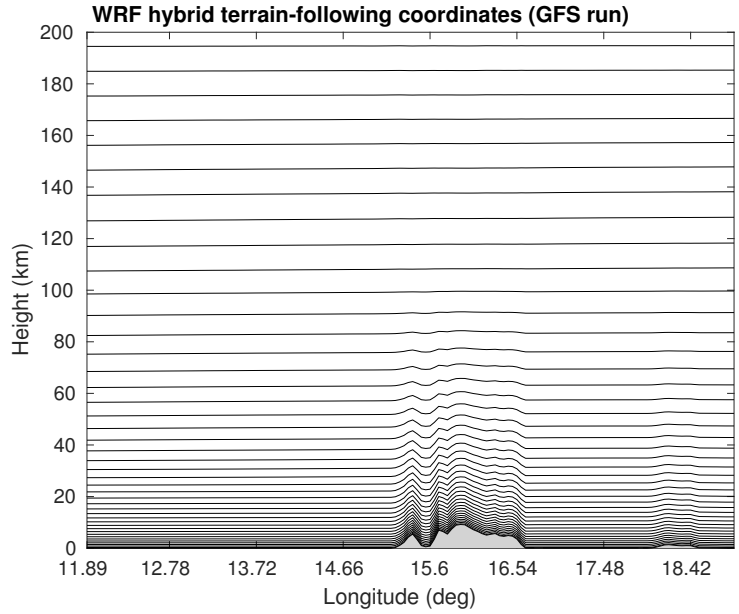

Figure 5.3: WRF vertical hybrid terrain-following coordinate layers for the GFS-initialized run.

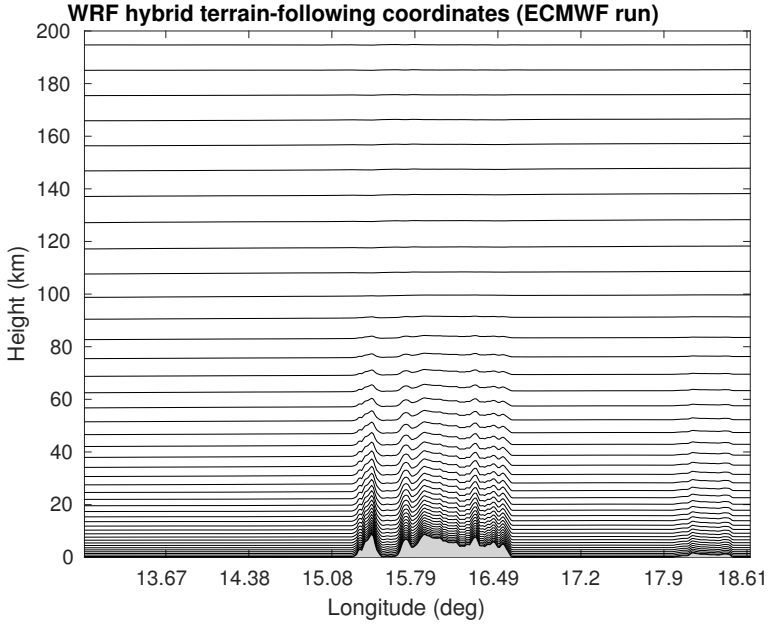

Figure 5.4: WRF vertical hybrid terrain-following coordinate layers for the ECMWF-initialized run.

The physics options used are summarized in Tab. 5.1. The way they interact is represented by the schematic diagram in Fig. 5.6.

Table 5.1: Physics options selected for both WRF runs.

Physics	**Scheme**	**Index**
Microphysics	Purdue Lin (S.-H. Chen and Sun 2002)	2
Shortwave Radiation	RRTM (Mlawer et al. 1997)	1
Longwave Radiation	Dudhia (Jimy Dudhia 1989)	1
Surface Layer	Eta Similarity (Janić 2001)	2
Land Surface Model	UNLS (Mukul Tewari et al. 2004)	2
Planetary Boundary Layer	Mellor–Yamada–Janjic (Janjić 1994)	2
Cumulus parameterization	Kain–Fritsch (Kain 2004)	1

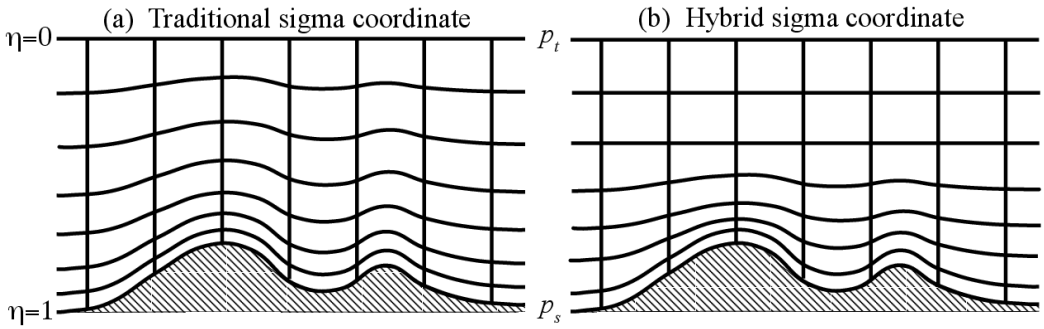

Figure 5.5: A qualitative graphic example of the difference between the traditional sigma and hybrid sigma coordinate system used in WRF version 4 (from Skamarock et al. 2019).

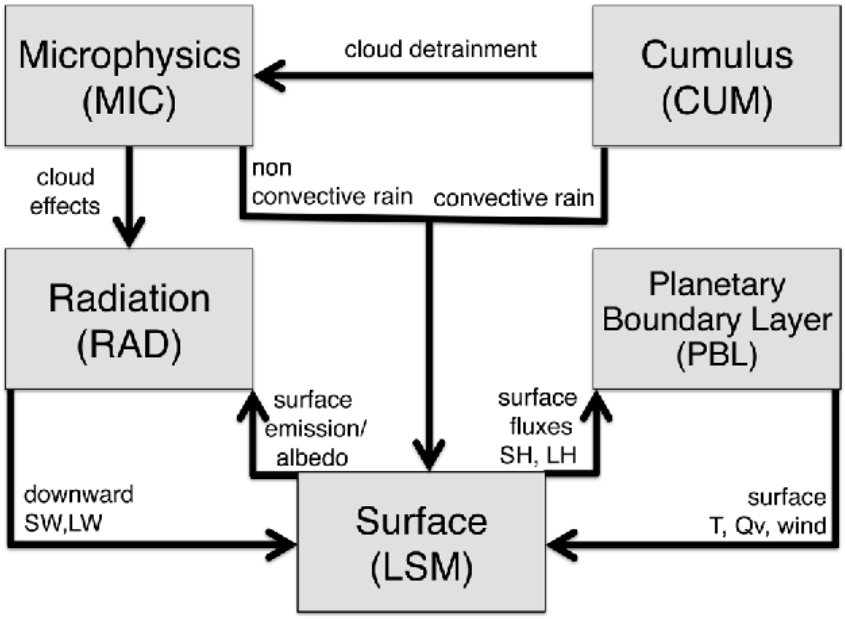

Figure 5.6: Interactions between the physics options in WRF (from Skamarock et al. 2019)

5.3 Results

The variables used for the calculation of WDI were the surface skin temperature (indicated simply as surface temperature in text from here on) and the 2-meter dew point temperature, estimated as already explained in Sec. 2.4.2.

Figs. 5.7 and 5.8 provide two examples of vertical-cross sections of pressure for both simulations. Notably, the atmosphere's layering appears significantly smoother when utilizing the ECMWF analysis as input, indicating a more refined representation of atmospheric conditions.

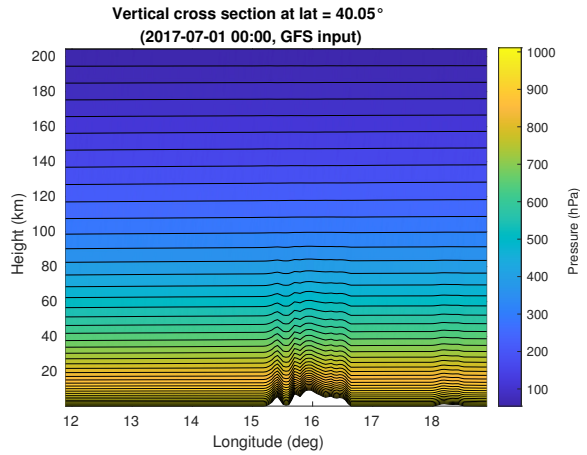

Figure 5.7: Vertical cross-section of pressure at a latitude of 45.05 ° for July 1st 2017 at midnight (GFS run).

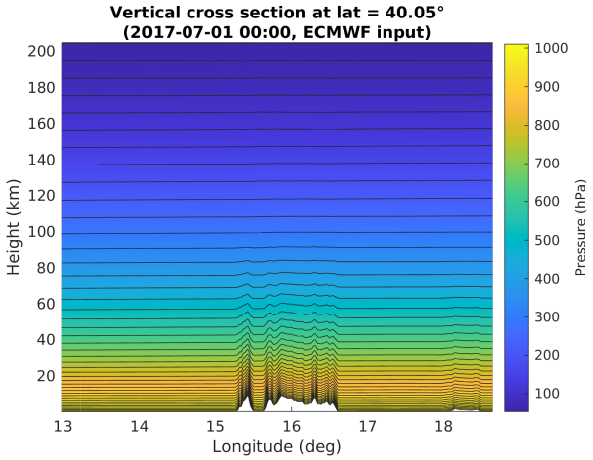

Figure 5.8: Vertical cross-section of pressure at a latitude of 45.05 ° for July 1st 2017 at midnight (ECMWF run).

By way of example, visual representations of 2-meter air temperature overlaid with sea-level pressure are available for four distinct days at 12 PM, as depicted in Figs. 5.9 and 5.10. Notably, the WRF-ECMWF output provides a more detailed depiction of pressure patterns, emphasizing the precision of this simulation. Interestingly, the 2-meter air temperature exhibits a consistent trend across both simulations, highlighting the convergence of results in this aspect.

Monthly maps of surface temperature, dew-point temperature at 2 meters, and WDI are depicted in Figs. 5.11- 5.16. These visualizations reveal intriguing patterns. Surface temperatures exhibit higher values over the Apulia region in both runs, with IASI data indicating temperatures approximately lower than 5 °C in the same area with respect to the simulations. The behavior of dew-point temperature remains consistent across all three cases.

These observations are directly reflected in the resulting WDI maps. The WDI values derived from the GFS-based simulation surpass 20 °C in a significant portion of the area, contrasting with the ECMWF run, which aligns more closely with the behavior observed in the IASI WDI output. However, both runs manage to improve the resolution of the prediction and actually correct the behaviour of the global forecast, spreading the increasing WDI trend over the central part of southern Italy: this highlights the effects of the intense heatwave of summer 2017, which interested the Mediterranean area and Souther Italy in particular.

Figure 5.17 displays the variation of WRF-ECMWF WDI for four different days of July 2017 (7th, 14th, 21st and 28th): the index seems to be decaying during the period over the Appenines, while showing higher values over the Apulia region by the end of the month.

On an even finer temporal scale, Fig. 5.18 shows maps of WRF-ECMWF WDI for the four different canonical hours (00:00, 06:00, 12:00, 18:00) for July 14th 2017: the index, starting from lower values at 00:00, rises during the day, reaching a peak value of over 25 °C at 12:00 on the internal part of the region; subsequently, it decreases till reaching a minimum value of approx. 5 °C at 18:00.

Zooming in on a single-pixel, local scale, Figure 5.19 presents intriguing results. WRF-GFS WDI demonstrates a noticeable upward trend during July 2017 in both San Paolo Albanese and Gorgoglione, peaking at around 26 and 15 °C respectively at the end of the month. In contrast, WDI predicted by WRF-ECMWF indicates a more moderate increase, oscillating around 12 °C in Gorgoglione.

This disparity in WDI trends is directly linked to the surface and dew-point temperature values predicted by the models. A closer examination of Figs. 5.20-5.21 reveals a consistent pattern. Surface temperatures in both

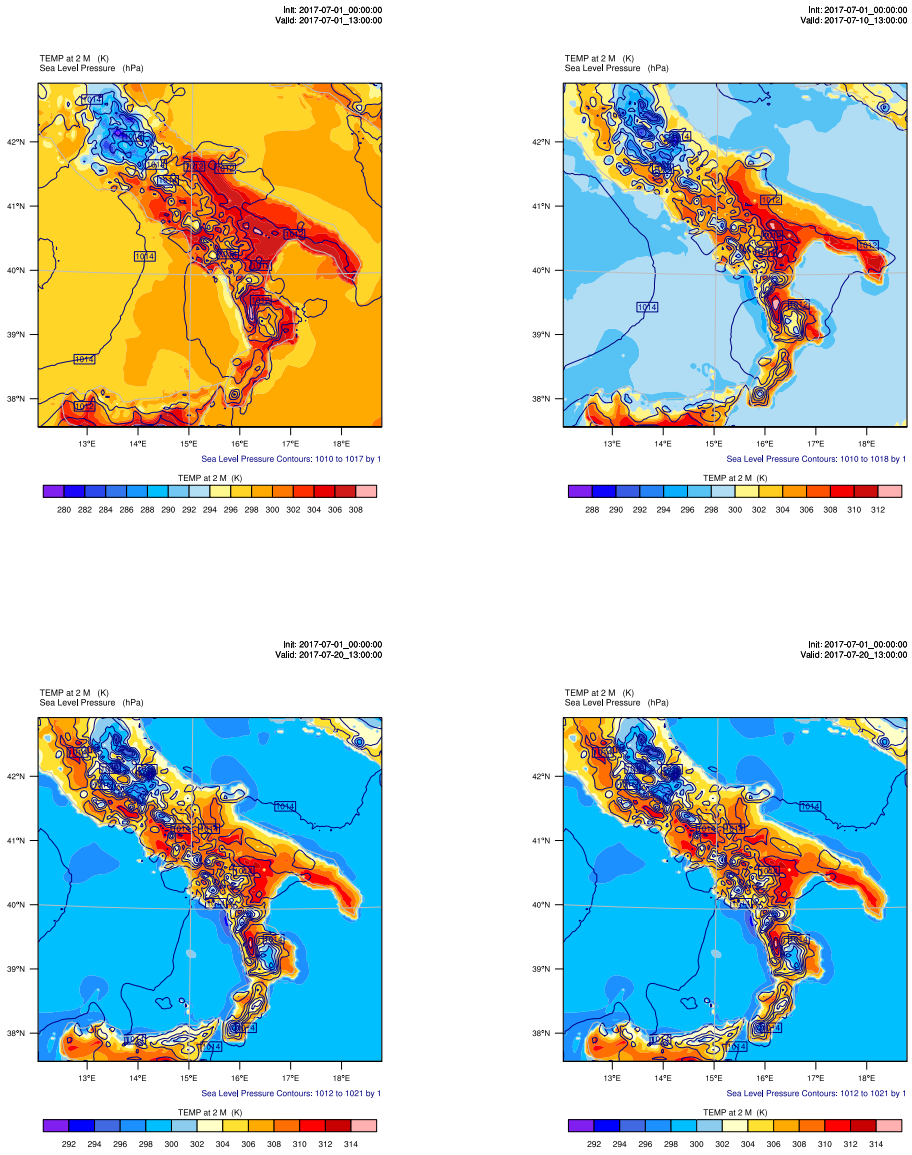

Figure 5.9: WRF-GFS 2-meter air temperature (K) and overlayed sea level pressure for July 1st, 10th, 20th and 30th.

areas exhibit a trend mirroring that of WDI, with the anomalous minimum peaks of 22 and 20 °C respectively on July 27th likely stemming from discrepancies in the original global ECMWF analysis for that day. Dew-point temperatures decrease throughout the entire month in both simulations and

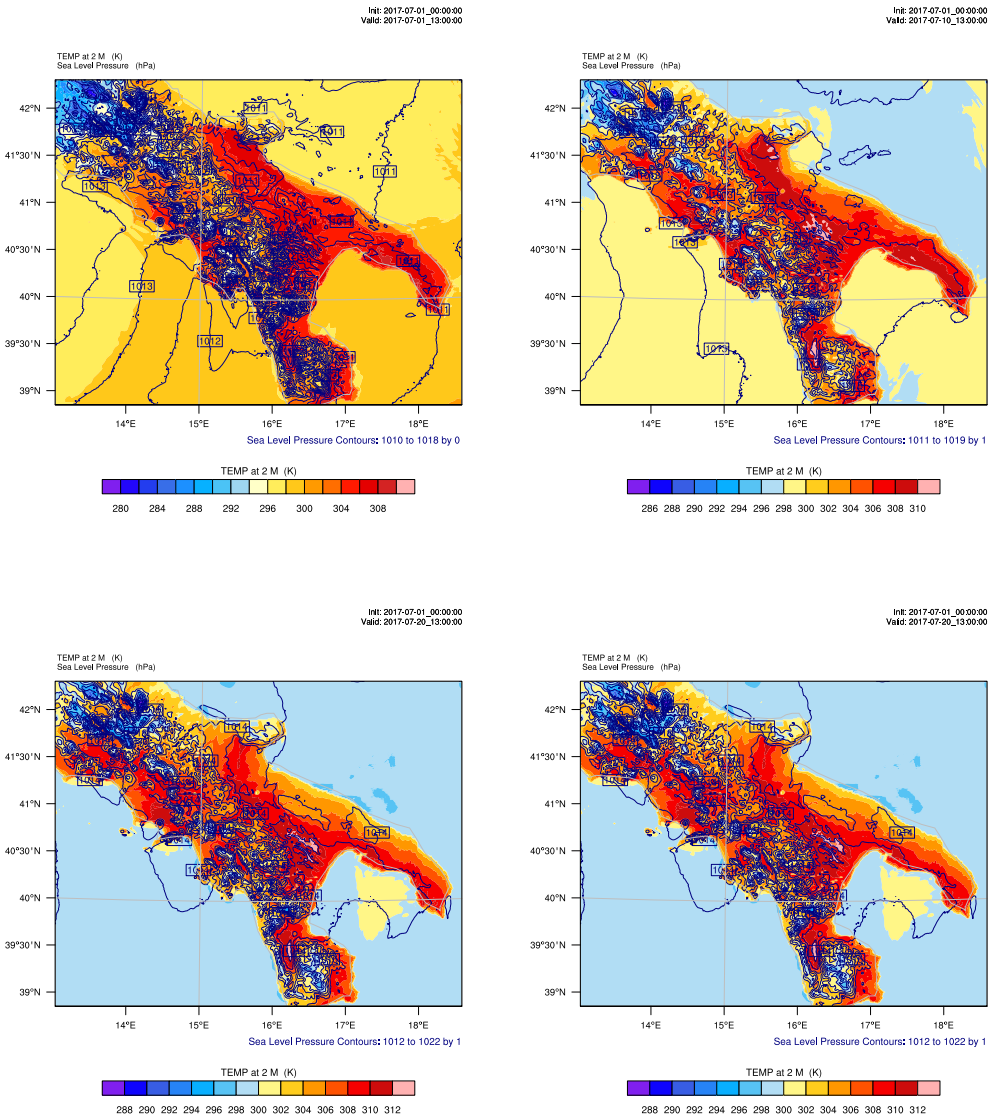

Figure 5.10: WRF-ECMWF surface temperature (K) and overlayed sea level pressure for July 1st, 10th, 20th and 30th.

areas (once again the WRF-ECMWF run exibiting a minimum peak on July 27th, for the same reasons previously discussed).

Furthermore, it's noteworthy that the dew-point temperature remains nearly constant over Gorgoglione, emphasizing the stability of this parameter in the region. Additionally, the WRF-GFS run consistently predicts

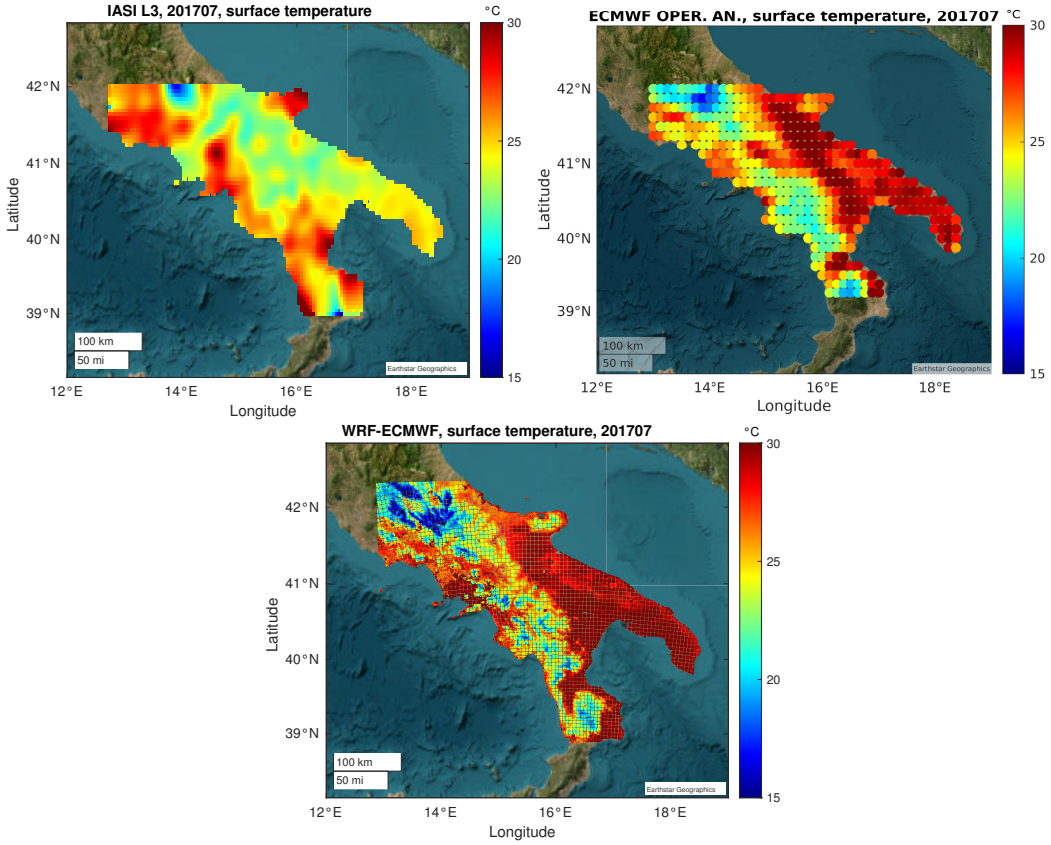

Figure 5.11: Maps of surface temperature for July 2017. Upper panel: IASI L3 (left, 5 km resolution) and ECMWF operational analysis (right, 12.5 km resolution). Lower panel: WRF-forecasted output (1.2 km resolution) using ECMWF operational analysis data as boundary and initial conditions.

values lower than its WRF-ECMWF counterpart, indicating nuanced differences in the models' outputs. These intricate details shed light on the complex interplay of atmospheric variables and the simulation models' predictive capabilities.

Overall, the results of both simulations suggest a convergence in the trend of WDI during July 2017, indicating an interesting level of agreement with the IASI WDI estimation. This further validates the methodology used and underscores the potential of WDI as a useful index for surface and atmosphere monitoring, not only in the context of remote sensing alone but also in expanding knowledge and insights in meteorology.

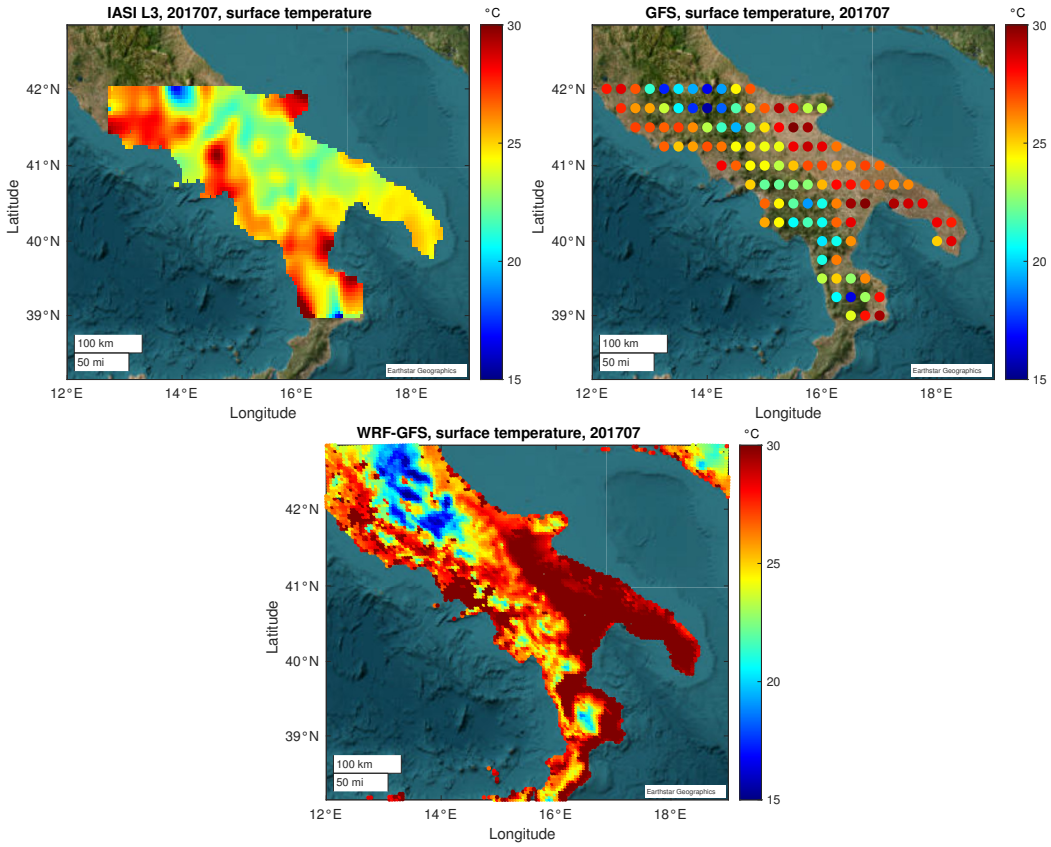

Figure 5.12: Maps of surface temperature for July 2017. Upper panel: IASI L3 (left, 5 km resolution) and GFS forecasts (right, 25 km resolution). Lower panel: WRF-forecasted output (4 km resolution) using GFS forecast data as boundary and initial conditions.

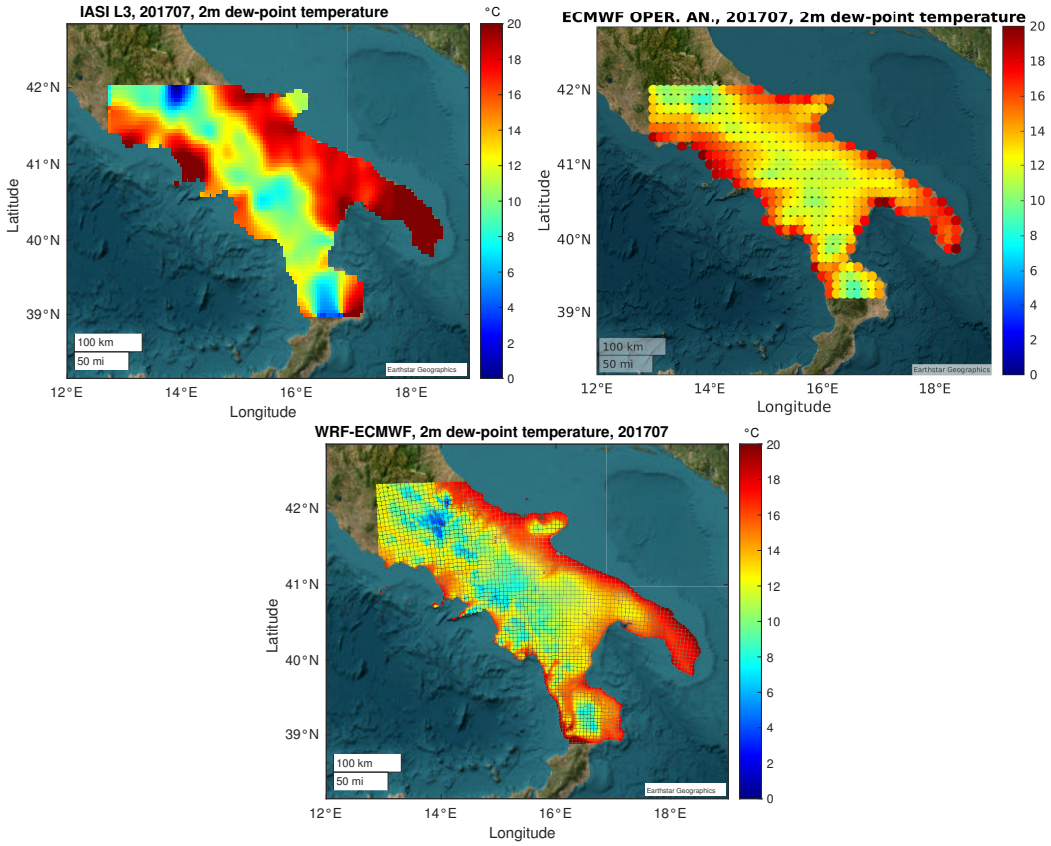

Figure 5.13: Maps of 2-meter dew-point temperature for July 2017. Upper panel: IASI L3 (left, 5 km resolution) and ECMWF operational analysis (right, 12.5 km resolution). Lower panel: WRF-forecasted output (1.2 km resolution) using ECMWF operational analysis data as boundary and initial conditions.

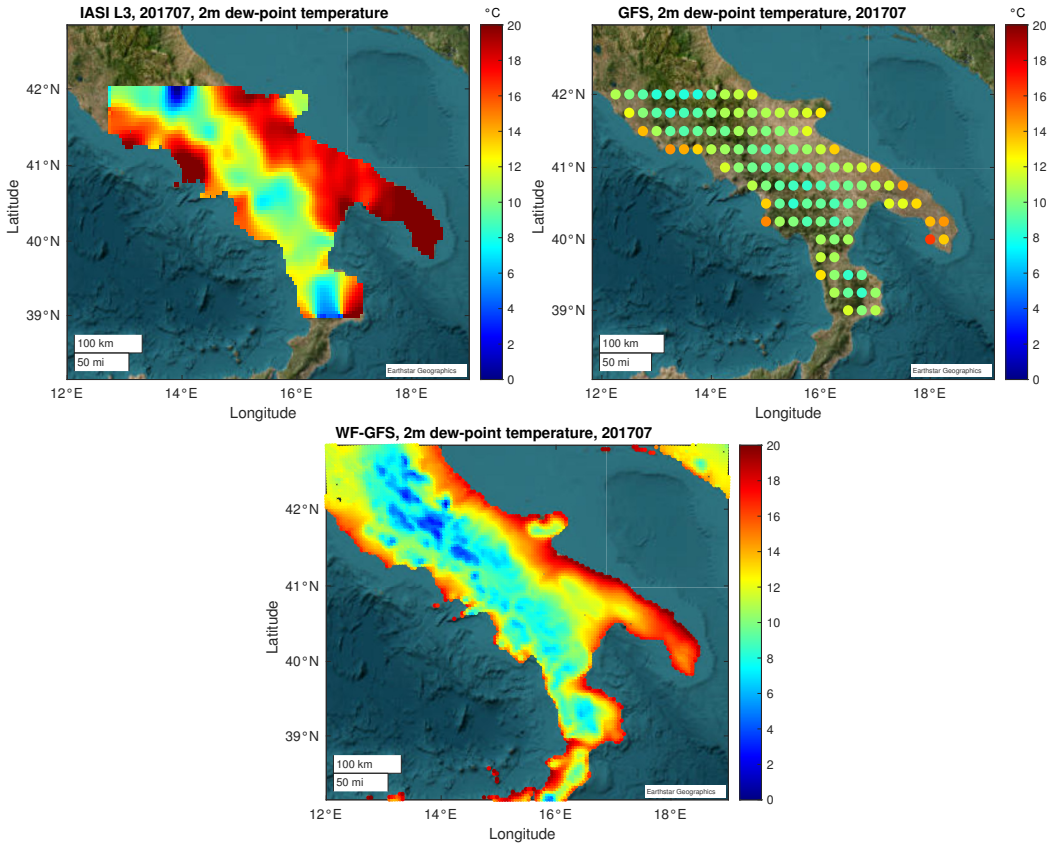

Figure 5.14: Maps of 2-meter dew-point temperature for July 2017. Upper panel: IASI L3 (left, 5 km resolution) and GFS forecasts (right, 25 km resolution). Lower panel: WRF-forecasted output (4 km resolution) using GFS forecast data as boundary and initial conditions.

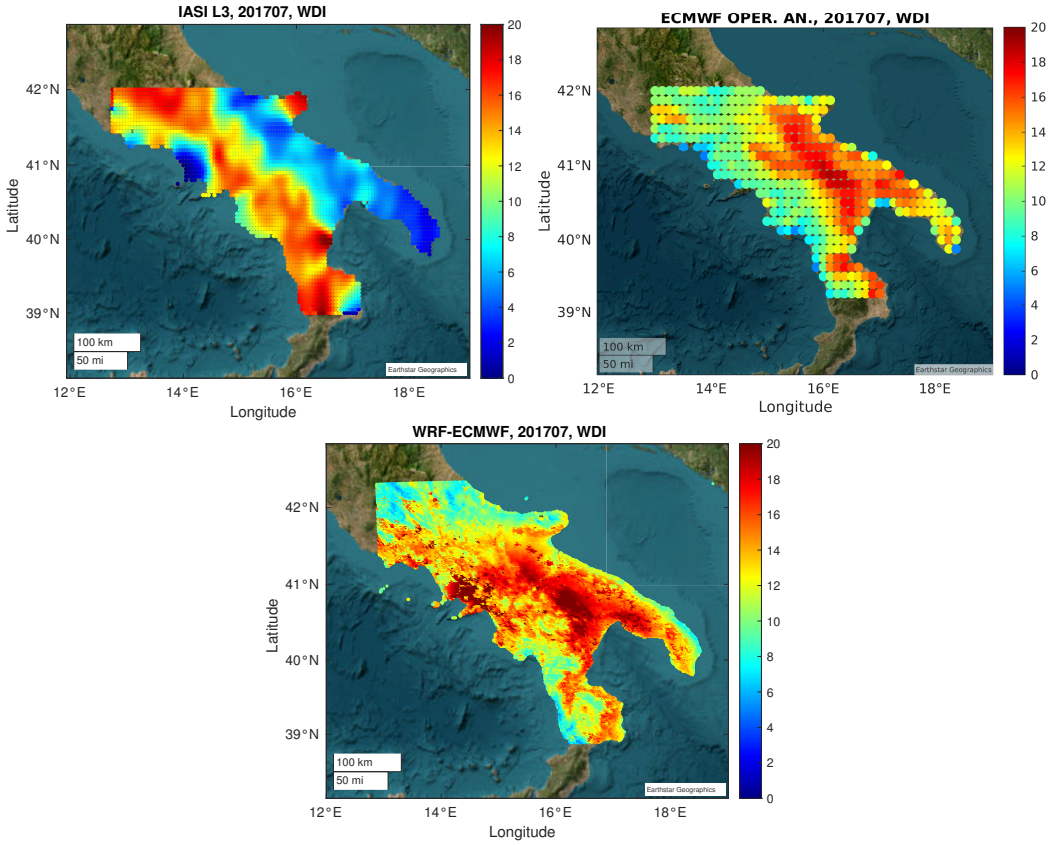

Figure 5.15: Maps of WDI for July 2017. Upper panel: IASI L3 (left, 5 km resolution) and ECMWF operational analysis (right, 12.5 km resolution). Lower panel: WRF-forecasted output (1.2 km resolution) using ECMWF operational analysis data as boundary and initial conditions.

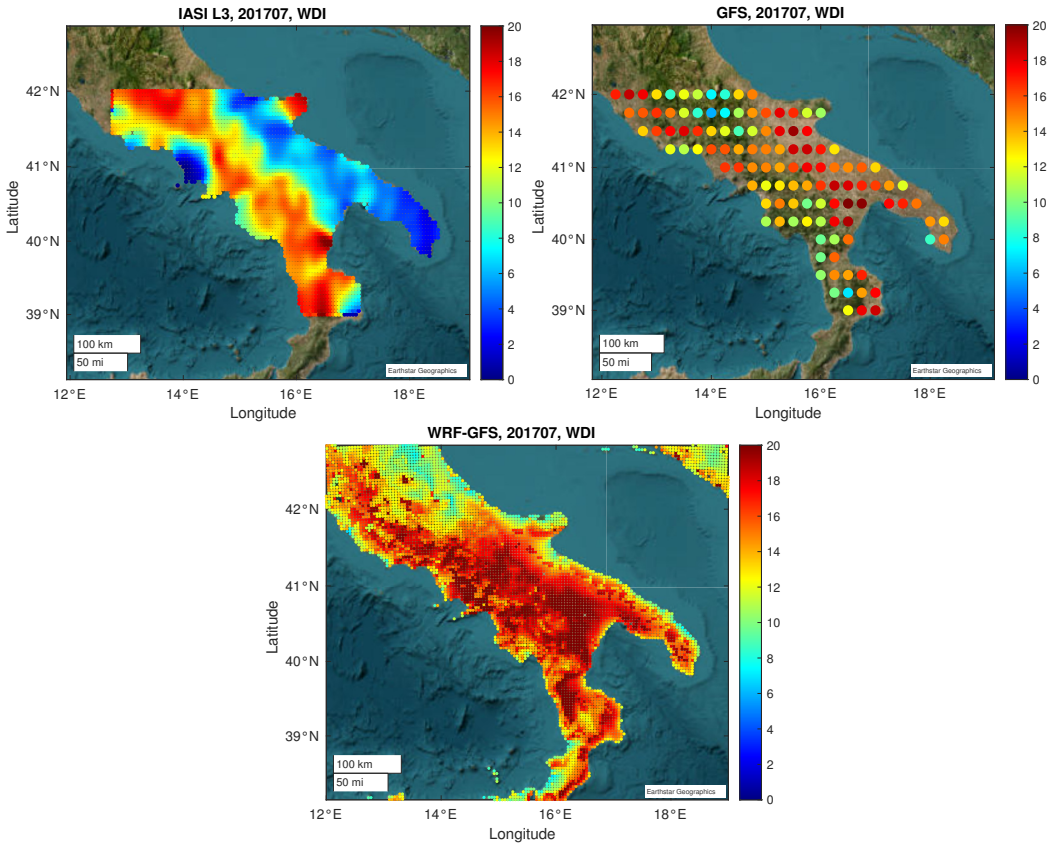

Figure 5.16: Maps of WDI for July 2017. Upper panel: IASI L3 (left, 5 km resolution) and GFS forecasts (right, 25 km resolution). Lower panel: WRF-forecasted output (4 km resolution) using GFS forecast data as boundary and initial conditions.

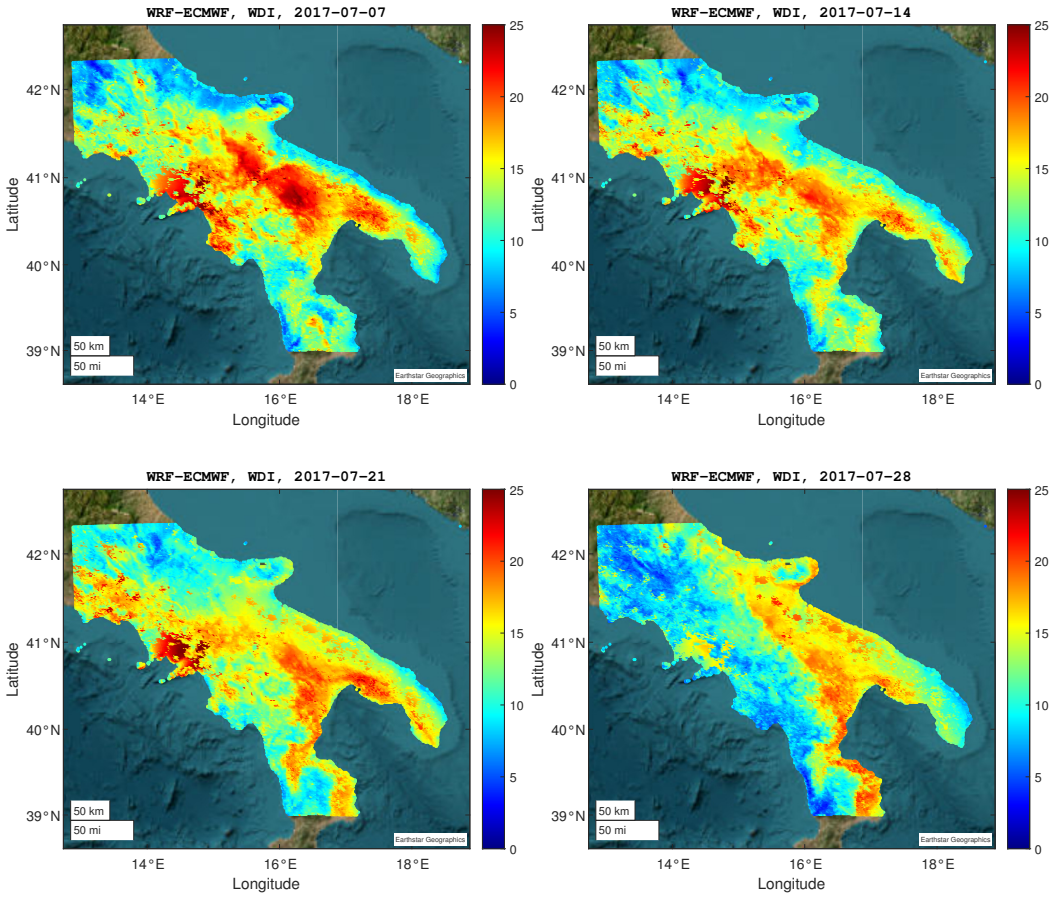

Figure 5.17: WRF-ECMWF WDI maps for July 7th, 14th (upper panel), 21st and 28th (lower panel) 2017.

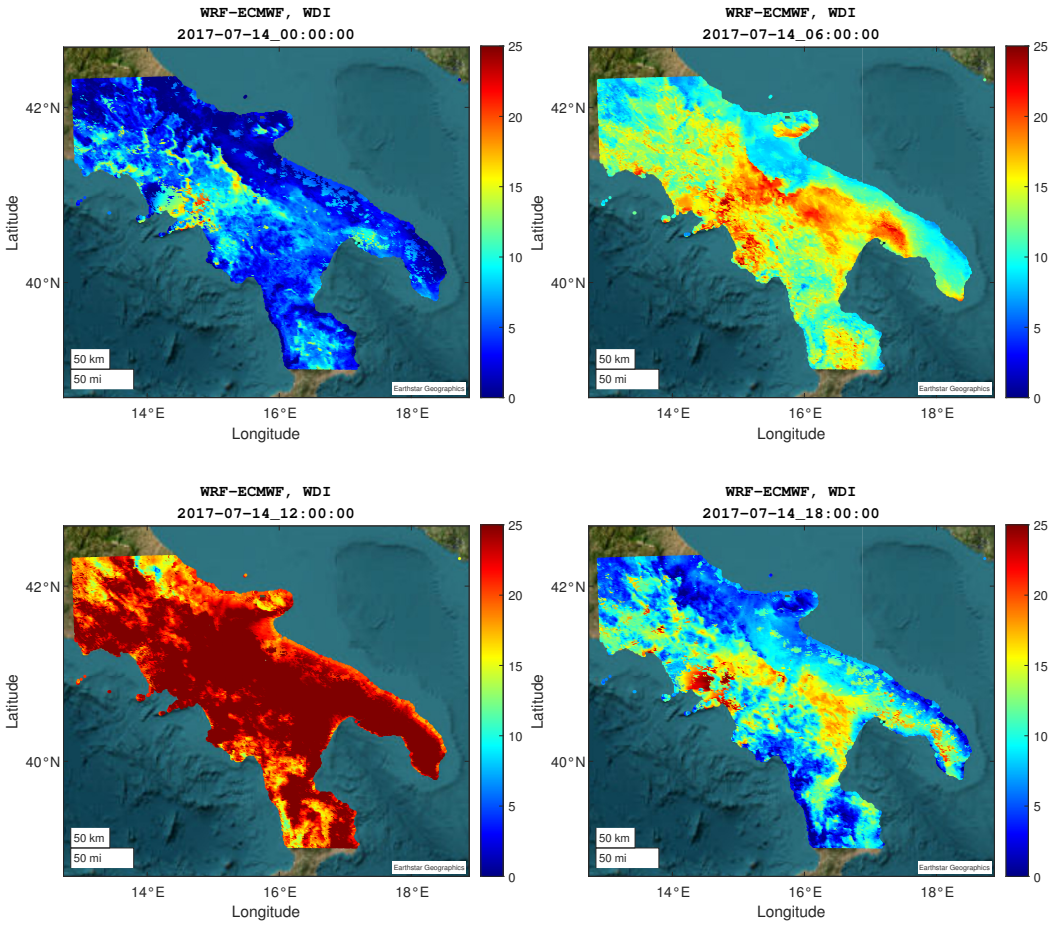

Figure 5.18: WRF-ECMWF WDI maps for July 14th 2017 at the four canonical hours.

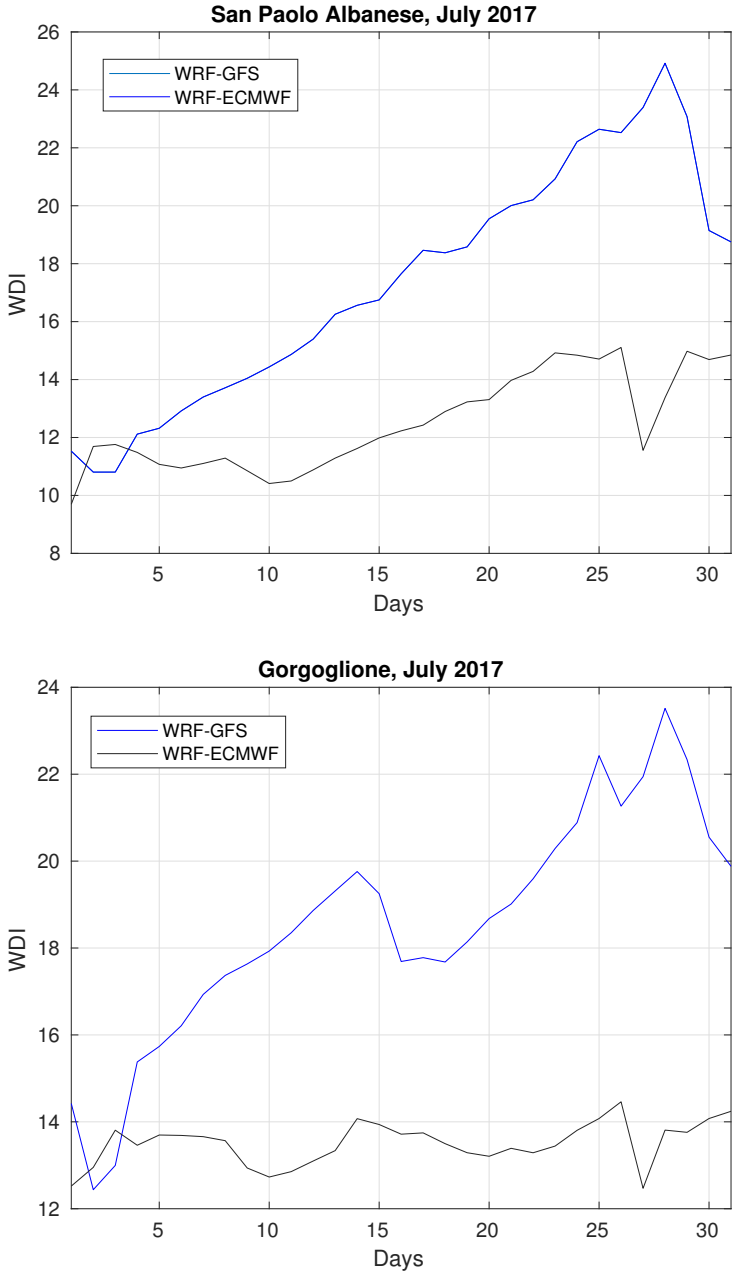

Figure 5.19: WDI values for San Paolo Albanese and Gorgoglione during July 2017, as calculated by both runs.

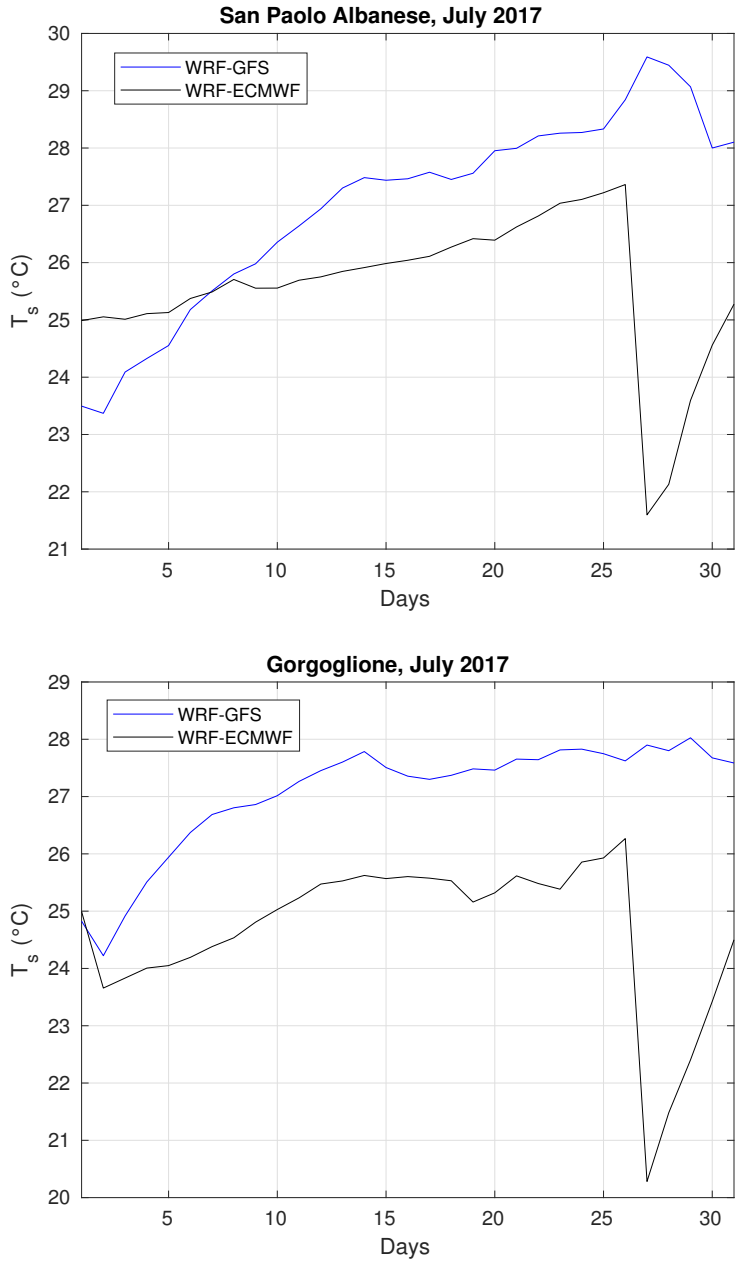

Figure 5.20: Surface temperature values for San Paolo Albanese and Gorgoglione during July 2017, as calculated by both runs.

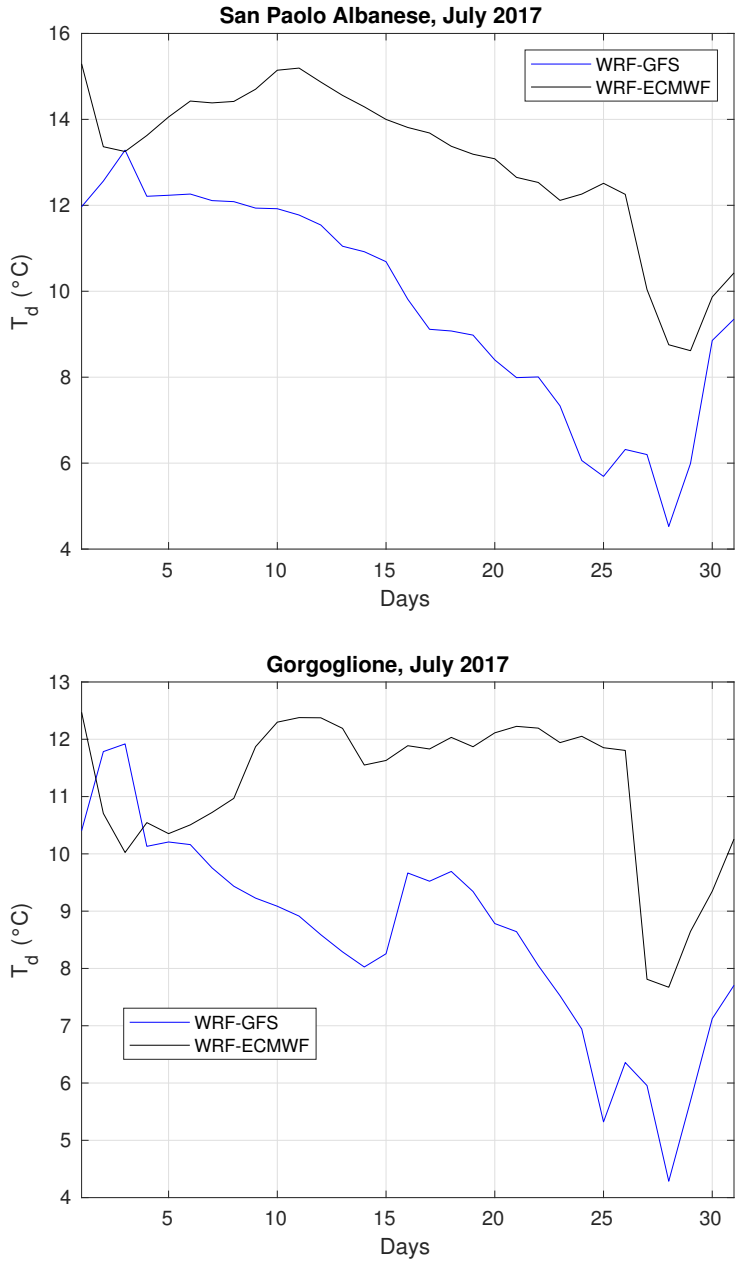

Figure 5.21: Dew-point temperature values for San Paolo Albanese and Gorgoglione during July 2017, as calculated by both runs.

Conclusions

Utilizing the simultaneous retrieval capabilities of the IASI instrument for surface and thermodynamic parameters, WDI and ECI were developed to assess severe drought conditions, especially within forests. A case study conducted in Southern Italy, which experienced intense droughts and heatwaves from the summer months of 2014-2022, aimed at evaluating the effectiveness of ECI and WDI in measuring water deficit severity during heatwave events. This assessment involved studying their correlations with other vegetation and drought monitoring indices (SSM, LAI, FAPAR, FVC and ET).

Significantly, an inverse correlation was found between WDI and SSM, while a direct correlation was observed with LAI, FAPAR, FVC and ET. This pattern highlighted WDI's ability to capture dynamic interactions at the surface-atmosphere interface and directly measure water deficit induced by intense heatwaves. In contrast, ECI showed correlations with SSM, LAI, FAPAR and FVC but exhibited an anticorrelation with ET. This indicated that ECI was more indicative of the depth of extreme conditions affecting vegetation. It also proved to be a better indicator than LAI, FAPAR and FVC of the senescent state of the Apennines woodlands during the 2017 and 2021 heatwaves, signaling reduced chlorophyll synthesis —an unexpected phenomenon given the heightened sunlight exposure during summer. The overall performance of both ECI and WDI proved to be useful and precise in identifying water stress, even when the most commonly used indices showed inaccuracy.

Moreover, it was demonstrated how the synergy between ECI and WDI can be exploited to detect arsons in regions of high fire risk, especially if used together with fire indices such as NBR and ΔNBR. Low values of ECI, when coupled with a descending WDI trend and a high-severity NBR level, proved to be an indicator of anthropic action over land: the fire outbreak was not related to the extreme water stress due to the 2017 heatwave, but was, in fact, an arson.

Finally, the use of the WRF model with two different global forecast input datasets confirmed the validity of WDI in identifying drougth conditions,

proving to be an effective and extremely useful physical parameter in the context of numerical weather prediction. The possibilty to enlarge the temporal and spatial resolution offered by the WRF model gave the opportuinity to analyze WDI's behaviour at a finer scale: observing its evolution during a single month (July 2017), at an hourly scale, over a water-stressed area (both at a domain and pixel level), confirmed its utility not only when cosidering its annual trend, but also the specific values it provides for reduced temporal windows and small (around $1\,\mathrm{km}^2$) areas.

Overall, it was demonstrated that the synergistic use of both indices and their complementary behaviour in relating to both surface and atmospheric condition are the key factors contributing to their value. Being able to simultaneously obtain such quantities from the same instrument, thus having both spatial and temporal coherence, is extremely difficult, either for satellite observations or in-situ measurements. In this context, IASI shines as a key instrument.

Surely there are numerous future developments to consider. First of all, it should be noted once again that ECI's estimation from the spectral bands used in this thesis is a uniqueness of the IASI instrument: there is, in fact, no other satellite sensor at the moment with the ability to retrieve the emissivity spectrum for such a large TIR interval ($4.8 - 13\,\mu\mathrm{m}$) and with such high spectral resolution ($0.25\,\mathrm{cm}^{-1}$). However, a measurement campaing using a drone with such specifics, and of course higher temporal and spatial resolution, could be of great interest in investigating ECI's performance on a more local scale (under $1\,\mathrm{km}^2$). The same could be done with WDI, as measured from a local station. The main challenge would be identifying the right instrument to use and selecting the measurement stations over specific areas. Identyfing different kind of surfaces and land categories (woodlands, crops, arid soil, urban environement), while having the possibility to estimate both ECI and WDI on a local scale, would be incredibly enriching in the context of exploiting the ECI-WDI synergy.

Lastly, the launch of the Surface, Biology and Geology Observing Terrestrial Thermal Emission Radiometer (SBG OTTER, `https://sbg.jpl.nasa.gov`), a sounder designed by the Jet Propulsion Laboratory (JPL) at NASA to have 7 TIR bands with a spatial resolution of 60 m, could provide high-quality data from which to gain new insights. Its interesting contribution could be used to further test these thermdynamical indices' capabilities and validate their effectiveness in the coming years.

Acknowledgements

I would like to express my sincere gratitude to my advisors, Prof. Guido Masiello and Carmine Serio, for their invaluable support and guidance throughout my doctoral studies. Their expertise, encouragement, and commitment have played a pivotal role in shaping the outcome of this research, providing valuable insights and constructive feedback that greatly enriched the quality of my work. Professor Masiello's dedication, never-ending passion and curiosity have been a constant source of inspiration.

I extend my sincere appreciation to my university colleagues: Gilda, Michele and Antonio, whose camaraderie and shared experiences have enriched my academic journey in countless ways. Their presence and support have made this experience truly unique. I wish them all the success and recognition they deserve in life.

Lastly, my heartfelt thanks go to my beloved boyfriend Marco, who accompanied me in these intense PhD years, for his unwavering support, love, understanding, and advice, and to my parents and my sister Veronica, who have supported me throughout my university path with their warmth, caring, and strength. A PhD is a truly intense experience, both in its most exciting and difficult moments. Their support and understanding, along with Marco's, have been immeasurable, and I am profoundly grateful for the role they have played in this academic success and in enriching my life all the way to this key moment.

Ad maiora semper.

References

Trenberth, Kevin E. et al. (2014). "Global warming and changes in drought". In: *Nature Climate Change* 4.1, pp. 17–22.

Cook, Benjamin I, Justin S Mankin, and Kevin J Anchukaitis (2018). "Climate change and drought: From past to future". In: *Current Climate Change Reports* 4, pp. 164–179.

Samaniego, Luis et al. (2018). "Anthropogenic warming exacerbates European soil moisture droughts". In: *Nature Climate Change* 8.5, pp. 421–426.

Adler, C. et al. (2022). "Cross-Chapter Paper 5: Mountains". In: *Climate Change 2022: Impacts, Adaptation and Vulnerability. Contribution of Working Group II to the Sixth Assessment Report of the Intergovernmental Panel on Climate Change*. Cambridge, UK and New York, USA: Cambridge University Press, pp. 2273–2318. ISBN: 9781009325844. DOI: 10.1017/9781009325844.022.2273.

Christensen, Lindsey et al. (2021). "Increasing plant water stress and decreasing summer streamflow in response to a warmer and wetter climate in seasonally snow-covered forests". In: *Ecohydrology* 14.1, e2256.

Williams, A Park et al. (2020). "Large contribution from anthropogenic warming to an emerging North American megadrought". In: *Science* 368.6488, pp. 314–318.

Edenhofer, Ottmar (2015). *Climate change 2014: mitigation of climate change*. Vol. 3. Cambridge University Press.

D'Orangeville, Loic et al. (2018). "Drought timing and local climate determine the sensitivity of eastern temperate forests to drought". In: *Global change biology* 24.6, pp. 2339–2351.

Cholet, Cybele et al. (2022). "Climate change increases the severity and duration of soil water stress in the temperate forest of eastern North America". In: *Frontiers in Forests and Global Change* 5, p. 879382.

Lisar, Seyed YS, Rouhollah Motafakkerazad, and Mosharraf M Hossain (2012). "Water Stress in Plants: Causes, Effects and Responses. Water Stress,

Prof. Ismail Md. Mofizur Rahman (Ed.), ISBN: 978-953-307-963-9". In: *Tech. doi* 10, p. 39363.

Imadi, Sameen Ruqia et al. (2016). "Water stress: types, causes, and impact on plant growth and development". In: *Water stress and crop plants: a sustainable approach* 2, pp. 343–355.

Hsiao, Theodore C (1973). "Plant responses to water stress". In: *Annual review of plant physiology* 24.1, pp. 519–570.

Kramer, Paul J (1963). "Water Stress and Plant Growth 1". In: *Agronomy Journal* 55.1, pp. 31–35.

Rita, Angelo et al. (2020). "The impact of drought spells on forests depends on site conditions: The case of 2017 summer heat wave in southern Europe". In: *Global change biology* 26.2, pp. 851–863.

Anderegg, William RL et al. (2020). "Climate-driven risks to the climate mitigation potential of forests". In: *Science* 368.6497, eaaz7005.

Mishra, Ashok K and Vijay P Singh (2010). "A review of drought concepts". In: *Journal of hydrology* 391.1-2, pp. 202–216.

Feiziasl, V et al. (2022). "Water deficit index to evaluate water stress status and drought tolerance of rainfed barley genotypes in cold semi-arid area of Iran". In: *Agricultural Water Management* 262, p. 107395.

Spinoni, Jonathan et al. (2019). "A new global database of meteorological drought events from 1951 to 2016". In: *Journal of Hydrology: Regional Studies* 22, p. 100593.

Sutanto, Samuel J et al. (2019). "Moving from drought hazard to impact forecasts". In: *Nature Communications* 10.1, p. 4945.

Stoyanova, Julia S and Christo G Georgiev (2013). "SVAT modelling in support to flood risk assessment in Bulgaria". In: *Atmospheric research* 123, pp. 384–399.

Gouveia, C, RM Trigo, and CC DaCamara (2009). "Drought and vegetation stress monitoring in Portugal using satellite data". In: *Natural Hazards and Earth System Sciences* 9.1, pp. 185–195.

Bento, Virgílio A et al. (2018). "Contribution of land surface temperature (TCI) to vegetation health index: A comparative study using clear sky and all-weather climate data records". In: *Remote Sensing* 10.9, p. 1324.

Stoyanova, Julia et al. (2019). "Spatial-temporal variability of land surface dry anomalies in climatic aspect: biogeophysical insight by Meteosat observations and SVAT modeling". In: *Atmosphere* 10.10, p. 636.

Feldman, Andrew F et al. (2020). "Land-atmosphere drivers of landscape-scale plant water content loss". In: *Geophysical Research Letters* 47.22, e2020GL090331.

Vicente-Serrano, Sergio M, X Pons-Fernández, and JM Cuadrat-Prats (2004). "Mapping soil moisture in the central Ebro river valley (northeast Spain)

with Landsat and NOAA satellite imagery: a comparison with meteorological data". In: *International Journal of Remote Sensing* 25.20, pp. 4325–4350.

Harris, A, RG Bryant, and AJ Baird (2006). "Mapping the effects of water stress on Sphagnum: Preliminary observations using airborne remote sensing". In: *Remote Sensing of Environment* 100.3, pp. 363–378.

Joshi, Rakesh Chandra et al. (2021). "Modeling Vegetation Water Stress over the Forest from Space: Temperature Vegetation Water Stress Index (TVWSI)". In: *Remote Sensing* 13.22, p. 4635.

Liu, Na et al. (2020). "Thermal remote sensing of plant water stress in natural ecosystems". In: *Forest Ecology and Management* 476, p. 118433.

Govender, M et al. (2009). "Review of commonly used remote sensing and ground-based technologies to measure plant water stress". In: *Water Sa* 35.5.

Huete, AR (2004). "Remote sensing for environmental monitoring". In: *Environmental monitoring and characterization*. Elsevier, pp. 183–206.

Wang, Junming et al. (2010). "Review of satellite remote sensing use in forest health studies". In: *The Open Geography Journal* 3.1.

Gausman, Harold W (1977). "Reflectance of leaf components". In: *Remote sensing of Environment* 6.1, pp. 1–9.

Ceccato, Pietro et al. (2001). "Detecting vegetation leaf water content using reflectance in the optical domain". In: *Remote sensing of environment* 77.1, pp. 22–33.

Coops, Nicholas C et al. (2003). "Chlorophyll content in eucalypt vegetation at the leaf and canopy scales as derived from high resolution spectral data". In: *Tree Physiology* 23.1, pp. 23–31.

Curran, Paul J, Jennifer L Dungan, and Henry L Gholz (1990). "Exploring the relationship between reflectance red edge and chlorophyll content in slash pine". In: *Tree physiology* 7.1-2-3-4, pp. 33–48.

Stone, Christine, Laurie Chisholm, and N Coops (2001). "Spectral reflectance characteristics of eucalypt foliage damaged by insects". In: *Australian Journal of Botany* 49.6, pp. 687–698.

Blackburn, George Alan (1999). "Relationships between spectral reflectance and pigment concentrations in stacks of deciduous broadleaves". In: *Remote sensing of environment* 70.2, pp. 224–237.

Rouse, John Wilson et al. (1974a). "Monitoring vegetation systems in the Great Plains with ERTS". In: *NASA Spec. Publ* 351.1, p. 309.

Lichtenthaler, Hartmut K (1987). "Chlorophylls and carotenoids: pigments of photosynthetic biomembranes". In: *Methods in enzymology*. Vol. 148. Elsevier, pp. 350–382.

Faurtyot, Thierry and Frédéric Baret (1997). "Vegetation water and dry matter contents estimated from top-of-the-atmosphere reflectance data: A simulation study". In: *Remote Sensing of Environment* 61.1, pp. 34–45.

Asner, Gregory P (1998). "Biophysical and biochemical sources of variability in canopy reflectance". In: *Remote sensing of Environment* 64.3, pp. 234–253.

Coops, Nicholas et al. (2002). "Comparison of green leaf eucalypt spectra using spectral decomposition". In: *Australian Journal of Botany* 50.5, pp. 567–576.

Curran, Paul J, Jennifer L Dungan, Bruce A Macler, et al. (1991). "The effect of a red leaf pigment on the relationship between red edge and chlorophyll concentration". In: *Remote Sensing of Environment* 35.1, pp. 69–76.

Anderson, Liana O et al. (2010). "Remote sensing detection of droughts in Amazonian forest canopies". In: *New Phytologist* 187.3, pp. 733–750.

Eitel, Jan UH et al. (2006). "Suitability of existing and novel spectral indices to remotely detect water stress in Populus spp." In: *Forest Ecology and Management* 229.1-3, pp. 170–182.

Fuchs, M (1990). "Infrared measurement of canopy temperature and detection of plant water stress". In: *Theoretical and Applied Climatology* 42, pp. 253–261.

Sepulcre-Cantó, Guadalupe et al. (2006). "Detection of water stress in an olive orchard with thermal remote sensing imagery". In: *Agricultural and Forest meteorology* 136.1-2, pp. 31–44.

Vicente-Serrano, Sergio M, José M Cuadrat-Prats, and Alfredo Romo (2006). "Aridity influence on vegetation patterns in the middle Ebro Valley (Spain): Evaluation by means of AVHRR images and climate interpolation techniques". In: *Journal of Arid Environments* 66.2, pp. 353–375.

Chen, Shulin et al. (2015). "Temperature vegetation dryness index estimation of soil moisture under different tree species". In: *Sustainability* 7.9, pp. 11401–11417.

Masiello, Guido, Angela Cersosimo, et al. (2020). "Emissivity-based vegetation indices to monitor deforestation and forest degradation in the Congo basin rainforest". In: *Remote Sensing for Agriculture, Ecosystems, and Hydrology XXII*. Vol. 11528. SPIE, pp. 125–138.

Le, Thai Son, Richard Harper, and Bernard Dell (2023). "Application of Remote Sensing in Detecting and Monitoring Water Stress in Forests". In: *Remote Sensing* 15.13. ISSN: 2072-4292. DOI: 10.3390/rs15133360. URL: https://www.mdpi.com/2072-4292/15/13/3360.

Rouse, John Wilson et al. (1974b). "Monitoring vegetation systems in the Great Plains with ERTS". In: *NASA Spec. Publ* 351.1, p. 309.

Musick, H Brad and Ramona E Pelletier (1988). "Response to soil moisture of spectral indexes derived from bidirectional reflectance in thematic mapper wavebands". In: *Remote sensing of environment* 25.2, pp. 167–184.

Hunt Jr, E Raymond and Barrett N Rock (1989). "Detection of changes in leaf water content using near-and middle-infrared reflectances". In: *Remote sensing of environment* 30.1, pp. 43–54.

Gao, Bo-Cai (1996). "NDWI—A normalized difference water index for remote sensing of vegetation liquid water from space". In: *Remote sensing of environment* 58.3, pp. 257–266.

Jackson, Thomas J et al. (2004). "Vegetation water content mapping using Landsat data derived normalized difference water index for corn and soybeans". In: *Remote Sensing of Environment* 92.4, pp. 475–482.

Daly, Edorado and Amilcare Porporato (2005). "A review of soil moisture dynamics: from rainfall infiltration to ecosystem response". In: *Environmental engineering science* 22.1, pp. 9–24.

Amani, Meisam et al. (2017). "Temperature-vegetation-soil moisture dryness index (TVMDI)". In: *Remote sensing of environment* 197, pp. 1–14.

Zhang, Ruidong et al. (2019). "The leaf-air temperature difference reflects the variation in water status and photosynthesis of sorghum under waterlogged conditions". In: *PLoS One* 14.7, e0219209.

Sandholt, Inge, Kjeld Rasmussen, and Jens Andersen (2002). "A simple interpretation of the surface temperature/vegetation index space for assessment of surface moisture status". In: *Remote Sensing of environment* 79.2-3, pp. 213–224.

Rahimzadeh-Bajgiran, Parinaz, Kenji Omasa, and Yo Shimizu (2012). "Comparative evaluation of the Vegetation Dryness Index (VDI), the Temperature Vegetation Dryness Index (TVDI) and the improved TVDI (iTVDI) for water stress detection in semi-arid regions of Iran". In: *ISPRS Journal of Photogrammetry and Remote Sensing* 68, pp. 1–12.

Myneni, Ranga B et al. (1997). "Estimation of global leaf area index and absorbed PAR using radiative transfer models". In: *IEEE Transactions on Geoscience and remote sensing* 35.6, pp. 1380–1393.

Widlowski, Jean-Luc et al. (2004). "Canopy structure parameters derived from multi-angular remote sensing data for terrestrial carbon studies". In: *Climatic Change* 67, pp. 403–415.

Chu, Duo and Duo Chu (2020). "Fractional Vegetation Cover". In: *Remote sensing of land use and land cover in mountain region: a comprehensive study at the central Tibetan Plateau*, pp. 195–207.

Karnieli, Arnon et al. (2010). "Use of NDVI and land surface temperature for drought assessment: Merits and limitations". In: *Journal of climate* 23.3, pp. 618–633.

Galvão, Lênio Soares, Icaro Vitorello, and Marco Antonio Pizarro (2000). "An adequate band positioning to enhance NDVI contrasts among green vegetation, senescent biomass, and tropical soils". In: *International Journal of Remote Sensing* 21.9, pp. 1953–1960.

Berg, Alexis et al. (2014). "Impact of soil moisture–atmosphere interactions on surface temperature distribution". In: *Journal of Climate* 27.21, pp. 7976–7993.

Jiang, Kang et al. (2022). "Influence patterns of soil moisture change on surface-air temperature difference under different climatic background". In: *Science of the Total Environment* 822, p. 153607.

Du, Lingtong et al. (2017). "Comparison of two simulation methods of the temperature vegetation dryness index (TVDI) for drought monitoring in semi-arid regions of China". In: *Remote Sensing* 9.2, p. 177.

Guo, Yuchen et al. (2023). "The Factors Affecting the Quality of the Temperature Vegetation Dryness Index (TVDI) and the Spatial–Temporal Variations in Drought from 2011 to 2020 in Regions Affected by Climate Change". In: *Sustainability* 15.14, p. 11350.

Baret, Frederic and Samuel Buis (2008). "Estimating canopy characteristics from remote sensing observations: Review of methods and associated problems". In: *Advances in land remote sensing: System, modeling, inversion and application*, pp. 173–201.

Ru, Chen et al. (2020). "Evaluation of the crop water stress index as an indicator for the diagnosis of grapevine water deficiency in greenhouses". In: *Horticulturae* 6.4, p. 86.

Hilton, Fiona et al. (2012). "Hyperspectral Earth observation from IASI: Five years of accomplishments". In: *bulletin of the american meteorological Society* 93.3, pp. 347–370.

Liuzzi, G et al. (2016). "Physical inversion of the full IASI spectra: Assessment of atmospheric parameters retrievals, consistency of spectroscopy and forward modelling". In: *Journal of Quantitative Spectroscopy and Radiative Transfer* 182, pp. 128–157.

Masiello, Guido, Carmine Serio, Sara Venafra, Giuliano Liuzzi, et al. (2018). "Physical retrieval of land surface emissivity spectra from hyper-spectral infrared observations and validation with in situ measurements". In: *Remote Sensing* 10.6, p. 976.

De Feis, Italia, Guido Masiello, and Angela Cersosimo (2020). "Optimal interpolation for infrared products from hyperspectral satellite imagers and sounders". In: *Sensors* 20.8, p. 2352.

Masiello, Guido, Carmine Serio, A Carissimo, et al. (2009). "Application of φ-IASI to IASI: retrieval products evaluation and radiative transfer

consistency". In: *Atmospheric Chemistry and Physics* 9.22, pp. 8771–8783.

Masiello, G et al. (2012). "IASI Retrieval of temperature, water vapor and ozone profiles over land with φ-IASI package during the COPS campaign". In: *measurements* 2, p. 3.

Rodgers, Clive D (2000). *Inverse methods for atmospheric sounding: theory and practice*. Vol. 2. World scientific.

Amato, Umberto et al. (2002). "The σ-IASI code for the calculation of infrared atmospheric radiance and its derivatives". In: *Environmental Modelling & Software* 17.7, pp. 651–667.

Carissimo, Annamaria, Italia De Feis, and Carmine Serio (2005). "The physical retrieval methodology for IASI: the δ-IASI code". In: *Environmental Modelling & Software* 20.9, pp. 1111–1126.

Masiello, Guido, Carmine Serio, Thomas Deleporte, et al. (2013). "Comparison of IASI water vapour products over complex terrain with COPS campaign data". In: *Meteorologische Zeitschrift* 22.4, pp. 471–487.

Masiello, Guido, Carmine Serio, Sara Venafra, Italia DeFeis, et al. (2014). "Diurnal variation in Sahara desert sand emissivity during the dry season from IASI observations". In: *Journal of Geophysical Research: Atmospheres* 119.3, pp. 1626–1638.

Shephard, MW et al. (2009). "Performance of the line-by-line radiative transfer model (LBLRTM) for temperature and species retrievals: IASI case studies from JAIVEx". In: *Atmospheric Chemistry and Physics* 9.19, pp. 7397–7417.

Alvarado, MJ et al. (2013). "Performance of the Line-By-Line Radiative Transfer Model (LBLRTM) for temperature, water vapor, and trace gas retrievals: recent updates evaluated with IASI case studies". In: *Atmospheric Chemistry and Physics* 13.14, pp. 6687–6711.

Masiello, Guido and Carmine Serio (2013). "Simultaneous physical retrieval of surface emissivity spectrum and atmospheric parameters from infrared atmospheric sounder interferometer spectral radiances". In: *Applied Optics* 52.11, pp. 2428–2446.

Serio, Carmine, Guido Masiello, Pietro Mastro, et al. (2020). "Simultaneous retrieval of OCS, and CO2 from the IASI shortwave spectral band: assessment of the accuracy of the retrieval products and validation with in situ observations." In: *Remote Sensing of Clouds and the Atmosphere XXV*. Vol. 11531. SPIE, p. 1153107.

Camy-Peyret, C et al. (2017). "Assessment of IASI capability for retrieving carbonyl sulphide (OCS)". In: *Journal of Quantitative Spectroscopy and Radiative Transfer* 201, pp. 197–208.

Amato, U et al. (2014). "Cloud mask via cumulative discriminant analysis applied to satellite infrared observations: scientific basis and initial evaluation". In: *Atmospheric Measurement Techniques* 7.10, pp. 3355–3372.

Serio, C et al. (2019). "CO2 spectroscopy and forward/inverse radiative transfer modelling in the thermal band using IASI spectra". In: *Journal of Quantitative Spectroscopy and Radiative Transfer* 222, pp. 65–83.

Serio, Carmine, Guido Masiello, and Giuliano Liuzzi (2016). "Demonstration of random projections applied to the retrieval problem of geophysical parameters from hyper-spectral infrared observations". In: *Applied Optics* 55.24, pp. 6576–6587.

Masiello, Guido, Carmine Serio, and Paolo Antonelli (2012). "Inversion for atmospheric thermodynamical parameters of IASI data in the principal components space". In: *Quarterly Journal of the Royal Meteorological Society* 138.662, pp. 103–117.

Serio, Carmine, Guido Masiello, and Sara Venafra (2019). "CO2 retrieval algorithm for the Infrared Atmospheric Sounder Interferometer: the potential of retrieving the vertical profile of carbon dioxide from its hot or laser bands in the 800-1200 cm-1 atmospheric window". In: *Remote Sensing of Clouds and the Atmosphere XXIV*. Vol. 11152. SPIE, pp. 113–125.

French, AN, TJ Schmugge, and WP Kustas (2000). "Discrimination of senescent vegetation using thermal emissivity contrast". In: *Remote Sensing of Environment* 74.2, pp. 249–254.

Moparthy, Suman, Dominique Carrer, and Xavier Ceamanos (2019). "Can we detect the brownness or greenness of the Congo rainforest using satellite-derived surface Albedo? A study on the role of aerosol uncertainties". In: *Sustainability* 11.5, p. 1410.

Huang, Jianhua (2018). "A simple accurate formula for calculating saturation vapor pressure of water and ice". In: *Journal of Applied Meteorology and Climatology* 57.6, pp. 1265–1272.

Sonntag, Dietrich (1990). "Important new values of the physical constants of 1986, vapor pressure formulations based on the ITS-90, and psychrometer formulae". In: *Z. Meteorol.* 70, pp. 340–344.

Allen, Richard G et al. (1998). "Crop evapotranspiration-Guidelines for computing crop water requirements-FAO Irrigation and drainage paper 56". In: *Fao, Rome* 300.9, p. D05109.

Serio, Carmine, Guido Masiello, Pamela Pasquariello, et al. (2022). "Exploiting the IASI profiling capability for surface parameters, atmospheric temperature, and water vapour to design emissivity contrast and water deficit indexes to monitor forests' response to droughts and heatwaves". In: *Remote Sensing of Clouds and the Atmosphere XXVII*. Ed. by Adolfo

Comerón et al. Vol. 12265. International Society for Optics and Photonics. SPIE, p. 1226502. DOI: 10.1117/12.2642877. URL: https://doi.org/10.1117/12.2642877.

Ripullone, Francesco et al. (2020). "Variation in the access to deep soil water pools explains tree-to-tree differences in drought-triggered dieback of Mediterranean oaks". In: *Tree Physiology* 40.5, pp. 591–604.

Colangelo, Michele et al. (2018). "Drought and Phytophthora are associated with the decline of oak species in southern Italy". In: *Frontiers in plant science*, p. 1595.

Torresani, Michele et al. (2022). "Correlation analysis of evapotranspiration, emissivity contrast and water deficit indices: A case study in four eddy covariance sites in italy with different environmental habitats". In: *Land* 11.11, p. 1903.

San-Miguel-Ayanz, Jesus et al. (2003). "The European forest fire information system (EFFIS)". In: *Joint International Workshop of EARSeL SIG on Forest Fires and the GOFC/GOLD-Fire Program: Innovative Concepts and Methods in Fire Danger Estimation*.

WMO (2023). *Exceptional heat and rain, wildfires and floods mark summer of extremes*. URL: https://public.wmo.int/en/media/news/exceptional-heat-and-rain-wildfires-and-floods-mark-summer-of-extremes (visited on 10/13/2023).

Velez, R (2009). "The causing factors: a focus on economic and social driving forces". In: *Living with wildfires: what science can tell us. EFI Discussion paper* 15, pp. 21–25.

Lovreglio, Raffaella et al. (2010). "Wildfire cause analysis: four case-studies in southern Italy". In: *iForest-Biogeosciences and Forestry* 3.1, p. 8.

Canepa, Alessandra and Federico Drogo (2021). "Wildfire crime, apprehension and social vulnerability in Italy". In: *Forest Policy and Economics* 122, p. 102330.

De Luca, Paolo (2017). *Incendio sul Vesuvio, fronte del fuoco di due chilometri: evacuate case e ristoranti*. URL: https://napoli.repubblica.it/cronaca/2017/07/11/news/incendio_vesuvio-170531573/ (visited on 10/13/2023).

VesuvioLive (2018). *11 Luglio 2017, a fuoco il Vesuvio: è il più grande disastro ambientale della sua storia*. URL: https://www.vesuviolive.it/ultime-notizie/256710-11-luglio-2017-a-fuoco-il-vesuvio-e-il-piu-grande-disastro-ambientale-della-sua-storia/ (visited on 10/13/2023).

Di Fiore, Gigi (2021). *Incendi sul Vesuvio 2017, quattro anni dopo sono stati arrestati solo due colpevoli*. URL: https://www.ilmattino.it/

napoli/cronaca/incendio_sul_vesuvio_2017-6118677.html (visited on 10/13/2023).

Buttner, Gyorgy (2014). "CORINE land cover and land cover change products". In: *Land use and land cover mapping in Europe: practices & trends*. Springer, pp. 55–74.

Escuin, S, R Navarro, and P Fernández (2008). "Fire severity assessment by using NBR (Normalized Burn Ratio) and NDVI (Normalized Difference Vegetation Index) derived from LANDSAT TM/ETM images". In: *International Journal of Remote Sensing* 29.4, pp. 1053–1073.

Miller, Jay D and Andrea E Thode (2007). "Quantifying burn severity in a heterogeneous landscape with a relative version of the delta Normalized Burn Ratio (dNBR)". In: *Remote sensing of Environment* 109.1, pp. 66–80.

Beck, Jeffrey et al. (2020). "An evaluation of a hybrid, terrain-following vertical coordinate in the WRF-based RAP and HRRR models". In: *Weather and Forecasting* 35.3, pp. 1081–1096.

Skamarock, William C et al. (2019). "A description of the advanced research WRF version 4". In: *NCAR tech. note ncar/tn-556+ str* 145.

Chen, Shu-Hua and Wen-Yih Sun (2002). "A one-dimensional time dependent cloud model". In: *Journal of the Meteorological Society of Japan. Ser. II* 80.1, pp. 99–118.

Mlawer, Eli J et al. (1997). "Radiative transfer for inhomogeneous atmospheres: RRTM, a validated correlated-k model for the longwave". In: *Journal of Geophysical Research: Atmospheres* 102.D14, pp. 16663–16682.

Dudhia, Jimy (1989). "Numerical study of convection observed during the winter monsoon experiment using a mesoscale two-dimensional model". In: *Journal of Atmospheric Sciences* 46.20, pp. 3077–3107.

Janić, Zaviša I (2001). "Nonsingular implementation of the Mellor-Yamada level 2.5 scheme in the NCEP Meso model". In.

Mukul Tewari, NCAR et al. (2004). "Implementation and verification of the unified NOAH land surface model in the WRF model (Formerly Paper Number 17.5)". In: *Proceedings of the 20th conference on weather analysis and forecasting/16th conference on numerical weather prediction, Seattle, WA, USA*. Vol. 14.

Janjić, Zaviša I (1994). "The step-mountain eta coordinate model: Further developments of the convection, viscous sublayer, and turbulence closure schemes". In: *Monthly weather review* 122.5, pp. 927–945.

Kain, John S (2004). "The Kain–Fritsch convective parameterization: an update". In: *Journal of applied meteorology* 43.1, pp. 170–181.